ABSTRACT

OPTICAL ENGINEERING OF III-NITRIDE NANOWIRE LIGHT-EMITTING DIODES AND APPLICATIONS

By
Ha Quoc Thang Bui

Applications of III-nitride nanowires are intensively explored in different emerging technologies including light-emitting diodes (LEDs), laser diodes, photodiodes, biosensors, and solar cells. The synthesis of the III-nitride nanowires by molecular beam epitaxy (MBE) is investigated with significant achievements. III-nitride nanowires can be grown on dissimilar substrates i.e., silicon with nearly dislocation free due to the effective strain relaxation. III-nitride nanowires, therefore, are perfectly suited for high performance light emitters for cost-effective fabrication of the advanced photonic-electronic integrated platforms. This dissertation addresses the design, fabrication, and characterization of III-nitride nanowire full-color micro-LED **(**μLED) on silicon substrates for μLED display technologies, high-efficient ultraviolet (UV) LEDs, and spectral engineering for narrow band LEDs.

In this dissertation, InGaN/AlGaN nanowire μLEDs were demonstrated with highly stable emission which can be varied from the blue to red spectrum. Additionally, by integrating full-color emissions in a single nanowire, phosphor-free white-color μLEDs are achieved with an unprecedentedly high color rendering index of ~ 94. Such high-performance μLEDs are perfectly suitable for the next generation high-resolution micro-display applications. Moreover, the first demonstration of two-step surface passivation using Potassium Hydroxide (KOH) and Ammonium Sulfide $(NH_4)_2S_x$ is reported. The photoluminescence, electroluminescence, and optical power of the 335 nm AlGaN

nanowire UV LEDs show improvements by 49%, 83%, and 65%, respectively. Such enhanced performance is attributed to the mitigation of the surface nonradiative recombination on the nanowire surfaces. A combination of KOH and $(NH_4)_2S_x$ treatment shows a promising approach for high efficiency and high power AlGaN nanowire UV LEDs.

The LEDs with narrow spectra are highly desirable light sources for precisely controlled applications such as phototherapy. In this regard, we have further demonstrated narrow spectral nanowire LEDs using on-chip integrated bandpass filters. To achieve narrow band spectra, the bandpass filters are designed and fabricated using all-dielectric and metal-dielectric multilayers for visible and UV regions, respectively. They are fabricated onto LED devices as a single photonic platform to achieve the narrow band LEDs for innovative applications like phototherapy for wound healing.

OPTICAL ENGINEERING OF III-NITRIDE NANOWIRE LIGHT-EMITTING DIODES AND APPLICATIONS

by
Ha Quoc Thang Bui

A Dissertation
Submitted to the Faculty of
New Jersey Institute of Technology
in Partial Fulfillment of the Requirements for the Degree of
Doctor of Philosophy in Electrical Engineering

Helen and John C. Hartmann Department of
Electrical and Computer Engineering

May 2021

APPROVAL PAGE

OPTICAL ENGINEERING OF III-NITRIDE NANOWIRE LIGHT-EMITTING DIODES AND APPLICATIONS

Ha Quoc Thang Bui

Dr. Hieu Pham Trung Nguyen, Dissertation Advisor — Date
Associate Professor of Electrical and Computer Engineering, NJIT

Dr. Durgamadhab Misra, Committee Member — Date
Professor of Electrical and Computer Engineering, NJIT

Dr. Marek Sosnowski, Committee Member — Date
Professor of Electrical and Computer Engineering, NJIT

Dr. Tao Zhou, Committee Member — Date
Associate Professor of Physics, NJIT

Dr. Roman S. Voronov, Committee Member — Date
Associate Professor of Chemical & Materials Engineering and Biomedical Engineering, NJIT

BIOGRAPHICAL SKETCH

Author: Ha Quoc Thang Bui

Degree: Doctor of Philosophy

Date: May 2021

Undergraduate and Graduate Education:

- Doctor of Philosophy in Electrical Engineering,
  New Jersey Institute of Technology, Newark, NJ, 2021

- Master of Science in Nanomaterials and Nanodevices,
  VNU-University of Engineering and Technology, Hanoi, Vietnam, 2013

- Bachelor of Science in Physics,
  VNUHCM-University of Science, Ho Chi Minh City, Vietnam, 2005

Major: Electrical Engineering

Presentations and Publications:

H. Q. T. Bui, T. T. Doan, R. T. Velpula, B. Jain, H. P. T. Nguyen, and H. D. Nguyen, "Enhancing Efficiency of AlGaN Ultraviolet Light-Emitting Diodes with A Graded *p*-AlGaN Hole Injection Layer," minor revision.

H. Q. T. Bui, R. T. Velpula, B. Jain, and H. P. T. Nguyen, "III-Nitride Based Narrow Band Far-UVC LEDs for Airborne and Surface Disinfection," *ECS Transactions*, vol 98, no. 6, pp. 83-89, 2020.

H. Q. T. Bui, R. T. Velpula, B. Jain, and H. P. T. Nguyen, "High-Performance AlGaN-based Ultraviolet Nanowire Light-Emitting Diodes by Potassium Hydroxide and Ammonium Sulfide Surface Passivation," *Applied Optics*, vol. 59, no. 24, pp. 7352-7356, 2020. **(Editor's Pick).**

H. Q. T. Bui, R. T. Velpula, B. Jain, and H. P. T. Nguyen, "Full-color InGaN/AlGaN Nanowire Micro Light-Emitting Diodes Grown by Molecular Beam Epitaxy: A Promising Candidate for Next Generation Micro Displays," *Micromachines*, vol. 10, no. 8, pp. 492-499, 2019.

M. R. Philip, **H. Q. T. Bui**, and H. P. T. Nguyen, "Molecular Beam Epitaxial Growth and Device Characterization of AlGaN Nanowire Ultraviolet-B Light-Emitting Diodes," *Advanced Optics and Photonics*, vol. 1, no. 1, pp. 3-11, 2018.

R. T. Velpula, B. Jain, **H. Q. T. Bui**, and H. P. T. Nguyen, "Numerical Investigation on The Device Performance of Electron Blocking Layer Free AlInN Nanowire Deep Ultraviolet Light-Emitting Diodes," *Optical Materials Express*, vol. 10, no. 2, pp. 472-483, 2020.

R.T. Velpula, B. Jain, **H. Q. T. Bui,** T. T. Pham, V.T. Le, H. D. Nguyen, T. R. Lenka, and H. P. T. Nguyen, "Design and Characteristic Study of Electron Blocking Layer Free AlInN Nanowire Deep Ultraviolet Light-Emitting Diodes," *arXiv preprint arXiv*:1907.07715, 2019.

B. Jain, R. T. Velpula, **H. Q. T. Bui**, and H. P. T. Nguyen, "High Performance Electron Blocking Layer Free InGaN/GaN Nanowire White-Light-Emitting Diodes," *Optics Express*, vol. 28, no. 1, pp. 665-675, 2020.

R. T. Velpula, B. Jain, **H. Q. T. Bui**, and H. P. T. Nguyen, "Full-Color III-Nitride Nanowire Light-Emitting Diodes," *Advanced Engineering and Computation,* vol. 3, no. 4, pp. 551-588, 2019. (**Invited Review**).

R. T. Velpula, B. Jain, **H. Q. T. Bui**, F. M. Shakiba, J. Jude, M. Tumuna, H-D. Nguyen, and H. P. T. Nguyen, "Improving Carrier Transport in AlGaN Deep-Ultraviolet Light-Emitting Diodes Using A Strip-In-A-Barrier Structure," *Applied Optics*, vol. 59, no. 17, pp. 5276-5281, 2020.

M. Djavid, D. D. Choudharya, M. R. Philip, **H. Q. T. Bui**, and H. P. T. Nguyen, "Effects of Optical Absorption in Deep Ultraviolet Nanowire Light-Emitting Diodes," *Photonics and Nanostructures -Fundamentals and Applications*, vol. 28, pp. 106-110, 2018.

B. Jain, R. T. Velpula, M. Tumuna, **H. Q. T. Bui**, J. Jude, T. T. Pham, and H. P. T. Nguyen, "Enhancing the Light Extraction Efficiency of AlInN Nanowire Ultraviolet Light-Emitting Diodes with Photonic Crystal Structures," *Optics Express*, vol. *28,* no. 15, pp. 22908-22918, 2020.

M. R. Philip, D.D. Choudharya, M. Djavid, M. N. Bhuyian, **H. Q. T. Bui**, and H. P. T. Nguyen, "Fabrication of Phosphor-Free III-Nitride Nanowire Light-Emitting Diodes on Metal Substrates for Flexible Photonics," *ACS Omega*, vol. 2, no. 9, pp. 5708-5714, 2017.

M. R. Philip, H. P. T. Nguyen, R. Babu, V. Krishnakumar, and **T. H. Q. Bui,** "Polyol Synthesis of Zinc Oxide-Graphene Composites: Enhanced Dye-Sensitized Solar Cell Efficiency," *Current Nanomaterials*, vol. 3, no. 1, pp. 52-60, 2018.

D. K. Panda, T. R. Lenka, R. T. Velpula, B. Jain, **H. Q. T. Bui**, T. T. Pham, S. Sadaf, and H. P. T. Nguyen, "Single and Double Gate based GaN MOS-HEMTs for Design of Low Noise Amplifier: A Comparative Study," *IET Circuits, Devices & Systems*, vol. 14, no. 7, pp. 1018-1025, 2020.

R. Singh, D. Panda, T. Lenka, R. T. Velpula, B. Jain, **H. Q. T. Bui**, and H. P. T. Nguyen, "The Dawn of Ga_2O_3 HEMTs for High Power Electronics - A Review," *Materials Science in Semiconductor Processing*, vol. 119, p. 105216, 2020.

R. Singh, D. Panda, T. Lenka, R. T. Velpula, B. Jain, **H. Q. T. Bui**, and H. P. T. Nguyen, "A Novel β-Ga_2O_3 HEMT with f_T of 166 GHz and X-Band P_{OUT} of 2.91 W/mm," *International Journal of Numerical Modelling: Electronic Networks, Devices and Fields*, e2794, 2020.

R. Singh, T. R. Lenka, D. Panda, R. T. Velpula, B. Jain, **H. Q. T. Bui**, H. P. T. Nguyen, "RF Performance of Ultra-wide Bandgap HEMTs," in *Emerging Trends in Terahertz Solid-State Physics and Devices*, Biswas A., Banerjee A., Acharyya A., Inokawa H., Roy J. (Eds), Singapore, Springer, 2020, pp. 49-63.

R. Singh, T. R. Lenka, R. T. Velpula, B. Jain, **H. Q. T. Bui**, H. P. T. Nguyen, "Investigation of Current Collapse and Recovery Time Due to Deep Level Defect Traps in β-Ga_2O_3 HEMT," *Journal of Semiconductors*, vol. 41, no. 10, pp. 102802(1-4), 2020.

H. Q. T. Bui, R. T. Velpula, B. Jain, and H. P. T. Nguyen, "Full-Color MicroLEDs for Display Technologies," in CLEO: Applications and Technology. Optical Society of America, May 10-15, 2020; San Jose, CA. (virtual).

T. H. Q. Bui, M. R. Philip, M. Djavid, H. P. T. Nguyen, "Full-Color Phosphor-Free InGaN/AlGaN Nanowire Light-Emitting Diodes Grown by Molecular Beam Epitaxy," in 2017 Annual Meeting of the APS Mid-Atlantic Section, Bulletin of the American Physical Society 62, November 3-5, 2017; Newark, New Jersey.

M. R. Philip, **T. H. Q. Bui**, M. Djavid, M. N. Bhuyian, P. Vu, and H. P. T. Nguyen, "Phosphor-Free III-Nitride Nanowire White-Light-Emitting Diodes for Visible Light Communication," *in Proceeding of SPIE Conference, Smart Structures and Materials + nondestructive Evaluation and Health Monitoring*, vol. 10595, Denver, CO, USA, March 3-7, 2018, pp. 1059531-7.

M. R. Philip, **T. H. Q. Bui**, M. Djavid, H. P. T. Nguyen, "Phosphor-Free InGaN/AlGaN White-Light-Emitting Diodes on Flexible Substrates," in 2017 Annual Meeting of the APS Mid-Atlantic Section, Bulletin of the American Physical Society 62, November 3-5, 2017; Newark, New Jersey.

R.T. Velpula, B. Jain, **H. Q. T. Bui**, and H. P. T, Nguyen, "High-Efficiency Ultraviolet Emission from AlInN/GaN Nanowires Grown by Molecular Beam Epitaxy," in CLEO: Applications and Technology. Optical Society of America, May 10-15, 2020; San Jose, CA. (virtual).

B. Jain, R. T. Velpula, **H. Q. T. Bui**, M. Tumuna, J. Jude, and H. P. T, Nguyen, “Electron Blocking Layer Free AlGaN Deep-Ultraviolet Light Emitting Diodes” in CLEO: Applications and Technology. Optical Society of America, May 10-15, 2020; San Jose, CA. (virtual).

R. T. Velpula, B. Jain, **H. Q. T. Bui**, and H.P.T, Nguyen, "Ultraviolet Light-Emitting Diodes Using Aluminium Indium Nitride Nanowire Structures," *ECS Meeting Abstracts*. No. 42. *IOP Publishing*, 2020.

B. Jain, R.T. Velpula, **H. Q. T. Bui**, M. Patel, and H. P. T, Nguyen, "Electron Blocking Layer Free Full-Color InGaN/GaN White Light-Emitting Diodes," *ECS Meeting Abstracts*. No. 42. *IOP Publishing*, 2020.

R. Singh, T. R Lenka, D. Panda, R.T. Velpula, B. Jain, **H. Q. T. Bui**, H. P. T. Nguyen, "Ga_2O_3 Based Heterostructure FETs (HFETs) for Microwave Millimeter-Wave Applications," in *Emerging Trends in Terahertz Engineering and System Technologies: Devices, Materials, Imaging, Data Acquisition and Processing*, Biswas A., Banerjee A., Acharyya A., A. Banerjee, H. Inokawa, (Eds), Singapore, Springer, 2021, pp. 209-227.

This dissertation is dedicated to my parents, my siblings, my relatives, my sponsors, my close friends, and my teachers.

"Trời còn để có hôm nay,
Tan sương đầu ngõ, vén mây giữa trời.
Thanks heaven we are here today,
To see the sun through parting fog and clouds."
(The Tale of Kieu, Nguyen Du)

ACKNOWLEDGMENT

The pursuit of a Ph.D. degree is a unique journey in my life with considerable ups-and-downs, but this journey helped me to extend the threshold of my capability of hard-working, consistency, and determination. No word can describe unprecedented years of the COVID pandemic. But, finally, I made it successfully, and of course with the help and sponsorship from many people and institutes. I am so thankful to them and feel grateful when I am here today.

First, I would like to express my gratitude to my dissertation advisor, Dr. Hieu Pham Trung Nguyen. It was my pleasure working, learning, and doing research in his lab. As a very supportive mentor, Dr. Hieu frequently encourages and teaches his students many perspectives in ways of very enthusiasm and commitment. Thanks to him, I developed the critical skill set for research and my career path. Through the development of concise manuscripts for the publication of our research, I have learnt from him basic knowledge, care in detail, and put things into a big picture. Without the significant guidance from Dr. Hieu, I could not successfully defend my doctorate program.

Second, I would like to thank the professors in the committee for their time and efforts in reading, evaluating, and having suggestions during the completion of my Ph.D. dissertation: Dr. Marek Sosnowski, Dr. Tao Zhou, and Dr. Roman S. Voronov. I am especially grateful to Dr. Durgamadhab Misra. As an academic advisor and committee member, he has offered significant support during my Ph.D. program.

Third, I am deeply grateful to two following institutes for their sponsorship: Vietnam International Education Development (VIED), Ministry of Education and Training (MOET) in Vietnam, and Pham Ngoc Thach University of Medicine (PNTU) in

Vietnam. With their financial aid, my pursuit of studying in the USA came true and I am very thankful about that. Moreover, for my colleagues who work in PNTU, I would like to thank specifically Tran Tho Nguyen, Dinh Thuong Le, Thi Kim Anh Nguyen, Thi Nam Tran Phan, and Ngoc Thu Pham, Xuan Thu Luu, Thi Thu Trang Truong, Van Thuy Nguyen, Thi Bich Van Nguyen, and Thi Hiep Le for their help in numerous different ways before and during my Ph.D. program. A special thanks is offered to Dr. Do Kien Cuong and Le Do Ninh who were the chair of the Biomedical Physics Department at PNTU in Vietnam where I worked as a faculty for many years. I would like to thank Dr. Minh Xuan Ngo, and Ngoc Dung Pham, as former presidents of PNTU for their administrative responsibility. In addition, I would like to thank Dr. Tien Dung Nguyen from the International Cooperation Department and Ms. Thi Thanh Tam Nguyen from VIED for coordinating and processing my scholarship.

Fourth, a special thanks to Dr. Hien Duy Tong from Vietnamese German University in Vietnam, who advised and guided me in research during my master's program so that I had a solid preparation for the education journey of my Ph.D. program. I would like to thank my close friends: Dr. Luc Quang Ho, Sa Hoang Huynh, and Van Khoe Nguyen from the National Chiao Tung University in Taiwan; Dr. Quang Khai Le from Leia Inc. in the USA, and Binh Tinh Tran from Suny Polytechnic Institute, NY, USA; Minh Khang Pham from University of Medicine and Pharmacy at Ho Chi Minh City in Vietnam; and My uncle, Hoang Hiep Nguyen, for their sharing and support in down and in need situations. Among them, more than anyone else, a special thanks is attributed to Dr. Quang Ho Luc and Dr. Hien Duy Tong who encouraged and believed in me in that I could do what I dreamt. I would like to thank Vietnamese students at NJIT including Long Quang Pham, Phuoc Vu, Anh Tong, Dung Pham, Danh Pham, Phung Lai, Duyen Nguyen; Chen Wu; and

Matthew Cooper who make my life more colorful during my PhD program. I would like to thank my lab-mates: Ravi Teja Velpula, Barsha Jain, and Moab Rajan Philip. We share research and ideals and work together well. I am grateful for the support and kindness I received by NJIT people: staff administrators in the ECE department, especially Ms. Joan Mahon and Teri Bass; to Dr. Catherine Siemann from the Writing Center, Dr. Jerry Trombella from Office of the Registrar; Susan Bunn, Judith Rigg and Myrna Lopez from Bursar's Office, and those from the Office of Graduate Student, especially Ms. Clarisa Gonzalez-Lenahan and Dr. Sotirios Ziavras who gave help to review my dissertation.

TABLE OF CONTENTS

TABLE OF CONTENTS
(Continued)

TABLE OF CONTENTS
(Continued)

LIST OF TABLES

LIST OF FIGURES

LIST OF FIGURES
(Continued)

LIST OF FIGURES
(Continued)

LIST OF FIGURES
(Continued)

LIST OF SYMBOLS

Am-MBE	Ammonia Molecular Beam Epitaxy
ATP	Adenosine Triphosphate
CRI	Color Rendering Index
CVD	Chemical Vapor Deposition
EBL	Electron Blocking Layer
EL	Electroluminescence
EQE	External Quantum Efficiency
FDTD	Finite-Difference Time-Domain
FWHM	Full Width at Half Maximum
IQE	Internal Quantum Efficiency
LEDs	Light-Emitting Diodes
LEE	Light Extraction Efficiency
LPCVD	Low Pressure Chemical Vapor Deposition
MBE	Molecular Beam Epitaxy
MC	Mast Cells
MOCVD	Metal Organic Chemical Vapor Deposition
MQWs	Multi Quantum Wells
MRSA	Methicillin-Resistant Staphylococcus Aureus
PAMBE	Plasma Assisted Molecular Beam Epitaxy
PCR	Polymerase chain reaction
PECVD	Plasma Enhanced Chemical Vapor Deposition
PL	Photoluminescence
PVD	Physical Vapor Deposition
QCSE	Quantum Confined Stark Effect
ROS	Reactive Oxygen Species

RGB	Red, Green, and Blue
RHEED	Reflection High-Energy Electron Diffraction
RIE	Reactive Ion Etching
SAG	Selective Area Growth
UV	Ultraviolet
VEGF	Vascular Endothelial Growth Factors
VLC	Visible Light Communication
VLS	Vapor-Liquid-Solid
μLEDs	Micro Light-Emitting Diodes

STATEMENT OF ORIGINALITY

The accomplishments in this dissertation take on peculiar significance in the field of photonics, materials science, nanotechnology through addressing last-long issues regarding III-nitride full-color LEDs and UV LEDs by using 1D nanowire structures. The nanowire LEDs were grown by MBE. The unique contribution of this Ph.D. dissertation includes the demonstration of full-color μLEDs in circular shape with diameter less than 50 μm; the first demonstration of two-step surface passivation for the enhanced light output power of nanowire UV LEDs; and the first reported nanowire LEDs using integrated bandpass filters. These LEDs are highly promising for the future monolithic microLED displays, AR/VR devices, water/air/surface disinfection, phototherapy, and wound healing. These unique contributions are described below:

We have developed, for the first time, full-color nanowire μLEDs with stable emissions in the red, green, and blue wavelength regions. The nanowire μLEDs are in circular shape with the diameter less than 50 μm. Moreover, we have reported the first demonstration of phosphor-free nanowire white-color μLEDs with unprecedentedly high CRI of ~ 94. These high efficiency, high color rendering properties, and low power consumption μLEDs are perfectly suitable as an alternative replacement of current display technologies.

We also reported the first experimental demonstration of two-step surface passivation using Potassium Hydroxide (KOH) and Ammonium Sulfide $(NH_4)_2S_x$. The photoluminescence, electroluminescence, and optical power of the 335 nm AlGaN nanowire UV LEDs show improvements by 49%, 83%, and 65%, respectively. Such enhanced performance is attributed to the mitigation of the surface nonradiative

recombination on the nanowire surfaces. A combination of KOH and $(NH_4)_2S_x$ treatment shows a promising approach for high efficiency and high power AlGaN nanowire UV LEDs. This study was published and selected as the Editor's pick in Applied Optics (The Optical Society of America).

We demonstrated the first narrow band nanowire LEDs using integrated bandpass filters. The 550 nm visible bandpass filter using 21 alternative all-dielectric Si_3N_4/SiO_2 layers and 310 nm UVB bandpass filters using 6 alternative metal-dielectric Ag/SiO_2 layers have been designed and fabricated. The results show that the integration of visible filters could produce emission with a full width at half maximum (FWHM) around 10 nm which is about five to eight times smaller than the recorded number from typical LEDs. The UV bandpass filter has high transmission up to 70% which is higher than other reported value for UV bandpass filters.

In conclusion, the studies reported in this Ph.D. dissertation have significantly contributed to the understanding and developing of high-performance light emitters using III-nitride semiconductors.

CHAPTER 1

INTRODUCTION

1.1 III-Nitride Nanowire LEDs

1.1.1 Overview

Light-emitting diodes (LEDs) can be found almost everywhere in the daily lighting, automotive lighting, street lighting, backlight of TV and smartphone screens. Besides these main markets, visible and ultraviolet (UV) LEDs have enormous potential applications for bio-imaging, light-visible communication, lidar, precise phototherapy, medical instruments, displays, water treatment, agriculture, and polymer curing [1-8]. New interesting applications such as post-harvest preservation and photobiomodulation from LEDs are also being explored day by day [9, 10].

An LED basically consists of a *p*-*n* junction emitting light when a forward voltage is applied between the two ends of the junction. Electrons and holes are the majority carriers in the *n*-type and in the *p*-type semiconductors, respectively. The *n*-type and *p*-type semiconductors are created by the doping process, adding impurities. Assuming that all dopants are ionized so that the electron concentration (n) is given by number of donors (N_D), and hole concentration (p) is given by the acceptor concentration (N_A).

When *n*- and *p*-type semiconductors are contacted, the electrons from the *n*-type diffuse over to the *p*-type, and conversely the holes from the *p*-type diffuse over to the *n*-type semiconductor. Consequently, two regions of the opposite charges are built-up, positive charges on the *n*-type and negative charges on the *p*-type of the *p*-*n* junction. This

phenomenon is caused by the diffusion current of electrons and holes. At the end, the accumulated charges result in an electric potential difference at the *p*-*n* junction. Meanwhile, the associated built-in electric field, generated by a potential difference between two oppositely charged regions, prevents the diffusion current of electrons and holes from further happening. At this point, the *p*-*n* junction reaches the equilibrium state. The junction area becomes a depletion region, relatively free of charge carriers, no mobile electrons and holes. The built-in potential forementioned in the *p*-*n* junction is called the diffusion voltage (V_D), given by equation (1.1). A typical *p*-*n* junction is illustrated in Figure 1.1. The depletion region is also called the active region because the emissive photons are generated when the *p*-*n* junction under a forward bias.

$$V_D = \frac{kT}{e} \ln \frac{N_A N_D}{n_i^2} \tag{1.1}$$

Here, n_i is the intrinsic carrier concentration of the semiconductor, N_A and N_D is the acceptor and donor concentration, respectively. T is the absolute temperature and k is Boltzmann constant.

When an external voltage, equal or larger than the diffusion voltage, is applied to the *p*-*n* junction, electrons and holes are moved across the depletion region and able to recombine. The recombination process, which radiates photons, is known as *radiative* recombination. Another competitive process does not radiate photons, known as the *nonradiative* recombination. In the *nonradiative* recombination, the energy releases as vibrations in the crystal lattice.

The energy of emissive photons from an LED and the radiation wavelength are given by Equation (1.2), The design and fabrication of LEDs are to achieve as high *radiative* recombination as possible and reduce *nonradiative* recombination.

$$E_g \approx \frac{hc}{\lambda} \tag{1.2}$$

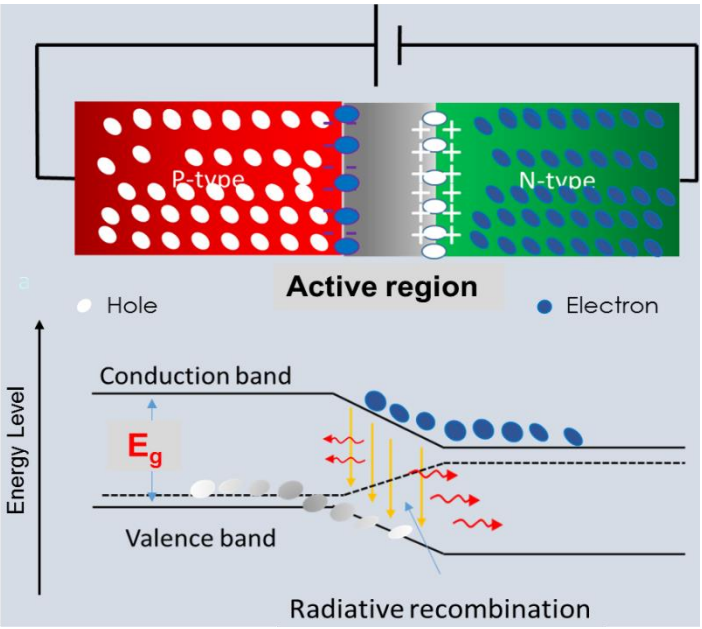

Figure 1.1 The schematic and band energy diagram of a *p-n* junction.

When it comes to the design of an LED, there are two important factors needed to be considered including internal quantum efficiency (IQE) and light extraction efficiency (LEE) because they finally define the external quantum efficiency (EQE) of an LED. An ideal LED can convert the total electric energy to the optical energy as emissive photons. Each photon radiating from the active region of a *p-n* junction is associated with a single injected electron. In other words, the IQE of the ideal LED is equal unity. However, there

is not the case for real LEDs which always have an IQE lower than 100% due to the nonradiative recombination.

To obtain a high value of IQE, real LED devices usually employ multi-quantum wells (MQW) in the active region to increase the carrier quantum confinement for high optical efficiency [11-13].

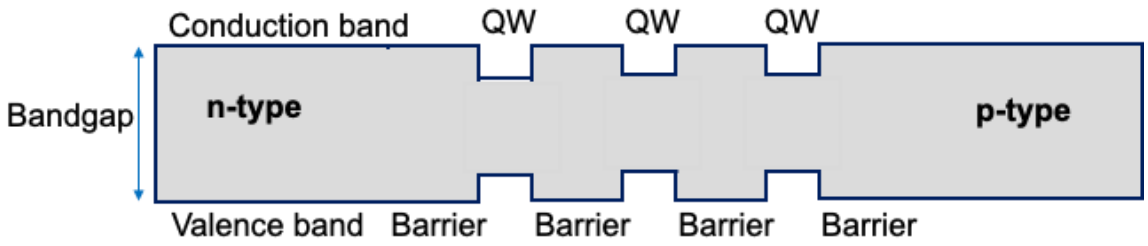

Figure 1.2 The diagram of an LED heterostructure of three quantum wells.

A quantum well can be created by sandwiching a single layer with a lower bandgap energy compound such as InGaN by two barrier layers with higher bandgap energy materials such as GaN or AlGaN. In this way, MQWs are created by repeating the heterostructure of a quantum well. The thickness of the quantum wells and barriers of III-nitride device heterostructures, grown on the wurtzite crystal structure, is in the nanometer range to obtain the high crystal quality and minimize polarization effects.

The IQE of an LED is defined by the number of photons emitting from the active region over the number of electrons injected in the region. If we call τ_r and τ_{nr} the lifetime of the electron for *radiative* recombination and for *nonradiative* recombination, respectively, the probability of an electron for the radiative recombination is τ_r^{-1} and for nonradiative recombination is τ_{nr}^{-1}. The IQE value is calculated by equation (1.3).

$$\eta_{IQE} = \frac{\tau_r^{-1}}{\tau_r^{-1} + \tau_{nr}^{-1}} \quad (1.3)$$

Moreover, due to the internal reflection and absorption within the LED, just a portion of photons created in the active region from *radiative* recombination escapes into the free space. This reduces the LEDs' optical efficiency. The low LEE reduces the LEDs' performance and it is one of the main hurdles for high performance LEDs, specifically for UV LEDs. The LEE is defined by the number of photons escaping into the free space over ones created in the active region. The LEE value denoted as η_{LEE} is calculated by Equation (1.4).

$$\eta_{\mathrm{LEE}} = \frac{\mathrm{P}/\mathrm{h}\nu}{\mathrm{P}_{\mathrm{int}}/\mathrm{h}\nu} = \frac{\mathrm{P}}{\mathrm{P}_{\mathrm{int}}} \quad (1.4)$$

In that equation, *P* is the optical power measured in the free space and P_{int} is the original optical power measured in the active region. The LEE plays a critical role to the contribution of the EQE of LEDs, given by Equation (1.5).

$$\eta_{\mathrm{EQE}} = \eta_{\mathrm{IQE}} \times \eta_{\mathrm{LEE}} \quad (1.5)$$

1.1.2 III-nitride materials

Group III-nitride semiconductors are critical compounds with direct and wide bandgap energy. They have excellent unique properties, such as high electron mobility, extreme chemical stability, and good thermal conductivity [14]. The direct bandgap energy of III-nitride compounds allow them to absorb and emit photons easily. Thus, III-nitride compound semiconductors are ideal for electronic and photonic devices. Shown in Figure

1.3, the energy bandgap of their ternary (AlGaN, AlInN, and GaInN) and quaternary (AlInGaN) alloys can be tuned from 0.69 eV (InN) through 3.40 eV (GaN), to 6.20 eV (AlN) [15-18]. This range of energies is associated with wavelengths from the mid-infrared through the entire visible to deep ultraviolet regions. For that reason, III-nitride compounds have received considerable attention and were developed for LEDs and lasers [19, 20]. GaN generally can be used as a representative for III-nitride compounds. III-nitride or GaN nanowires are used interchangeably in this dissertation.

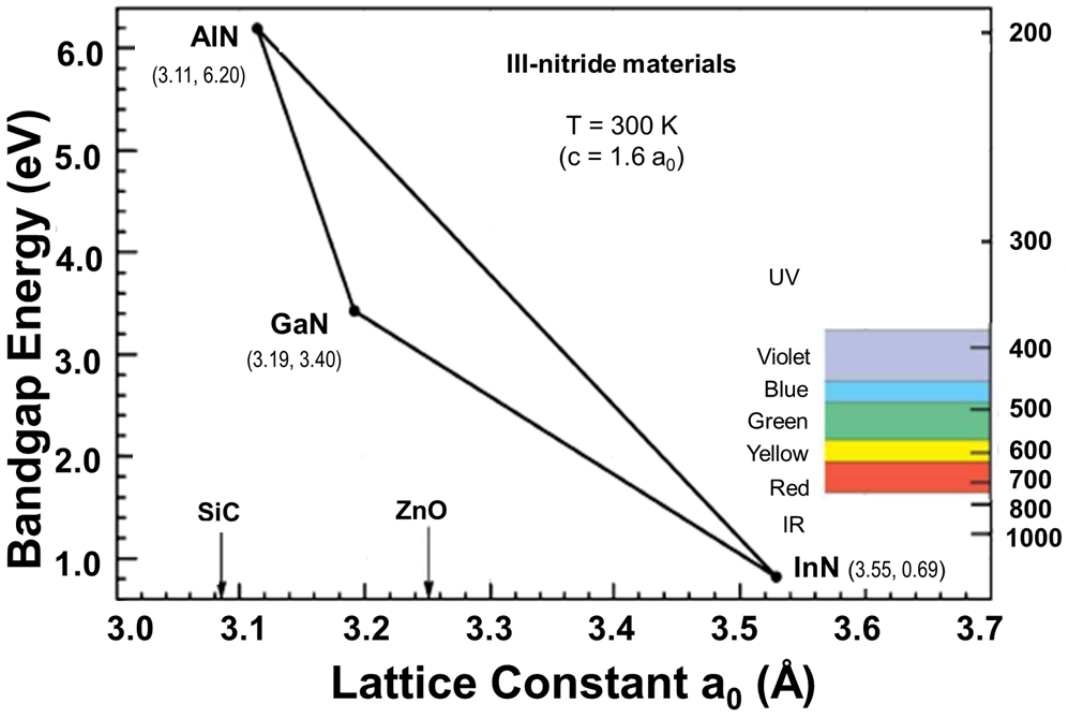

Figure 1.3 The bandgap energy and wavelength versus the lattice constant of III-nitride compounds.

Source: [6].

Due to the lack of the native substrate, conventional III-nitride thin-film heterostructures are synthesized on lattice-mismatched materials such as sapphire, carbide, or silicon. This causes a poor-quality crystal, high density of dislocation, threading defects,

and polarization, which all together severely limit the performance and applications of the devices. In this regard, III-nitride nanowire structures have emerged as an alternative candidate for LEDs with a better performance and novel features [2, 21-28].

Due to the fact that the nanowire structure is 1D (one dimensional) with a high surface-area-to-volume ratio, the strain energy caused by the crystalline mismatch of different materials in heterostructures can be released efficiently into the side wall of the nanowires. Therefore, good quality crystal nanowires can be grown with very low density of threading dislocations and stacking faults [29]. In addition, the sufficient *p*-type doping can be implemented, facilitated by the surface Mg dopant incorporation, compared to epilayers [30-33], addressing the *p*-type doping difficulty. Also, nanowire structures can be easily integrated into very highly flexible photonics platforms using any kinds of substrates, facilitated for novel technologies and applications [23, 34, 35].

1.1.3 Fabrication methods of III-nitride nanowire LEDs

III-nitride nanowires are created by two methods: top-down and bottom-up. Top-down approach utilizes several steps of photolithography and etching to define nanowires from an initial planar structure. Masks are required and play an important role in determination of the resulting nanowire structures. Sometimes, electron-beam lithography is also used to finely define structures at nanoscale [36], enabling precisely direct-writing of nano/micro patterns. However, time-consumption and high equipment cost make it unsuitable for mass production. Self-assembled metal nano-islands were employed to produce a mask of seeding particles on a large area with minimal processing time for the etching process [37, 38]. The pre- and post-treatment procedures are usually required to reduce defects in GaN nanostructures. However, high contaminants, defects, and dislocations in the initial bulk

III-nitride materials limit the material quality of the nanowires, leading to the poor performance of the device.

Bottom-up method, on the other hand, provides high crystalline quality of GaN nanowires due to epitaxial synthesis occurring in the highly controlled vacuum environment, growth temperature, and precursor influx. The high crystal quality of heterostructure nanowires can be achieved in this process using epitaxy processes by the mechanism of vapor-liquid-solid (VLS) with the support of a metal catalyst or spontaneous formation.

1.1.4 Vapor-liquid-solid mechanism

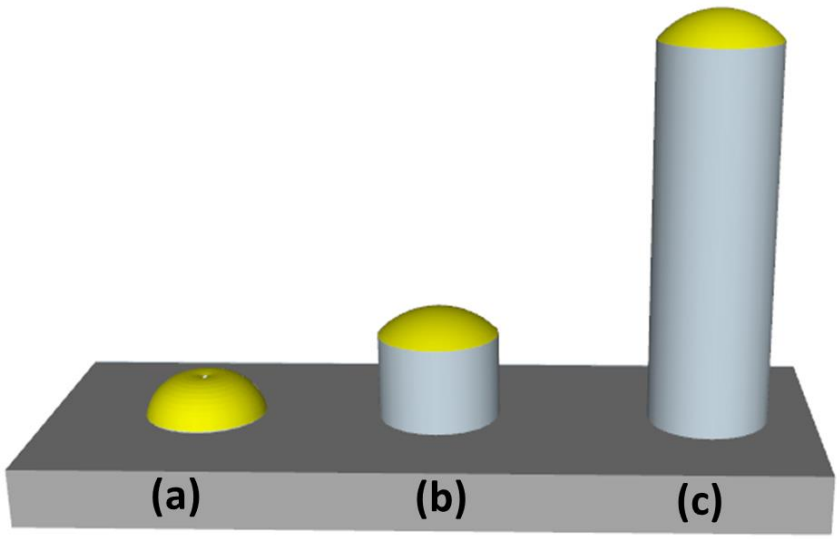

Figure 1.4 Vapor - liquid - solid method for nanowire growth.

The VLS mechanism of the growth of nanowire structures was first reported in the 1960s by Wagner and Ellis [39]. It generally requires a metal particle such as Au, Ni, Pt, etc. to serve as a catalyst from which nanowires are formed and grown. The growth mechanism involves three main phases. The first step begins with the formation of droplets on the

surface of the substrate, shown in Figure 1.4a. Later, the crystal nucleation is formed in the place of the liquid droplets, presented in Figure 1.4b. Finally, when the vapors reach supersaturation with respect to the solid phase, the axial growth of nanowires is dominant, shown in Figure 1.4c. The low solubility of metal particles in growing semiconductor structures is resulted by a low melting temperature eutectic point in the alloy phase diagram. This allows VLS growth around the eutectic melting temperature. The position and diameter of the growing nanowires depend on the position and size of metal particles. Other growth parameters such as the temperature and pressure also have an impact. The length of nanowires is usually determined by growth rate and duration time. Due to the foreign metal catalyst, the grown nanowires suffer a considerable degree of metal contamination, thereby reducing the optical and electrical properties. To prevent the contamination, the mechanism of spontaneous formation was explored to grow nanowires.

1.1.5 Spontaneous formation

Group III-nitride nanowires can be also formed spontaneously under the right conditions within a nitrogen-rich environment without the presence of any foreign metal catalyst. The spontaneous formation is desired for nanostructure growth of high crystalline quality. In this growth technique, the foreign metal catalyst is absent and no catalyst droplet presents at the top of nanowires, as proposed by Bertness [40]. Instead, the nanowire is grown by the differences in the surface energies, sticking coefficient, and diffusion coefficient on the crystal plane. In Debnath's study [41], the diffusion induced mechanism was used to explain the MBE growth of GaN nanowires as shown in Figure 1.5. The adatom diffuses from the sidewall to the top of the nanowires due to the lower chemical potential. The sticking coefficient is much higher on the top of the nanowire than on the sidewall. As a

result, Ga atoms attach directly on the top. In other words, the sidewall tends to desorb rather than absorb Ga atoms. This supports vertically nanowire growth, particularly when the nanowires are growing close to each other. The growth conditions including the substrate temperature and nitrogen flux affect the diffusion process and consequently the growth rate. The top of the nanowires also absorbs the Ga atoms which have desorbed from the nearby nanowires. The nanowires grown by the spontaneous technique result in higher crystalline quality, uniformity, and density than those grown by the VLS technique. Thus, spontaneous growth technique is excellent for the synthesis of optoelectronic devices.

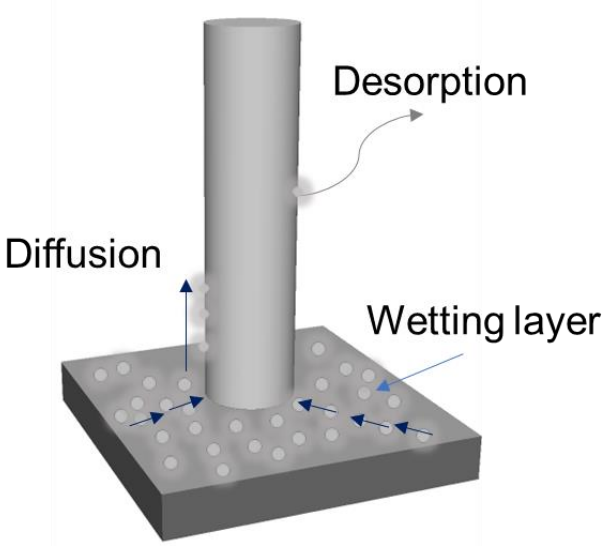

Figure 1.5 The spontaneous formation of a nanowire.

In the bottom-up approach, metal-organic chemical vapor deposition (MOCVD), chemical vapor deposition (CVD), hydride vapor phase epitaxy (HVPE), and MBE are widely used techniques. Among them, MBE growth technique has many advantages in terms of the high level control of purification, composition, and flexible architecture [42, 43].

In an MBE system, group III element metal sources for Al, Ga, and In are placed in the different effusion cells. The metal sources can be heated at high temperatures in the effusion cells to become the metal gases. These metal vapors are then transported into the vacuum growth chamber where they react with the nitrogen precursor right on the substrate and form III-nitride nanostructures. Ammonia (NH_3), or the nitrogen plasma are the nitrogen precursors. The growth rate is slower than other epitaxy methods such as MOCVD and CVD, but the high purity of crystalline structures and composition controllable capability are much better due to the high vacuum growth conditions.

1.1.6 Metal-organic chemical vapor deposition

MOCVD or metalorganic vapor-phase epitaxy (MOVPE) is the conventional epitaxial growth technique which is widely used to grow LEDs [13, 44]. Most of the commercial planar LEDs are grown by MOCVD. The epitaxial growth of LEDs by MOCVD is performed at the high temperature and atmosphere pressure. For instance, III-nitride alloys are grown at temperature from 800-1000 °C [45]. The precursors in MOCVD come from meta-organic compounds. III-elements are usually provided by trimethylgallium (TMG), trimethylaluminium (TMA), trimethylindium (TMI) for Ga, Al, and In, respectively. The nitrogen precursor is provided by NH_3 or nitrogen plasma. The *n*-type doping and *p*-type doping are implemented by Bis(cyclopentadienyl) magnesium (CP_2Mg) and disilene (Si_2H_6). Therefore, the purity of III-nitride structure achieved by MOCVD is theoretically lower than from MBE where pure element sources are used. Also, due to the high-pressure growth condition, gas carriers of N_2 or H_2 are needed for the growth process. The different gases result in different materials morphology [46]. However, the spontaneous mechanism of III-nitride nanowires using MOCVD is not the option for the growth of III-nitride

nanowire LEDs. III-nitride nanowires grown with the spontaneous mechanism result in relatively poor morphology, observed from SEM images [47, 48]. To address poor nanowire LEDs with MOCVD, selective area growth (SAG) has been adopted. The substrate has been patterned in advance. The details of SAG are presented in the next section.

1.1.7 Selective area growth

SAG is an approach using a pre-patterned wafer to allow GaN nanowires to be grown at a highly controllable position and radius. This method could produce a high order uniformity of the nanowires, suited well for the fabrication of high-performance devices. The position and size of nanowires are defined by a pre-patterned mask. The growth duration controls the height of nanowires. The widely used MOCVD and MBE are common tools for the growth of GaN nanowires in this technique. While MOCVD offers a faster growth rate, MBE growth is better in terms of purity, sophistication of the nanowire structures, and high quality crystalline. Silicon, silicon carbide, and sapphire are popular wafers for GaN nanowire growth using the SAG technique.

Several materials of masks and buffer layers have been used to create an initial uniform pattern for GaN nanowire growth [49]. The SAG technique is metal contaminant free during the growth process, and thus the nanowires can be grown with a high level of purity. A layer of GaN or AlN is usually used as the buffer layer for the strain compensation before the mask layer is deposited. The patterns on the mask layer usually are defined by E-beam lithography or photolithography depending on the diameter of the designed nanowires. This is followed by the reactive ion etching (RIE) process to create the openings which define the position of the future grown nanowires. The mask layer is usually titanium

(Ti), silicon nitride (Si_3N_4), or silicon dioxide (SiO_2). Figure 1.6 presents the basic steps for the SAG. A silicon substrate, shown in Figure 1.6a is coated with a SiO_2 mask layer in Figure 1.6b. The pattern is shown in Figure 1.6c in which the openings and spacing are defined by E-beam lithography and RIE. Figure 1.6d illustrates the grown nanowires.

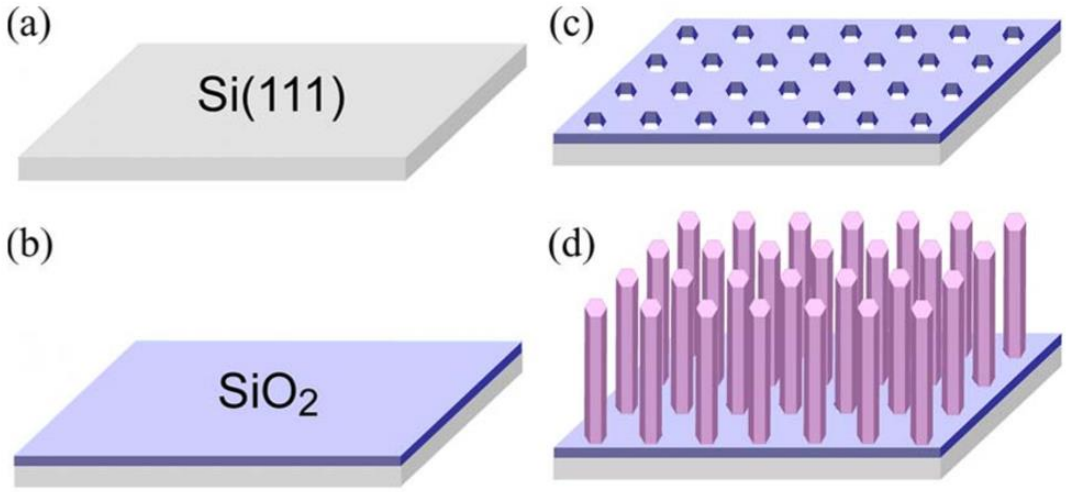

Figure 1.6 Selective-area growth process on silicon wafer with SiO_2 mask.
Source: [50].

Since the last decade, SAG has been used to grow uniform nanowire arrays in a precisely controlled manner of their radius, spacing, density, and height [51]. Stephen *et al.* synthesized GaN nanowires with MOCVD. A layer of 600 nm GaN was deposited as the buffer layer before the deposition of 30 nm Si_3N_4 mask layer. The mask was patterned by the interferometric lithography. Si_3N_4 was deposited on the GaN film by low pressure chemical vapor deposition (LPCVD). The height of GaN hexagonal nanowires is about 1 μm, and the radius is approximately 221 nm. GaN nanowires were then formed by the chemical reaction of the precursors of trimethylgallium (TMGa) and ammonia (NH_3) introduced in the growth chamber.

To study the dependence of the growth rate to the lateral size of openings, the SiO_2 mask layer was patterned with variable apertures at a constant pitch of 2.0 μm by E-beam lithography and RIE. It was found that the growth rate of GaN nanowires is lower on the pre-patterned smaller openings than in the larger ones. This implies the distribution of the precursor is relatively low in the small openings. It also states that SAG is independent of the thickness of the mask layer of SiO_2.

1.1.8 Molecular beam epitaxy growth

Invented over 50 years ago by Arthur and Alfred Y. Cho in Bell Lab [52], MBE technique has evolved to one of the critical methods for semiconductor nanostructure synthesis. Over decades, MBE has had tremendous improvements, well used for the growth of advanced structures such as dot-in-a wire heterostructure for LEDs [53]. The structure of axial quantum wells, radical quantum wells, quantum wires, quantum-dots embedded in nanowires have been demonstrated by using MBE systems [54].

Basically, the MBE system consists of three chambers: intro-chamber, buffer chamber, and growth chamber. A wafer is introduced into the intro-chamber. This chamber's pressure subsequently is evacuated to a *m*Torr level before the valve between the intro-chamber and buffer chamber is opened for wafer transferred into the buffer chamber. In the buffer chamber, the sample shall be baked out in a high vacuum level. Finally, the extremely cleaned sample will be transferred to the growth chamber. Nanostructures are grown in the growth chamber under an extremely high vacuum ($\leq 10^{-8}$ Torr).

MBE growth of III-nitride nanowires is employed by directly introducing group-III elements from effusion cells and nitrogen into the ready-heated substrate. Given that the

growth process occurs in the ultra-high vacuum, the high-quality crystals can be achieved. There are two types of MBE, classified by nitrogen precursors. The ammonia-molecular beam epitaxy (Am-MBE) uses ammonia while the plasma-assisted MBE (PAMBE) employs the nitrogen gas generated by the plasma generator to create the nitrogen plasma. The MBE systems are usually equipped with sensors such as reflection high-energy electron diffraction (RHEED) or mass spectroscopy for *in situ* measurements and investigations. Therefore, the MBE systems have huge advantages in studying growth parameters during the growth process.

In the Am-MBE system, the nitrogen source is introduced in the form of NH_3 gas which is broken down at high temperature. However, the decomposition efficiency of NH_3 largely depends on the temperature. To yield a highly efficient NH_3 deposition, the growth process operates at a high temperature. However, at high temperature, the indium rich III-nitride compounds are hardly stable since indium largely desorbs. Moreover, the remaining NH_3 molecules become an erosive contaminant, causing a big issue in MBE growth. To deal with contamination problems and indium desorption, the PAMBE system is in favor. The nitrogen gas source is introduced and the RF generator is used to create the nitrogen plasma including the mix of (N_2^+), atoms (N), and ionized atoms (N^+). The nitrogen plasma is chemically active, and they can react with group-III elements to form III-nitride nanostructures. The nitrogen influx can be easily controlled by the power of the plasma generator. Therefore, PAMBE is a choice for the growth of high indium nanostructures at relatively low temperature and can avoid contaminant residues. For these reasons, high crystalline III-nitride nanostructures grown by PAMBE growth can be obtained. Beside III-nanowire based LEDs, many research groups have demonstrated lasers [55],

photodetector [56] based on III-nitride nanowires with high quality crystals using MBE technique [57].

PAMBE growth is also employed with a pre-patterned substrate to grow desirable nanowires. The size, density, diameter, morphology, and height of the nanowires can be greatly controlled by the growth temperature and/or the III/nitride ratio. Importantly, the main advantages of MBE growth include the precise control of the influx of precursors, high vacuum, and possible low temperature. This supports the growth of InGaN nanowires with high indium composition in quantum wells.

The initial SAG of GaN nanowires with InGaN/GaN quantum wells by PAMBE was first reported using the patterned mask of Ti layer [58]. Ti-masks have been widely used in GaN nanowire SAG [59, 60]. In that report, the 5 nm Ti film was deposited on a 3.5 μm GaN thin-film and nanoholes were patterned on the Ti layer using the focused ion beam milling. The GaN nanowires were grown at various temperatures from 880 ˚C to 925 ˚C. At 900 ˚C and N_2 flux at 1 sccm, the SAG GaN nanowires were grown uniformly of 183 nm in diameter, 400 nm in space, and 1.5 μm in height. Growth temperature below 900 ºC did not support the GaN nanowire formation, while at higher than 900 ºC, the growth rate was decreased and the GaN nanowires are smaller in diameter. In addition, Schumann et al. have demonstrated SAG of GaN nanowires by PAMBE using SiO_2 mask [61]. The SiO_2 mask layer was deposited on a 10 nm AlN buffer layer from which the pattern of openings of 120 nm in diameter and 0.75 μm pitch were written by E-beam lithography and RIE, respectively. The growth temperature was set at 815 ˚C, 825 ˚C, and 835 ˚C. It was found that GaN nanowire arrays are well grown at 825 ˚C. When the growth temperature increased to 835 ˚C, GaN nanowires are sparely grown across the substrate.

To study the effect of the size of openings on the nanowires, the patterned holes in different diameters were employed. The lateral openings with the diameter below 50 nm support the growth of a single nanowire in the patterned holes. When the hole diameter increased to 140 nm, the nanowires were not uniformly grown. More than 85% patterned openings were occupied with more than one nanowire in a single opening. Similar results were also reported by other studies [62, 63].

Using Si_3N_4 as the mask layer is also common in SAG GaN nanowires by MBE [64]. The Si_3N_4 mask layer was prepared on AlN/Si substrate by the thermal furnace process from precursors of dichlorosilane and ammonia. It was found that if the diameter of openings is smaller than 500 nm, the nanowires grown are hexagonal and uniform. When the openings are larger than 1 μm in diameter, several nanowires were grown within a single opening, indicating some nucleation seedings were formed in advance within a single opening. The photoluminescence intensity of nanowires of 750 nm or larger in diameter is relatively low compared to that recorded from the smaller nanowires. As such, larger diameter nanowires result in lower *radiative* recombination. Moreover, many sub-band emissions were found in nanowires with a diameter higher than 900 nm. This is attributed to the presence of crystalline defects.

Although SAG by MBE growth has numerous advantages, it requires several steps including the deposition of a buffer layer and mask preparation. The whole process needs a variety of instruments such as E-beam lithography, RIE systems, and other equipment for nitride or oxide mask deposition. Therefore, nanowire growth with the SAG MBE technique is not so popular.

In this context, the nanowire growth utilizing the natural self-assembly mechanism becomes a useful method. By carefully controlled temperature and/or the III/nitride ratio, the very high-quality crystal nanowires can effectively be grown on mismatched substrates. In our research, Veeco Gen II PAMBE is integrated with an RHEED system for *in situ* investigation. The Al, Ga, and In sources are contained in the separate effusion cells in which they can be heated to a high temperature to become the metal gases that are flown separately into the growth chamber. The PAMBE system also has effusion cells for the introduction of silicon and magnesium dopants to form *n*-type and *p*-type semiconductors, respectively. The active nitrogen species are supplied by the nitrogen plasma. The growth temperature and influx of precursors are used to control uniformity, density, height, diameter, shape, and alignment of the nanowires. The formation of the high density of nanowires is favored by the low growth temperature since the adatom surface migration can be reduced. Moreover, the substrate orientation is used to control the nanowire alignment. In taking advantages of the Si dominant industry, III-nitride nanowires usually are grown on silicon substrates for the economic reason, mass production, and electronic-photonic integrated platform [61].

1.1.9 III-nitride nanowire LEDs

LEDs based on III-nitride nanowire heterostructures have been intensively studied as an emerging platform for future solid-state lighting, full-color displays, and medical applications. In comparison to the conventional, nanowire-based LEDs present numerous advantages of greatly reduced dislocation densities, polarization fields, quantum-confined Stark effect (QCSE) due to the effective lateral stress relaxation. However, several existing hurdles still limit further enhancement of the quantum efficiency and optical output power

of nanowire LEDs. Some of them are attributed to the lack of carrier confinement in the active region, non-uniform carrier distribution, electron overflow [27], and surface nonradiative recombination [65]. Moreover, the presence of large surface defect densities can cause carrier loss in nanowire LEDs. Consequently, currently reported nanowire LEDs show a relatively low output power. The focus on design, epitaxial growth, post-treatment, and fabrication are needed to achieve high power LEDs in the visible and UV region. The emissive color of the III-nitride nanowire LEDs can be tuned by varying constituent composition of group-III elements in the active region. Other parameters such as the size, space, length of nanowires can also be customized for finely adjusting the emissive spectrum for targeted applications.

1.2 Applications of III-Nitride Nanowire LEDs

1.2.1 Lighting

LEDs are used everywhere today, but the LED technology is still in its infancy. When the price of LEDs is going down and the efficiency is increasing over time, more and more lighting systems made of LEDs are prevalent more than ever before. However, the majority of potential of LEDs is still untapped [66]. According to a report from the Department of Energy in 2017, lighting applications from LEDs will hold 86% in daily lighting by 2035. Huge impacts of LEDs are likely to go beyond the lighting application as a replacement of conventional incandescent. In fact, environmentally friendly, more LED lighting can save energy consumption, benefiting global warming, and reduce carbon footprint. LED lights are practical for zero-energy buildings. Furthermore, due to small turn on electric power, the integration of an LED lighting system with renewable energy sources like solar cells

becomes easy. The ubiquitous renewable energy is a solution to the global warming problem.

As for GaN nanowire LEDs, it might need years to see them in the daily lighting before all supported technologies can reach the level of economic competitiveness. However, initial applications of GaN nanowire LEDs might be found in special lighting environments in theaters and museums, exhibition centers, and showrooms, where the quality and design of lighting systems are critical. More importantly, the high flexibility and miniaturization of nanowire structures make the LEDs to be a promising candidate for many other fields such as μLED displays, precise phototherapy, and bio-imaging.

1.2.2 MicroLED display

Since Apple Inc. acquired LuxVue in 2014, a company developing self-emissive full-color microLEDs (μLEDs) for display technologies, the μLED display has received much attention worldwide. μLED displays basically use the combined red, green, and blue (RGB) μLEDs to be individual pixels. Unlike the organic light-emitting diode (OLED) display technology, the μLED display based on inorganic materials does not degrade over time. The μLED display technologies using full-color μLEDs are advancing not only traditional electronic devices such as TV screens, smartphone screens, but also augmented and virtual reality devices. Historically, display technologies underwent several stages from cathode ray tube (CRT), liquid-crystal display (LCD), conventional LED, and recently organic LED (OLED). In LCD and conventional LED screens, LEDs are used as the backlight sources. In an OLED display, individual RGB OLEDs are self-emissive pixels. But, due to the limitation of organic materials, the OLED screens suffer burn-in effects and the quality of the display reduces over time. μLED display technologies using

inorganic III-nitride materials, however, have a longer lifetime, high energy efficiency, wide color gamut, high-frequency operation. Thus, the μLED displays are predicted as the next ultimate display revolution.

Extensive efforts to create high quality full-color μLEDs and integrate a huge number of RGB μLEDs to form self-emissive individual pixels for μLED displays have been reported. Some techniques are based on quantum dots, resonant nanorings, and strain engineering [67]. The complicated process and introduction of foreign materials in these studies are not in favor of the processing of millions of tiny LEDs. In this regard, monolithic technology has been received considerable attention. The high crystal GaN nanowire LED structures grown on a silicon wafer have a potential in the demonstration of the μLED display. This approach benefits from the integration of electronic platforms to control a massive number of the RGB μLEDs. Currently, several companies such as Aledia and Glo are developing the nanowire based μLED displays. The integration of transistors into the LED wafer to control the μLED individually remains an issue of light modulation of the great number of individual LEDs for μLED displays although recently a practical solution was introduced [68].

1.2.3 Phototherapy

Healing effects of sunlight were well-known thousands of years ago from Egypt, India, and China [69]. In modern life, phototherapy, the study of light for disease treatment, dated back to the early 20th century. Niels Ryberg Finsen was awarded a Nobel Prize in Physiology or Medicine in 1903 for his contribution to the treatment of lupus vulgaris diseases using the ultraviolet light [70]. Since then, phototherapy using artificial light sources has been developing. However, it was not until the invention of laser that

phototherapy received much more attention. Laser allows for a high controllability of the spectrum and intensity of the illumination. In the late 1960s, Endre Mester, a Hungarian physician, conducted several experiments using a low-powered ruby laser illumination at 694 nm to investigate the carcinogenic effects on mice. Surprisingly, the laser illumination resulted in useful effects. The hairs from the shaved-off area were grown more with the illumination than the area without a phototherapy treatment [71]. This became a motivation for medical science study with artificial light.

Recently, LEDs have received tremendous attention due to their significant advantages including long lifetime, high energy efficiency, flexibility, small size, low cost, and chemical and physical stability [72]. Unlike lasers, LEDs are far cheaper, more energy efficient, longer lifetime, and higher flexibility, and more availability of wavelengths. Also, there is no safety regulation with visible LEDs. The III-nitride LED's emissions could be tuned from the ultraviolet throughout infrared. The broad field of irradiation of LEDs is also suitable for a large area illumination. Thus, LEDs are well suited for phototherapy as a light source.

NASA has conducted several experiments on the international space station to explore effects of the LED illumination on plants and animals. For example, mice with the LED illuminations presented five times faster in healing the wounds in the experiment than the mice without illumination. In the microgravity space, red and infrared LEDs at 680 nm, 730 nm, and 880 nm were recorded to boost the cell growth process [73, 74]. Other case studies in the early 2000s showed that the UV LED illumination increases the wound healing progress [75]. Ultraviolet, visible, and infrared LEDs overall induce numerous

biological effects and help normal wounds and chronic wounds to be healed more efficiently [76, 77].

The wound healing effects caused by LEDs, in fact, depend on the illumination intensity and wavelengths. The interaction of photons and the living tissues causes biological effects. If the resulting effects are learnt well in association with the LEDs' illumination wavelengths, phototherapy could become a powerful treatment method for many kinds of diseases. The phototherapy treatment could be achieved due to the quantum mechanism. The illumination photons are only absorbed in association with the shift of electrons between two discrete energy levels in atoms or molecules. Thus, singular energy photons could selectively stimulate a certain biochemical reaction. These reactions occur by the change of electron states within one molecule or between different molecules. Thus, the phototherapy method with multiple wavelength LEDs could become an advanced light source for precision phototherapy. For example, wound healing treatment, which requires the illumination with a wide range of wavelengths from the UV to visible depending on the healing stages [78, 79]. The state-of-the-art combination of a wide variety of narrow spectral LEDs from the UV to visible region would be an extremely practical idea for many targeted biochemical reactions in wound healing processes. Narrow band LEDs can be created by integrated optical bandpass filter structures. Chapter 5 mentions narrow bandpass filters in detail. The fabricated bandpass filters can be integrated onto III-nitride nanowire LEDs to achieve an ultra-narrow emission.

CHAPTER 2

FULL-COLOR INGAN/ALGAN NANOWIRE μLEDS GROWN BY MBE: A PROMISING CANDIDATE FOR NEXT GENERATION MICROLED DISPLAYS

2.1 Introduction

A display using inorganic μLEDs as self-emissive pixels is called the μLED display. This display technology has recently been intensively investigated due to its great potential for tech gadgets such as Apple watches, smartphone screens, television screens, billboards, Google glass, and virtual reality devices. Considerable efforts have been poured into research and development to bring μLED display technologies to the market [80-84]. The increasing demand for μLED displays in high-tech gadgets has received much attention from academia and industry since early last decade. Achieving μLEDs displays requires several critical stages [85] consisting of making μLEDs, transferring them to the backplane, and precisely controlling individual tiny LEDs [86-88]. The first essential step is to have the right RGB μLEDs satisfactory for the μLED display requirements. The μLEDs need a long lifespan, superior brightness, high efficiency, and durability. Different approaches for making RGB and white color μLEDs to form a full-color micro-pixel in the μLED displays were reported [67, 89-91]. The monolithic μLED display based on III-nitride nanowire μLEDs is promising since it allows more direct control of the emissive wavelengths of the LEDs. The emission wavelength of the nanowire μLEDs can be controlled by changing the indium composition in the InGaN active region. This can be executed by adjusting the epitaxial growth conditions including the growth temperature and/or In/Ga flux ratios [92-95]. The energy bandgap of InGaN compounds can be varied from 3.40 eV (GaN) to 0.69

eV (InN) [16], covering the full visible region for display applications. Therefore, GaN based nanowire μLEDs become a potential candidate for developing novel μLED displays [83].

Conventional planar GaN based LEDs are used in everyday lighting and automotive headlights. However, their poor operating efficiency and efficiency degradation in the green to red spectra have limited their potential. The presence of polarization fields [96, 97], Auger recombination [98, 99], poor hole transport [100], defects/dislocations [101, 102], and electron leakage and electron overflow [103-105] are the main causes of these above drawbacks. In this regard, nanowire heterostructures are intensively studied as an alternative candidate for the high efficiency LEDs. Unlike conventional thin-film structures, nanowires exhibit numerous distinct advantages, including dramatically reduced strain-induced polarization fields and dislocation densities due to the effective lateral stress relaxation. Moreover, the micro-size nanowire-based LEDs can be much more efficient in heat dissipation due to the reduced current spreading resistance and thereby resulting in an increase in injection current levels [106-108]. The performance of the nanowire LED is expected to be better than their thin-film counterparts. III-nitride nanowire LED is predicted to be far superior to the OLED and planar LED in terms of reliability, energy efficiency, moisture resistance, and miniaturization [26]. Therefore, nanowire μLEDs have emerged as a promising candidate for display applications. In this chapter, we demonstrated InGaN/AlGaN nanowire μLEDs in different sizes using MBE growth and conventional steps of micro/nano fabrication. Such nanowire μLEDs exhibit strong and stable emissions in visible wavelengths from blue to red colors. Moreover,

phosphor-free white-color μLEDs have also been demonstrated with a highly stable emission.

Generally accepted size of μLEDs is from 100 μm or smaller while mini-LEDs and conventional LEDs are about 100-300 and larger than 300 μm, respectively [109]. One of the first μLEDs was reported by Lin et al, which has an emissive window of 100-200 μm [110]. Later, Jiang et al. demonstrated 15×15 blue μLED arrays and each μLED has 12 μm in the diameter emissive window for blue emission only, not full color [111]. For full color μLEDs on silicon substrates, Liu et al reported μLEDs pixel size of 50 μm and pixel pitch of 70 m [84]. The smaller size of full color μLEDs were demonstrated with quantum dot color converting technology [112]. Also, 75 μm × 75 μm μLEDs were demonstrated with top-down method using conventional nano/micro fabrication process on thin-film planar LED structure [113]. Although the size of μLEDs could be reduced down to 10×10 μm^2 in the lab-demonstrated experiments, the degradation of performance due to surface effects can reduce the reliability of the display [114]. Also, the mass production is challenging. The commercialization of μLED displays still needs years to be widely seen on the market.

2.2 Experimental Details

Vertically aligned InGaN/AlGaN core-shell nanowire μLEDs were grown by PAMBE in a Veeco Gen II system. Silicon and magnesium dopants were doped to grow *n*-GaN and *p*-GaN segments, respectively. During the epitaxial growth process, the nitrogen flow was kept at 1 sccm and the plasma power was controlled at 350 W. The GaN segments were grown at 750 °C, while InGaN/AlGaN quantum wells in the active region were grown at lower temperatures, in the range of 580–650 °C to enhance the indium incorporation. The

nanowire μLEDs consist of GaN:Si grown on a silicon substrate and the GaN:Mg on the top. The ten couples of quantum wells were grown in the active region. Each quantum well includes a 3 nm InGaN dot and 3 nm AlGaN barrier. During growth of the AlGaN barrier, the AlGaN shell is spontaneously formed, enabling unique core-shell layers [115, 116]. The emission color of the μLEDs can be controlled by adjusting the Ga/In flux ratios and the substrate temperature during the MBE growth. For instance, the peak emission wavelengths can be shifted from red to blue by gradually increasing the growth temperature of the InGaN active region from 580 °C to 650 °C with a ramping rate of 10 °C/min. The nanowire length is controlled by the growth duration. Further information of the core-shell nanowire structures and MBE growth can be found elsewhere [116-120].

Figure 2.1a presents the schematic structure of a single InGaN/AlGaN nanowire on a Si substrate. Figure 2.1b shows a scanning electron microscope (SEM) image of InGaN/AlGaN nanowire LEDs taken under a 45° tilted angle. The SEM shows that the nanowires are relatively uniform across the substrate. Figure 2.1c illustrates the microscopic image of the fabricated μLEDs.

The μLED's emissive window has a diameter of 50 μm, which connects with the square electrode pad. The μLEDs were fabricated using standard photolithography, dry etching and contact metallization techniques, which are described elsewhere [27, 95, 119, 121, 122]. During the fabrication process, μLEDs with 30 μm to 100 μm in diameter were defined by standard photolithography. The μLEDs with a diameter of 50 μm were chosen for characterization.

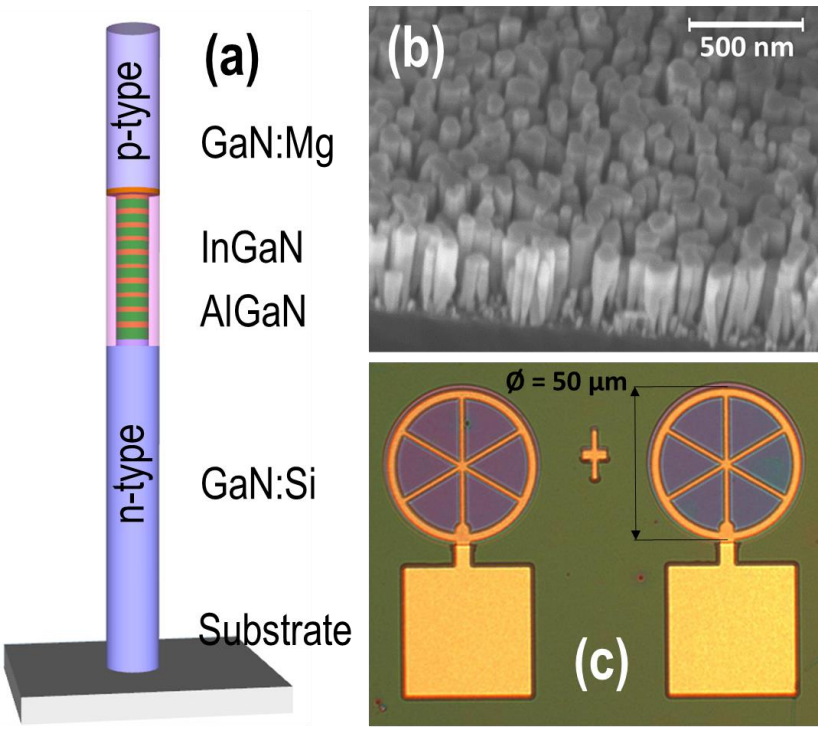

Figure 2.1 (a) Schematic structure of nanowire µLEDs with a ten InGaN/AlGaN quantum well heterostructure; (b) the 45° tilted SEM image of InGaN/AlGaN nanowires on Si substrate; and (c) optical image of µLEDs.

2.3 Results and Discussion

Figure 2.2 shows the normalized photoluminescence (PL) spectra of the InGaN/AlGaN core-shell nanowires. The measurement was performed at room temperature with a 405 nm laser excitation source. It clearly shows that strong red, green, and blue emissions were recorded at 645 nm, 550 nm, and 475 nm, respectively. The current-voltage characteristics of RGB µLEDs were characterized. The turn-on voltages increase with the decreasing indium composition in the active region of the nanowires. The less indium composition, the higher energy bandgap, makes the light emissions shift toward the blue region. The higher energy band gap makes turn-on voltages increase [6], as clearly shown in Figure 2.3. The turn-on voltages of the red, green, and blue µLEDs are approximately 1.6 V, 3.5

V, and 4.6 V, respectively. The I-V characteristics also indicate that the devices with a low resistance and good fabrication processes have been achieved.

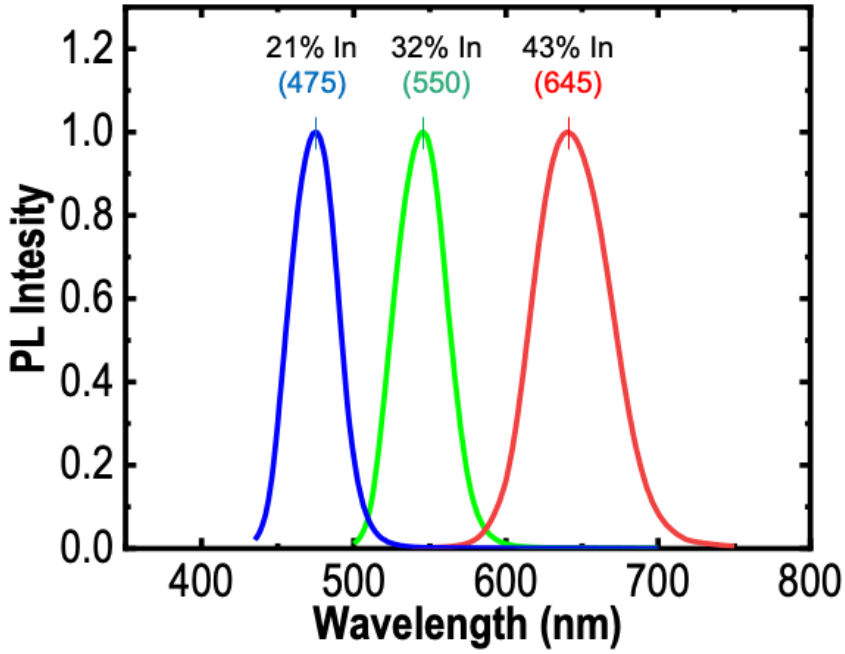

Figure 2.2 Photoluminescence spectra of the red, green, and blue (RGB) InGaN/AlGaN nanowire μLEDs measured at room temperature.

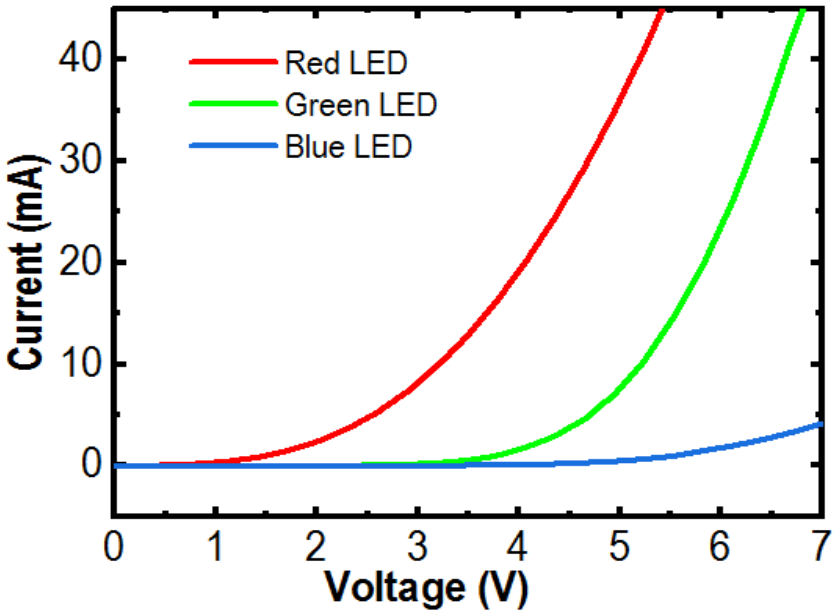

Figure 2.3 Current-voltage characteristics of the RGB μLEDs.

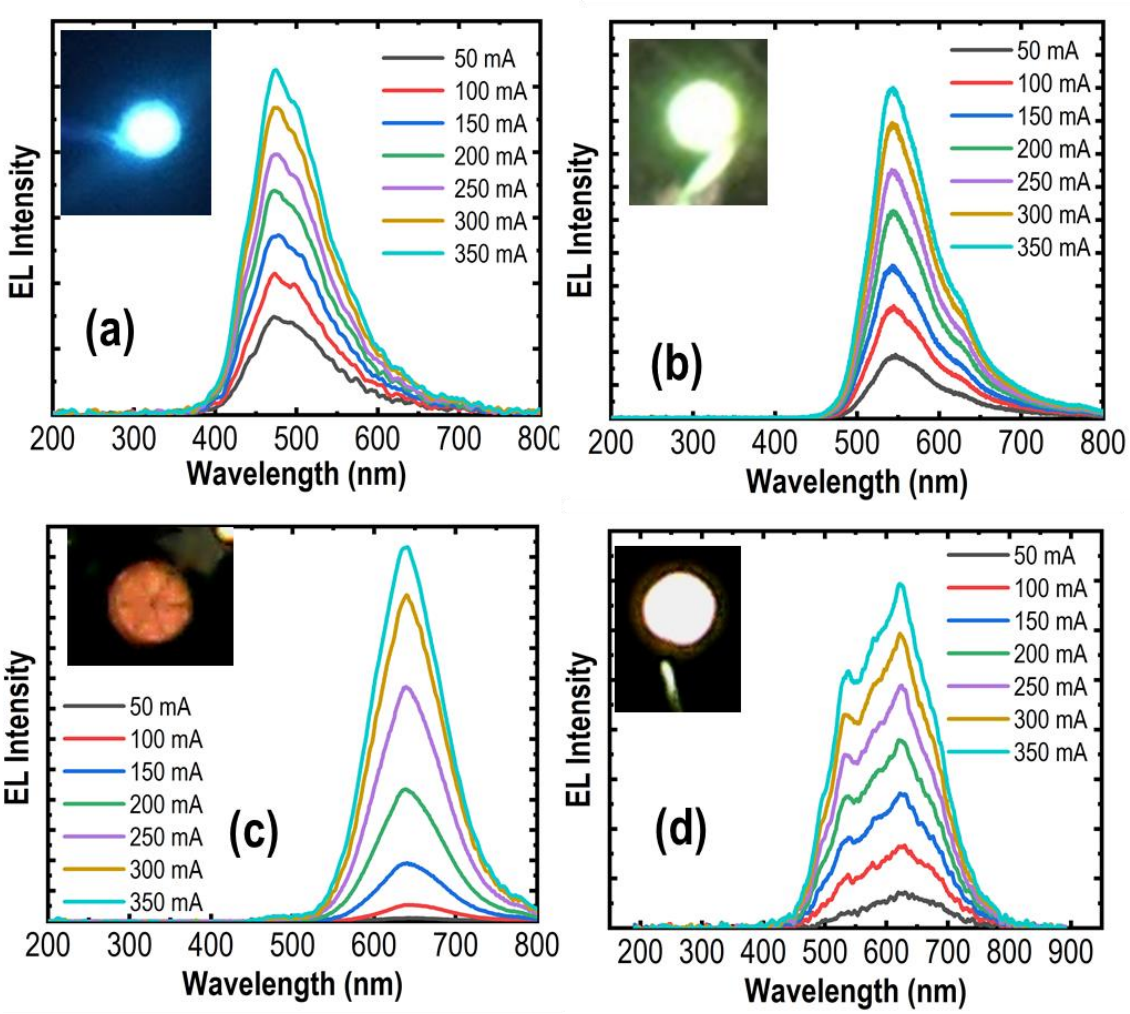

Figure 2.4 (a) The electroluminescence characteristics of the fabricated blue μLED; (b) green μLED; (c) red μLED; and (d) white μLED. The corresponding optical images of these μLEDs are presented in the insets.

The electroluminescence (EL) spectra of these μLEDs are presented in Figure 2.4. The measurements were conducted at room temperature using pulse biasing conditions from 50 mA to 350 mA to reduce the heating effect. Strong red, green, and blue emissions were recorded at 645 nm 550 nm, and 475 nm for the RGB μLEDs, respectively. Illustrated in Figure 2.4a, highly stable emissions with negligible shift in peak wavelengths were measured for the blue μLED with an injection current from 50 mA to 350 mA, attributed

to the greatly reduced QCSE [123] by using nanowire structures. Shown in Figure 2.4b and 2.4c, the blue shifts of about 1.5 nm was measured for the green and 3 nm for the red μLEDs. That values are significantly smaller than those of planar quantum well LEDs operating in the same spectral regime. A summary of the peak emissions of the RGB μLEDs is shown in Figure 2.5.

III-nitride based planar LEDs operating in the green or longer wavelengths are prone to the blue shift with high driving currents due to QCSE [123]. However, using the nanowire structure, the RGB μLEDs have stable center wavelengths at 645 nm in red, 550 nm in green, and 475 nm in blue due to the negligible QCSE, meaning that the lattice mismatch induced strain and efficiency droop are free [124].

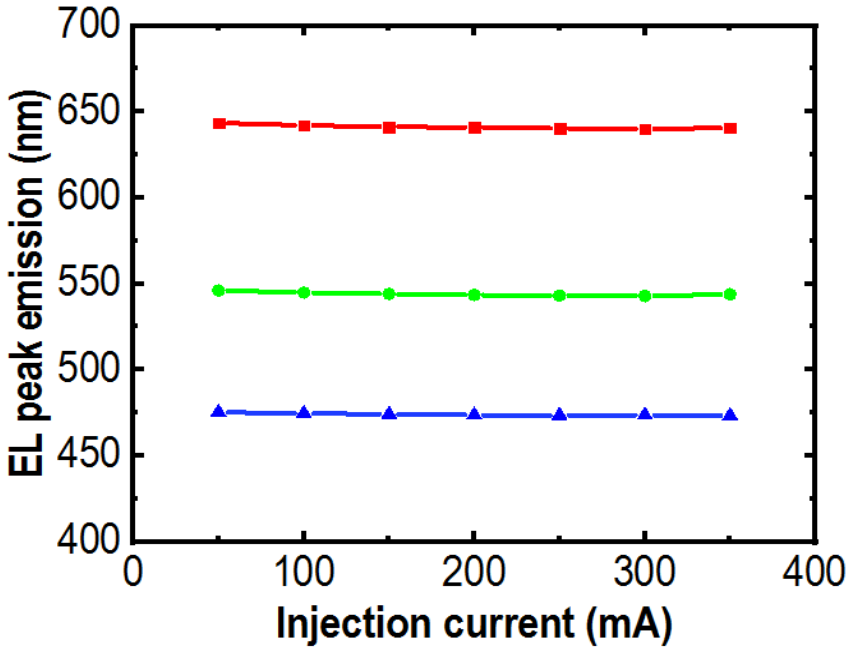

Figure 2.5 The peak emissions of red, green, and blue μLEDs measured under different injection currents from 50 mA to 350 mA.

We have also demonstrated white-color μLEDs with strong emission by engineering the emission wavelength of the core-shell nanowire structure. The white light emission covers an approximately entire range of the visible spectrum from 450 nm to 800 nm. Moreover, the white-color μLED exhibits a stable emission with a small blue shift of ~ 4 nm for injection currents from 50 mA to 350 mA. The stable emission characteristics of the phosphor-free white-color μLEDs are further illustrated in the 1931 Commission International l'Eclairage chromaticity diagram in Figure 2.6.

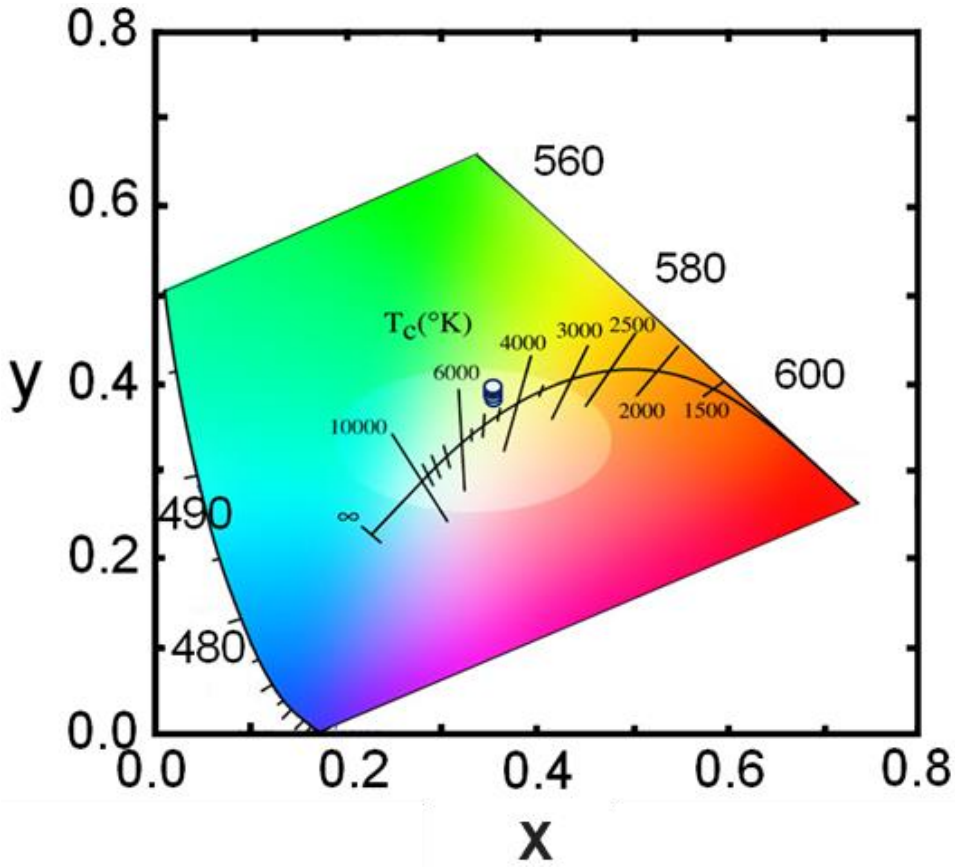

Figure 2.6 The 1931 Commission International l'Eclairage chromaticity diagram presents a stable white light emission of the phosphor-free white-color InGaN/AlGaN nanowire μLED.

The x and y values are derived to be in the ranges of ~0.351–0.362 and 0.391–0.398, respectively. The phosphor-free white-color μLEDs exhibit nearly a neutral white

light emission, with correlated color temperature of ~ 4850 K. Additionally, a very high color rendering index (CRI) of ~ 94 was measured for this phosphor-free white-color μLED, which is extremely difficult to achieve using planar LED structures.

Currently, phosphor-based white LEDs have CRI values in the range of 80–86 [125-128]. With some special design of phosphor converters, the CRI of these types of white LEDs can reach 90–97 [129-133]. However, the complicated fabrication process of these white LEDs and the device reliability are major concerns. To the best of our knowledge, up to this moment, the CRI value for white-color μLEDs have not yet been reported, possibly due to the complexity of the device fabrication for such μLED devices. In this regard, our full-color and phosphor-free white-color μLEDs are highly desirable for the next generation μLED display technology.

2.4 Conclusion

We have successfully demonstrated μLEDs using InGaN/AlGaN core-shell nanowire heterostructures grown on silicon substrates by MBE. Strong and stable emission from full-colors and white-color were recorded from these μLEDs. The color properties of the μLEDs can be optimized by controlling the spectral distribution of the μLEDs. Using nanowire structures, we have achieved phosphor-free white LEDs with unprecedentedly high CRI of ~ 94. The high performance and stable operation of the RGB μLEDs show promise in monolithic μLED displays. Generally, the high cost of current displays is a bottleneck for the market growth. Due to the progressive demand for electronic devices, it is expected to provide lucrative growth opportunities for the micro-display market. In this regard, using the selective area growth approach, RGB subpixel μLEDs can be integrated

on the same chip, eliminating the current pick-and-place process, which requires precisely controlling procedures. Therefore, high efficiency, high color rendering properties, and low power consumption μLEDs using GaN nanowire heterostructures are perfectly suitable as an alternative replacement of current display technologies.

CHAPTER 3

AlGAN NANOWIRE ULTRAVIOLET LEDS

3.1 Introduction

Ultraviolet light with wavelength from 10 nm to 400 nm is the electromagnetic waves staying in between the X-ray and visible region. Ultraviolet light is well known with considerable applications in water and wastewater sanitation [4], disinfection [1, 7, 134], polymer curing [135], non-destructive investigation [136], food technology [3], agriculture [5]. The conventional UV light sources are mostly based on mercury vapor lamps and gas discharge lamps. These lamps are bucky, high energy consumption, short lifetime, limited in wavelengths, and non-flexibility. Therefore, the search for a new type of UV light sources is essential for bringing benefits of the UV technology to human life. UV LEDs have been emerging not only as a replacement of the conventional UV light sources, but also as a drive force for UV based novel applications. Compared to conventional UV light sources, UV LEDs offer many advantages such as compactness, fast turn-on, low energy consumption, long lifetime, high flexibility, and environmentally friendly. The UV LED helps to cut the cost of UV light source production and provide a wide range of novel applications.

Figure 3.1 presents numerous applications from AlGaN UV LEDs. In this chapter, the study focuses on UV LEDs operating at wavelengths from 290 nm to 330 nm. These UV LEDs are very useful because, as UVB region, they are beneficial for vitamin D deficiency [137] and widely used in phototherapy [138], in bacteria disinfection [1], and money validation [139].

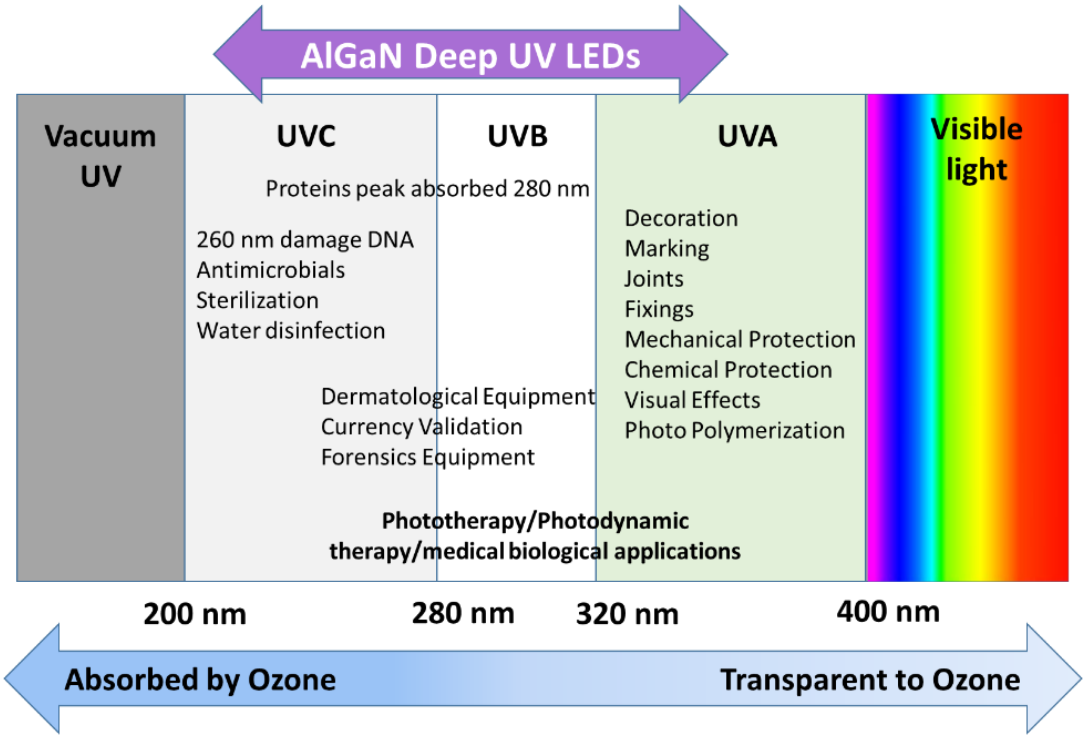

Figure 3.1 Applications of ultraviolet light in different wavelength regions.

Among some materials for UV LEDs such as ZnO [140], III-nitride alloys are the most promising candidate for UV emitters and AlGaN is the material of choice due to its inherently wide tunable bandgap energy. When the bandgap energy of $Al_xGa_{1-x}N$ varies in the range of 3.40 eV (GaN) to 6.20 eV (AlN), the corresponding wavelengths are from 207 nm to 365 nm, respectively [15]. The energy bandgap of $Al_xGa_{1-x}N$ is estimated from the formula:

$$E = xE^{AlN} + (1-x)E^{GaN} - bx(1-x) \qquad (1.6)$$

Where bowing parameter, b = 0.94 is chosen [141].

The UV LEDs have been found for a wide variety of potential applications in healthcare, water purification, disinfection, and spectroscopy [142]. However, as shown in

Figure 3.2, current UV LEDs have low EQE due to a low IQE and LEE [27, 143]. The reported EQE of UV LEDs operating below 300 nm is smaller than 10%, preventing UV LEDs from becoming a replacement for the bulky mercury-based UV lamp for tremendous practical applications. Therefore, the successfully developed high-efficiency AlGaN UV LEDs are considered the next disruptive technology for solid-state lighting after the visible white LEDs.

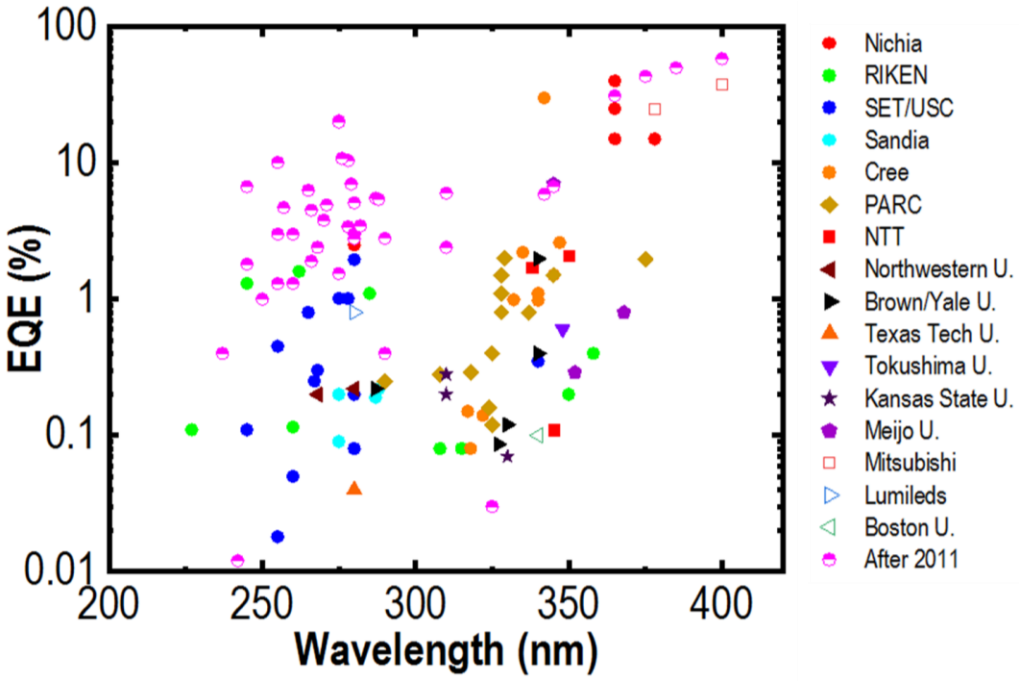

Figure 3.2 The low EQE of UV LEDs, adopted before 2011 and additionally updated values.
Source: [135]

Given in Equation (1.5), EQE is directly proportional to IQE and LEE. To have a high value of EQE, the idea is to increase IQE and LEE. To improve IQE is strictly related to several factors such as crystalline quality, carrier density in the active region, heat effect,

polarizations, and current spreading. All these factors are remaining issues in the synthesis of the LED structure and fabrication processes [2], but we can improve EQE through LEE.

Due to the multiple internal reflection and high absorption, UV LEDs suffer from low LEE, especially from planar UV LEDs. UV LEDs emit photons from the active region in two modes: transverse magnetic (TM) and transverse electric (TE) fields. The TM emissions are photons propagating along in a horizontal direction. Photons in the TM mode emission have the electric fields parallel to the axial nanowire. The TE mode, on the other hand, propagates along the vertical directions with oscillating electric fields parallel with the plane of the substrate (c-plane). Since the TM mode emissions become dominant in high Al-rich III-nitride composition UV LEDs, the increasing internal reflection and absorption become an issue, reducing LEE.

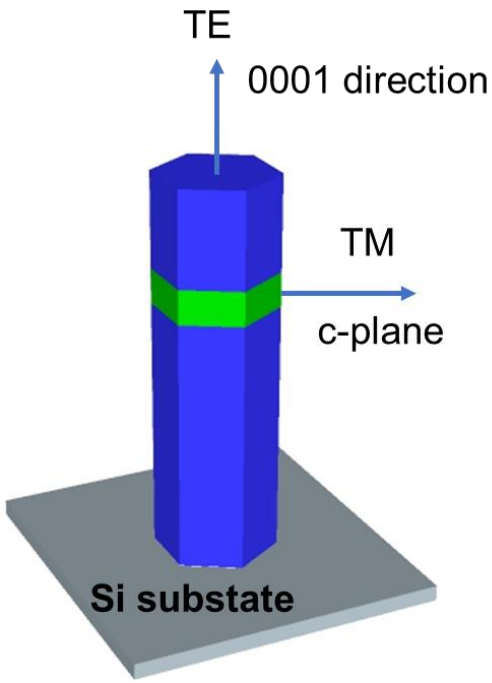

Figure 3.3 The TM and TE mode of the light emission in nanowire LEDs.

There are several methods to improve LEE. The patterned substrates [144], rolled up nanotubes [145], surface roughing [146] and photonic crystal patterns [147] have been used to enhance the LEE of UVB LEDs. With nanowire UV LEDs, the nanowires could be implemented as a photonic structure when using periodic nanowires to increase the LEE [148]. Herein, we present the numerical investigation of the periodic nanowire structure as a photonic crystal to improve the LEE.

3.2 Simulation and Experiment

We show the method for optical enhancement of nanowire UV LEDs using periodic photonic structures and demonstrate AlGaN nanowire UV LEDs with MBE growth. The AlGaN nanowire heterostructures were grown on <111> Si substrates by the PAMBE system under nitrogen rich conditions. Figure 3.4 depicts the schematic structure of the GaN/AlGaN UVB LEDs on Si substrate and the photonic crystal of square nanowires in finite-difference time-domain (FDTD) Lumical simulation. The LEE values from 19 random photonics crystals of nanowires were also calculated for the comparison.

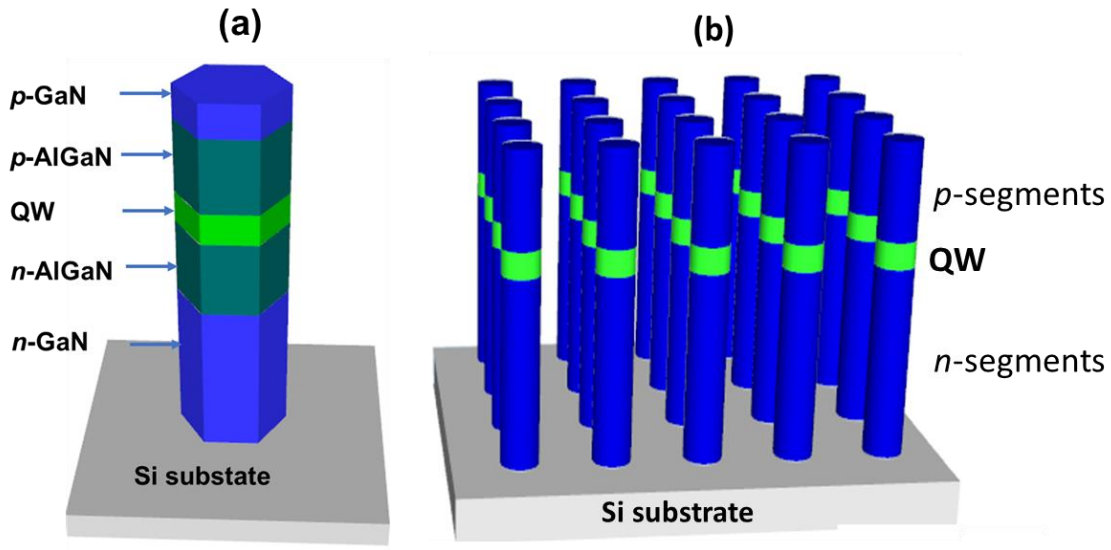

Figure 3.4 (a) The illustration of the AlGaN UVB nanowire on silicon substrate; and (b) an array of LED nanowires.

The LED device of a rectangle array of the nanowires with the size of 2.5 μm × 2.5 μm, shown in Figure 3.4b. The device is enclosed by perfectly matched layers (PML) to absorb the emission photons without any unexpected reflection off the boundaries [149]. The PML has sigma and kappa factors of auxiliary attenuation coefficient set at 0.25 and 2, respectively. The meshing was set at 0.25 nm [150]. The light source is a single Gaussian spectral dipole. It is inserted in the middle of the device and at the active region of the center nanowires. The dominant TM mode polarization in UV LEDs is taken into account in the simulation [148]. To optimize nanowire parameters of UVB LEDs for the highest output power, the radius of nanowires and center-to-center (c-c) spacing are varied from 49–69 nm and 165 nm – 200 nm, respectively. The calculated LEE values of square photonic crystals and random nanowires are presented in Figure 3.5.

3.3 Results and Discussion

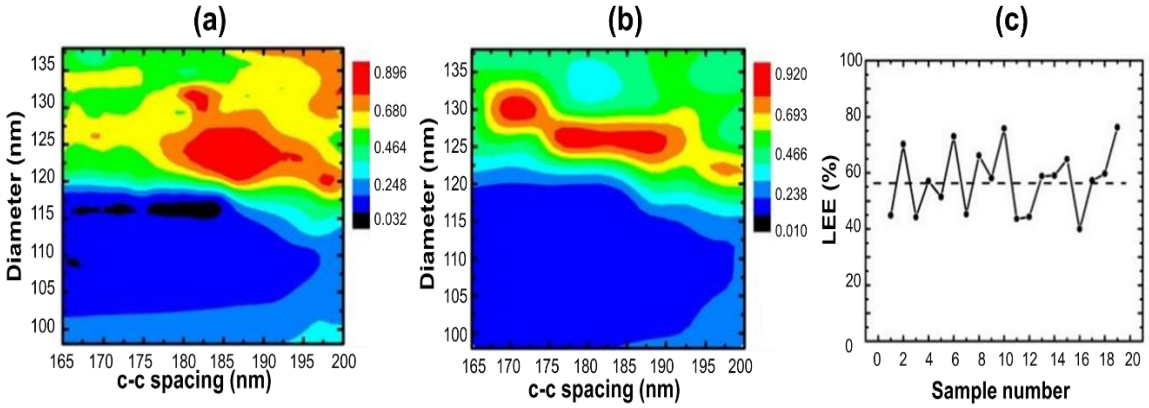

Figure 3.5 (a) The contours of LEE of the 290 nm; (b) 320 nm LEDs with the changing diameter versus c-c spacing; and (c) LEE values of LEDs with the random nanowire structures.

Different arrangements of LED nanowires were studied. The numeral investigation shows that the UV LEDs based on periodic nanowire structures result in a LEE as high as

~ 90% and 92% for 290 nm and 320 nm UV LEDs, respectively. LEE from the UVB LEDs made of random nanowires is relatively as low as ≈ 56%, but it is still higher than the value recorded from the AlGaN planar counterpart at the similar emission.

The contours show that the LEE of 290 nm UVB LEDs is as high as 90% in Figure 3.6a, which was acquired at a c-c spacing of ~186 nm and nanowires' diameter of 125 nm. Similarly, LEE of ~92% was calculated for 320 nm UV LEDs when the diameter of the nanowires is from 125 to 130 nm and the c-c spacing value is from 170 nm and 190 nm, shown in Figure 3.6b. The LEE of both types of the UV LEDs are higher than that recorded from 19 random structures. The enhanced LEE values especially from the lateral sides of the nanowires arise due to the mode coupling within the nanowires. During the generation of coupled modes, photons propagating horizontally through the nanowires can be easily extracted. The simulation of different nanowires' morphology points out the optimal diameter as well as the spacing between nanowires for the highest LEE.

Based on simulation results, the MBE growth was controlled for achieving AlGaN nanowires with diameter in the range of maximum LEE. The distance between nanowires only can be controlled with SAG which is one of our future work. The diameter and density of the nanowires in this study were controlled by the substrate temperature and Al/Ga flux ratios. The nanowire height was defined by the growth duration. The Al/Ga ratio and/or growth temperature conditions were used to control AlGaN nanowires.

The SEM of AlGaN nanowires is shown on Figure 3.6 where they are relatively uniform across the substrate. The nanowires consist of 250 nm *n*-GaN in the bottom, followed by 100 nm *n*-AlGaN segment and 60 nm quantum well (QW) active region. On the top of the quantum well is 100 nm *p*-AlGaN and 10 nm *p*-GaN. The samples then were

fabricated. The device fabrication of AlGaN UVB nanowire LEDs began with the planarization and passivation. The whole fabrication process is presented in Figure 3.7.

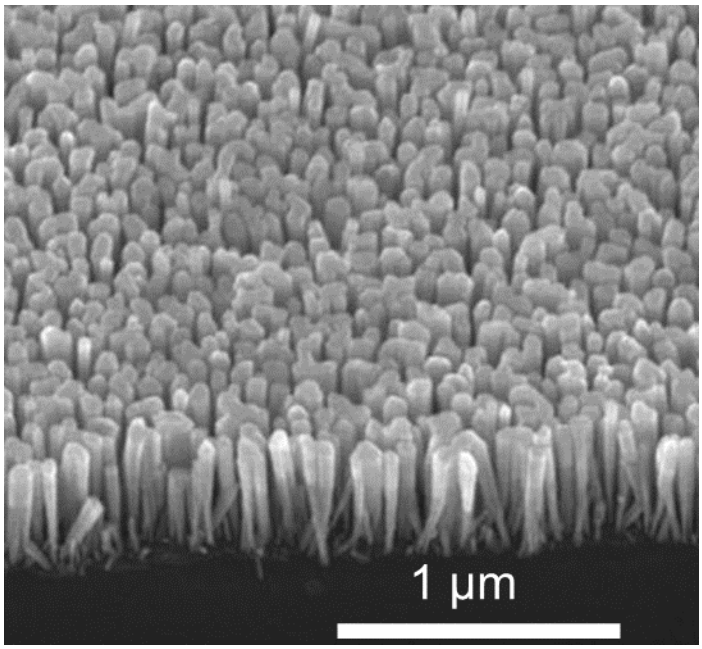

Figure 3.6 The 45° tilted SEM image of the AlGaN UV LED

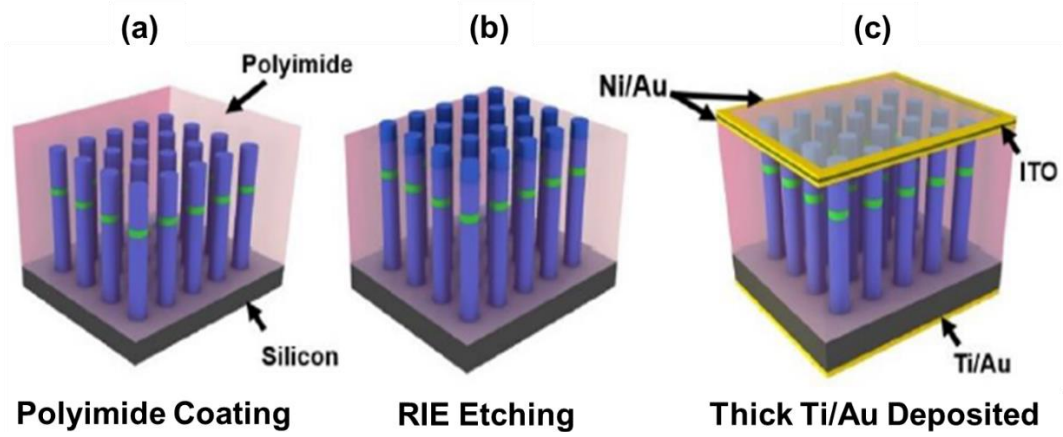

Figure 3.7 The fabrication of nanowire UVB LEDs on silicon substrate.

The nanowire array was spin-coated with the polyimide resist, illustrated in Figure 3.7a. This was followed by O_2 dry etching to expose the top portion of the nanowires,

shown in Figure 3.7b. The metal contact layers including 5 nm Ni/5 nm Au /150nm (ITO) were then deposited to form the top metal contacts. 10 nm Ti/100 nm Au and metal-grid 10 nm Ni/100 nm Au layers were then evaporated on the backside of the Si substrate and top of ITO to form the contacts in both sides, shown in Figure 3.7c.

Optical properties of UV LEDs were examined using a 266 nm laser diode as the excitation source. The duration, maximum energy, and repetition rate of the laser pulse were set at 7 ns, 4 uJ, and 7.5 kHz, respectively. To eliminate light intensity from the laser source, a long pass filter (> 270 nm) was placed in front of the spectrometer. The normalized PL spectra of multiple AlGaN UVB nanowire LEDs measured at room temperature show emissive peaks at 290 nm, 300 nm, 320 nm, and 330 nm, presented in Figure 3.8.

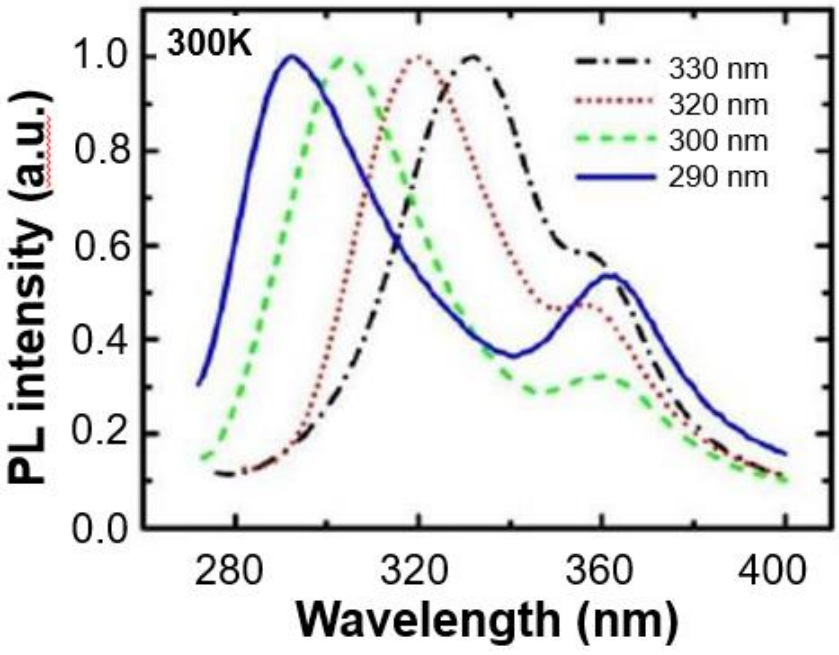

Figure 3.8 Photoluminescence of nanowire LEDs with the peak wavelengths of 290 nm, 300 nm, 320 nm, 330 nm at room temperature, respectively.

As seen from the corresponding plots, these emissive peaks match the designed wavelengths of the light excited from the nanowire LEDs. Expected Al composition in the AlGaN wells was achieved by keeping the growth process at different temperatures and/or changing the flux ratio of Al/Ga. A higher Al percentage achieves a shorter wavelength of UVB LEDs. Thus, emissions from 290 nm to 330 nm were realized as increased Al composition in the active regions.

The EL spectra from device area of 500×500 μm^2 were measured at room temperature using the Ocean Optics spectrometer (USB 2000) at injection currents from 50 mA to 400 mA under pulsed biasing conditions (~1% duty cycle) to minimize the junction heating effect.

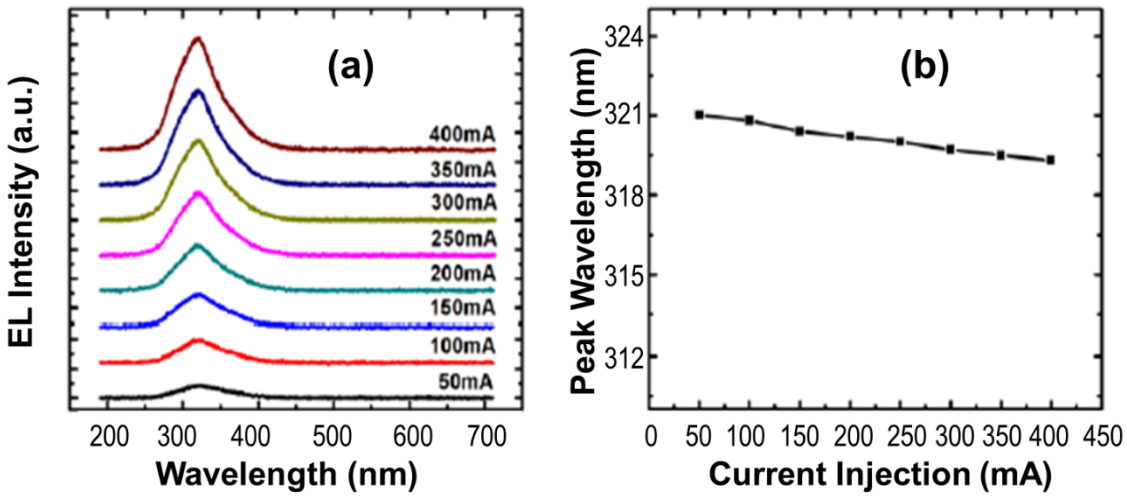

Figure 3.9 (a) The electroluminescence of the AlGaN nanowire UVB LED with emission at 320 nm under injection currents from 50 mA to 400 mA by step 50 nm; and (b) variation of peak wavelengths at different current injection levels.

The EL spectra exhibit a singular peak at around 320 nm which corresponds to the emission from the AlGaN quantum well, shown in Figure 3.9a. Additionally, illustrated in Figure 3.9b, the emission peaks are similar, as the injection currents were increased from

50 mA to 400 mA. The EL spectra show the negligible blue shift under that range of injection currents. The very small shift of about 1.5 nm emphasizes the absence of the internal polarization field due to the effective strain relaxation. It can be observed that the device shows a stable and strong emission at 320 nm regardless of injection currents without any noticeable emission due to the deep level defects in AlGaN [151, 152].

The current-voltage characteristic of the UVB LEDs is depicted in Figure 3.10. The fabricated UVB LEDs by MBE growth presents a relatively low resistance with an excellent current-voltage characteristic. The defect density, QCSE, and polarization field are minimized in the nanowires, resulting in perfect performance of the UV LEDs with a very low leakage current of <1mA at a reverse voltage of ≈ -6V. The sharp increase of the current in the forward bias confirms the excellent current-voltage characteristic with a low resistance. The leakage current can be attributed to the leakage paths due to the inadequate insulation between the nanowires and polyimide resist as well as carrier *nonradiative* recombination occurred on the surface of the nanowires [37].

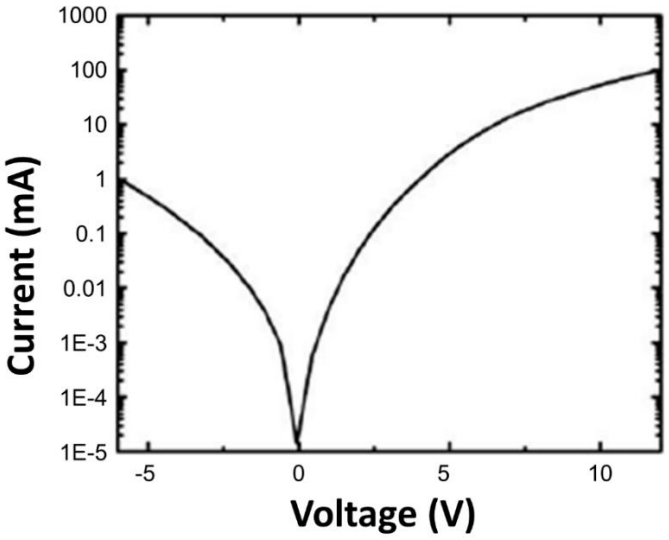

Figure 3.10 Current–voltage characteristic of the AlGaN nanowire LED.

3.4 Conclusion

In summary, high performance AlGaN nanowire UVB LEDs grown on silicon substrate have been demonstrated. The LEE of the UVB LEDs with square photonic crystals is significantly improved, compared to the random nanowires. The UV LEDs hold the strong EL intensity with an unnoticeable blue shift. This study has a contribution to addressing some of the major issues existing in planar UV LEDs to improve EQE of AlGaN UVB LEDs. These high efficiency AlGaN nanowire UVB LEDs are highly potential for novel practical applications.

CHAPTER 4

HIGH EFFICIENCY NANOWIRE UVA LEDS BY SURFACE PASSIVATION

4.1 Introduction

Previously mentioned in Chapter 3, as a solid-state light source, UV LEDs have several advantages over the traditional mercury-vapor UV lamps such as compactness, high mechanical and chemical stability, low power consumption, and long lifetime [135]. The AlGaN compound has drawn significant attention for making UV LEDs because their wide direct bandgap energy can be finely tuned from 6.20 eV (AlN) to 3.40 eV (GaN) [17, 18] by varying the Al and/or Ga contents. The corresponding emission wavelengths of AlGaN LEDs virtually cover the entire UV regime from 206 nm to 365 nm. Similar to the visible LEDs which have with numerous practical applications such as general lighting [24, 153], displays [28, 109, 154], agriculture [155] and food processing [3], the UV LEDs can be considered for a wide variety of potential applications including airborne surface disinfection [60], water purification [156], food processing [10], medical applications [157], nondestructive inspection, photopolymer curing, and spectroscopy [8, 158]. However, due to the lack of the native substrate, AlGaN thin-film UV LEDs are usually grown on lattice-mismatched substrates such as silicon, sapphire, or silicon carbide. The differences in the lattice constants and thermal coefficients between the substrate material and AlGaN make the grown structures usually present high threading dislocations (TDs) [159, 160]. The difference in crystal constants between AlN and GaN also causes high mismatched induced polarization and TDs within AlGaN epilayers [161-164]. Moreover,

inefficient *p*-doping in Al-rich AlGaN due to the high Mg activation energy remains a bottleneck in achieving high efficiency AlGaN UV LEDs [165-167]. These drawbacks lead to significantly low IQE [168]. Furthermore, internal absorption and high internal total reflection reduce the LEE of such AlGaN UV LEDs [28, 135, 169, 170]. Although significant efforts to improve IQE [171, 172] and LEE [173, 174], the overall EQE of the planar UV LEDs given by Equation (1.5) (EQE = IQE×LEE) is still very low, compared with the visible LED's [8, 175]. For instance, the EQE of UV LEDs with the emission wavelengths around 300 nm can reach up to nearly 10%. However, the EQE of UV LEDs with emission wavelength below 300 nm decreases dramatically from less than 4% to ~0.04% [160], which is extremely low for practical applications [176-178]. In this context, AlGaN nanowire structures have emerged as a promising replacement owing to their advanced properties. III-nitride nanowires present nearly free dislocations and reduced piezoelectric polarization [22, 179] owing to their effective strain relaxation. Furthermore, MBE grown AlGaN nanowires have demonstrated a reasonable *p*-type [33], LEE [180], effective thermal dissipation, and reduced polarization. Consequently, high efficiency AlGaN UV LEDs can be achieved with the nanowire structures [181].

However, because of the high surface to volume ratio, the surface states such as dangling bonds [182] and surface Fermi level [183, 184] greatly contribute to high surface nonradiative recombination of the nanowire LEDs [185, 186], thereby reducing the performance of the AlGaN nanowire UV LEDs [22]. The surface passivation is used to reduce surface defects, deactivate surface dangling bonds to improve the overall power efficiency, reliability, and durability of the AlGaN UV LEDs.

4.2 Surface Passivation with Si_3N_4 and SiO_2

The Si_3N_4 and SiO_2 are common surface passivation materials in semiconductors. They have been used for many semiconductor devices including GaN Schottky diodes, heterostructure field effect transistors, and metal-insulator semiconductor (MIS) structures [187]. The surface passivation with Si_3N_4 and SiO_2 has been reported for gaining an enhancement of the photoluminescence intensity for the GaN surface and reducing the leakage current [187]. When Si_3N_4 passivation was used, the band-bending of the GaN heterostructures was reduced [188], proved by the X-ray photoelectron spectroscopy (XPS) characterization. A layer of Si_3N_4 passivation prepared by sputtering has seen an increase in the operation stability of GaN LEDs at high temperature [189]. However, another study has indicated that hydrogen-free Si_3N_4 deposition conditions should be implemented otherwise the reduced emission efficiency of the passivated GaN LED [190]. When SiO_2 was used for GaN nanowire surface passivation, the blue LEDs result in an increase in optical power and reduction in the leakage current [191]. Despite the limited understanding of the underlying mechanism of passivation, the enhancement of optical and electrical properties of the GaN devices could be attributed to the diminished dangling bondings and oxides in the UV LEDs [22].

GaN nanowire LEDs grown on Si substrates obtain a high material quality, dislocation free, polarization free due to the laterally released strain towards the nanowire sidewalls. However, due to the high surface-to-volume ratio of nanowires, the surface nonradiative recombination caused by the surface defects is high, reducing the total optical efficiency of the LEDs. Furthermore, donor bound excitons proximity the surface [192] and band energy bending because of the Fermi level pinning at the surface [193] are other

issues. In this study, we numerically studied the passivation of the GaN nanowire LEDs with Si_3N_4 or SiO_2 layers to increase the optical power efficiency and reduce the leakage current.

4.3 Surface Passivation with KOH and $(NH_4)_2S_x$

Wet chemical surface passivation is a relatively simple method. It has been demonstrated to reduce the surface nonradiative recombination from III-nitride devices. Biswas et al. performed AlGaN nanowire surface treatment with phosphoric acid (H_3PO_4) [194]. They found that the suppression of the surface states increases the performance and carrier lifetime of nanowire UV LEDs. Moreover, Zhao et al. reported that Octadecylthiol and Ammonium Sulfide $(NH_4)_2S_x$ passivation could mitigate Shockley-Read-Hall nonradiative recombination in InGaN/GaN disk-in-nanowire LEDs [22]. $(NH_4)_2S_x$ was used to passivate the nanowires with an aim at deactivating dangling bonds, adjusting Fermi level pinning, and protecting the nanowires from being oxidized again. Sun et al. found that Potassium Hydroxide (KOH) solution treatment can improve AlGaN UV LED's luminescence by the removal of the natural oxides and Al-rich AlGaN shell layer on nanowires' surface [115, 195]. Nguyen et al. also reported that using $(NH_4)_2S_x$ solely can increase the efficiency of white InGaN/GaN dot-in-a-wire LEDs [122].

4.4 Surface Passivation of AlGaN Nanowire Ultraviolet LEDs

First, we have numerically investigated SiO_2, Si_3N_4, and $(NH_4)_2S_x$ surface passivation for III-nitride nanowire LEDs using the FDTD method. The simulated results show that

nanowire UV LEDs with $(NH_4)_2S_x$ passivation have the highest LEE. Therefore, $(NH_4)_2S_x$ is selected for further experimental process. The passivation with a combination of KOH and $(NH_4)_2S$ has been conducted on AlGaN nanowire UVA LEDs. The performance of the 335 nm AlGaN nanowire LEDs after passivation is significantly increased.

4.4.1 Simulation

Nanowire LEDs are assumed to be filled up with the passivation layers of SiO_2, Si_3N_4, and $(NH_4)_2S_x$. We calculated the LEE of the GaN nanowire LEDs using the commercial FDTD Lumerical software. The FDTD method solves the Maxwell equations for electromagnetic waves in real time-space.

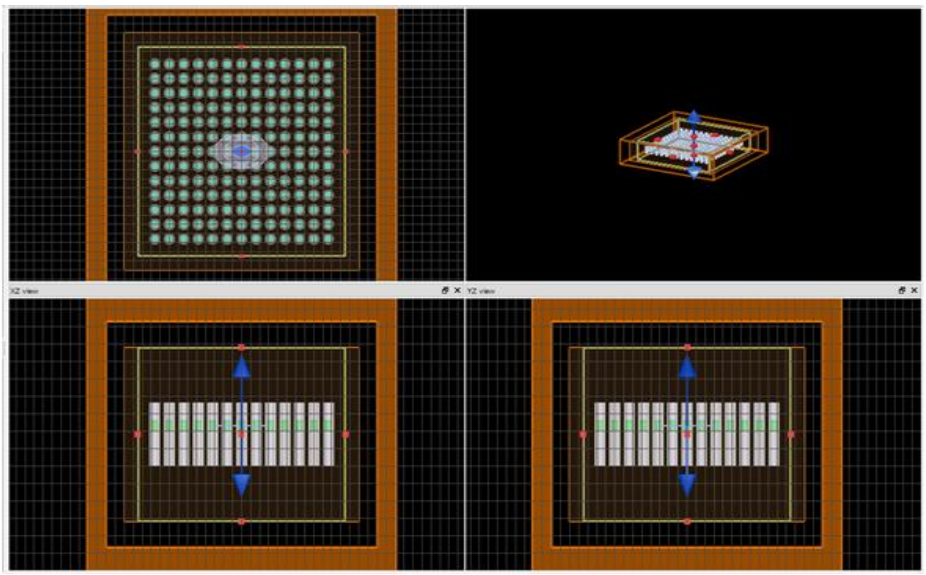

Figure 4.1 The FDTD simulation implemented with square nanowire structures.

The thickness of Si_3N_4 and SiO_2 were adjusted to fill the entire empty space between the nanowires. A dipole light source at 335 nm was inserted in the active region of the LED nanowire. The passivation calculation in three different nanowire

arrangements: random, square, and hexagonal structures. The refractive indices of Si_3N_4, SiO_2, and $(NH_4)_2S_x$ are 2.14, 1.48, and 1.47, respectively. Figure 4.1 shows the FDTD simulations structure. The LEE was recorded with the detectors around the structure and simulation time was set up to 2000 picosecond. The obtained findings from the simulation are helpful in the design and implementation of experiments.

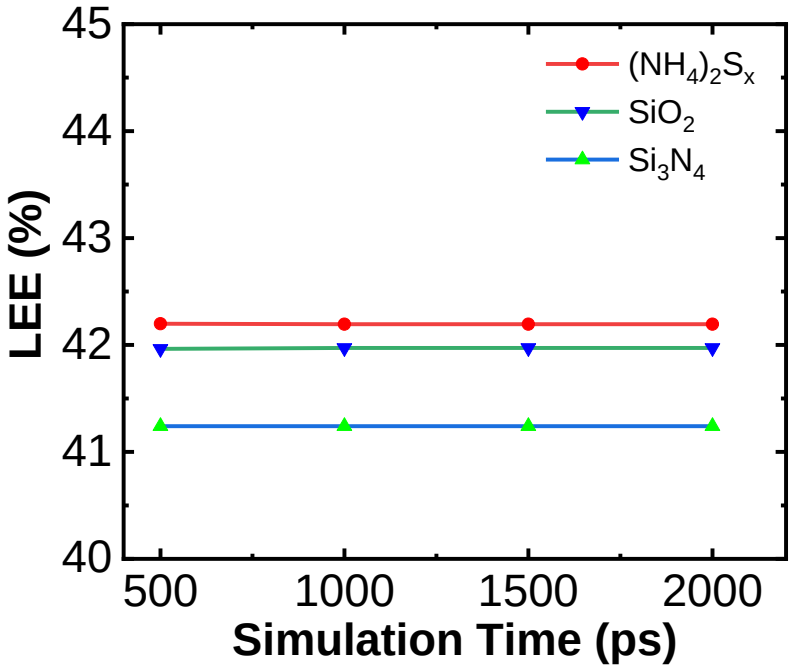

Figure 4.2 The illustration of LEE of nanowire LEDs after Si_3N_4, SiO_2, and $(NH_4)_2S_x$ passivation.

The dipole light source is considered a non-polarization. We just evaluated the passivation based on the achieved LEE. The LEE values were recorded from 41% to 42.2% for these surface passivation materials. As shown in Figure 4.2, the $(NH_4)_2S_x$ surface passivation offers the highest LEE of 42.2%. Therefore, $(NH_4)_2S_x$ was chosen for subsequent passivation experiments. By far, surface passivation with Si_3N_4, SiO_2 have experimentally demonstrated in several reports using common deposition techniques like atomic layer deposition (ALD), plasma enhanced chemical vapor deposition (PECVD),

sputtering, or E-beam evaporator. However, the passivation using $(NH_4)_2S_x$ is relatively limited. Also, although chemical surface treatment is highly beneficial, studies are largely limited in using only one chemical. To the best of our knowledge, an acid e.g. H_3PO_4 or a base e.g. KOH has an etching effect for the smooth surface [196], but AlGaN is subjected to reoxidation. Thus, Sulfide based chemicals was used to form a sulfur atomic layer on the surface, preventing the adsorption of oxygen [197]. In this work, the combination of KOH followed by $(NH_4)_2S_x$ surface passivation causes an enhancement in the electrical and optical properties of AlGaN nanowire UV LEDs. Compared to the as grown UV LEDs, passivated UV LEDs show a fascinating performance.

4.4.2 Experiment

KOH and $(NH_4)_2S_x$ surface passivation treatment has been found to be improved in the electrical and optical performance of AlGaN nanowire UV LEDs. Based on calculated intensity, enhancements in photoluminescence at 335 nm (49%), optical output power (65%), and electroluminescence (83%) recorded from fully passivated LED5 with respect to the as-grown nanowire LED1. These enhancements are attributed to the reduced nonradiative recombination on the nanowire surfaces. This study provides a potential surface passivation approach for producing high-power AlGaN nanowire LEDs operating in the UV spectrum.

4.4.3 AlGaN nanowire growth

The AlGaN UV LEDs nanowires were grown on Si (111) under nitrogen-rich conditions using a Veeco GEN II PAMBE system. Illustrated in Figure 4.3(a), the nanowire LED structure includes following segments: Si-doped *n*-type GaN (200 nm)/ *n*-$Al_{0.36}Ga_{0.64}N$

(150 nm)/ *i*-$Al_{0.17}Ga_{0.83}N$ (30 nm)/ *p*-$Al_{0.36}Ga_{0.64}N$ layer (50 nm)/ Mg-doped *p*-GaN (20 nm). During the AlGaN nanowire heterostructure growth process, the nitrogen flow rate was kept at 1 sccm and plasma power was set at 400 W. The GaN and AlGaN segments were grown at 780^{o}C and at 800-850^{o}C, respectively. The Al composition in the active region and cladding layers can be varied by Al/Ga flux ratio and controlling the substrate temperature. The growth rate of GaN and AlGaN layers are of ~3 and ~2 (nm/min), respectively.

Five AlGaN UVA LED samples denoted as LED1, LED2, LED3, LED4, and LED5 were developed and characterized. LED1 as the reference sample, is an as-grown AlGaN nanowire UVA LED. LED2 has a similar structure to LED1, but it was treated only with KOH (30% at 50 ^{o}C) for 30 min. LED3 and LED4 were passivated with KOH for 30 min, followed by $(NH_4)_2S_x$ (40-48% concentration at 50 ^{o}C) for 10 min and 20 min, respectively. LED5 was first treated in KOH for 30 min, followed by $(NH_4)_2S_x$ passivation for 30 min.

The photoluminescence characterization was performed on these five UVB LEDs, while the electroluminescence, optical power, and current-voltage characteristics were conducted on LED1, LED3, and LED5. Since LED2, LED3, and LED4 have similar passivation patterns, we chose LED3 to present for these three LEDs. The LED samples were then dried in N_2 and fabricated following our standard fabrication process. The nanowire LED samples were filled up with polyimide by spin coating. Then, polyimide was etched by RIE to expose the top of the nanowires for forming the *p*-type contact. The photolithography process was deployed to define the devices' size and electrode position. The detailed fabrication process could be found elsewhere [198].

Figure 4.3 illustrates the schematic structure of the AlGaN nanowire LEDs and SEM image of highly uniform nanowire LEDs depicting uniform nanowires across the Si wafer. The height of the nanowires is of ~450 nm, and their diameter is in the range of 100-120 nm.

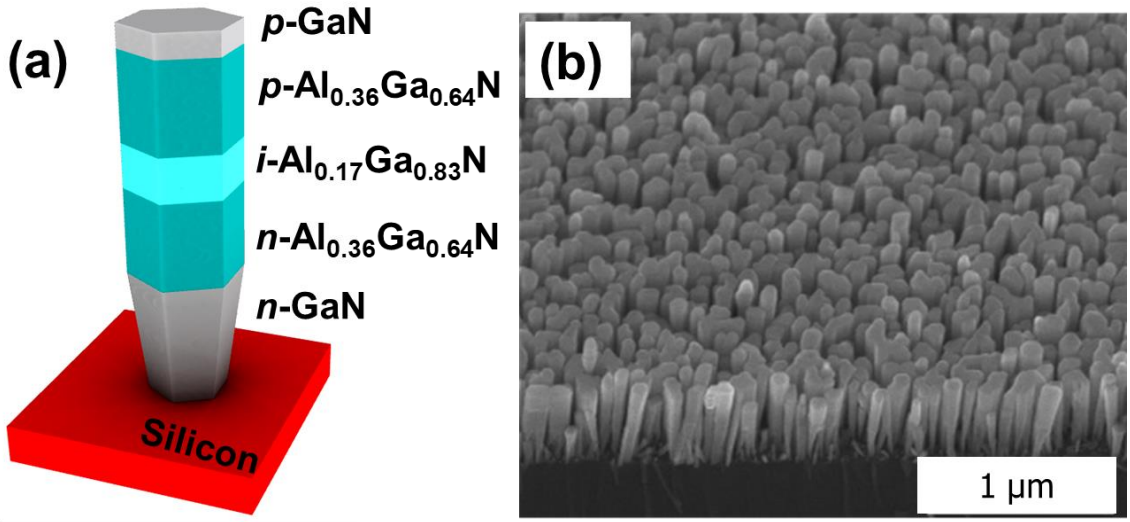

Figure 4.3 (a) The schematic structure of the AlGaN nanowire UVA LED on Si substrate; and (b) an SEM image of nanowires under 45^0 tilted with the height of nanowires around 450 nm.

4.4.4 Photoluminescence characteristics

Figure 4.4 shows the room temperature photoluminescence (PL) characterization of all five AlGaN nanowire-based UVA LEDs (with and without surface passivation). The measurements were carried out using a 266 nm laser source as the optical excitation. Three distinct peaks are clearly shown at 365 nm, 335 nm, and 295 nm. The peak emission at 365 nm originates from *n*- and *p*-GaN segments, while the main peak at 335 nm is the emission from the $Al_{0.17}Ga_{0.83}N$ active region. The shortest peak at 295 nm related to the emission from the *n*- and *p*-$Al_{0.36}Ga_{0.64}N$ cladding layers. The PL spectra also show a slight shoulder

at 312 nm, which stems from the defect associated radiative recombination normally observed in doped AlGaN [151, 198, 199].

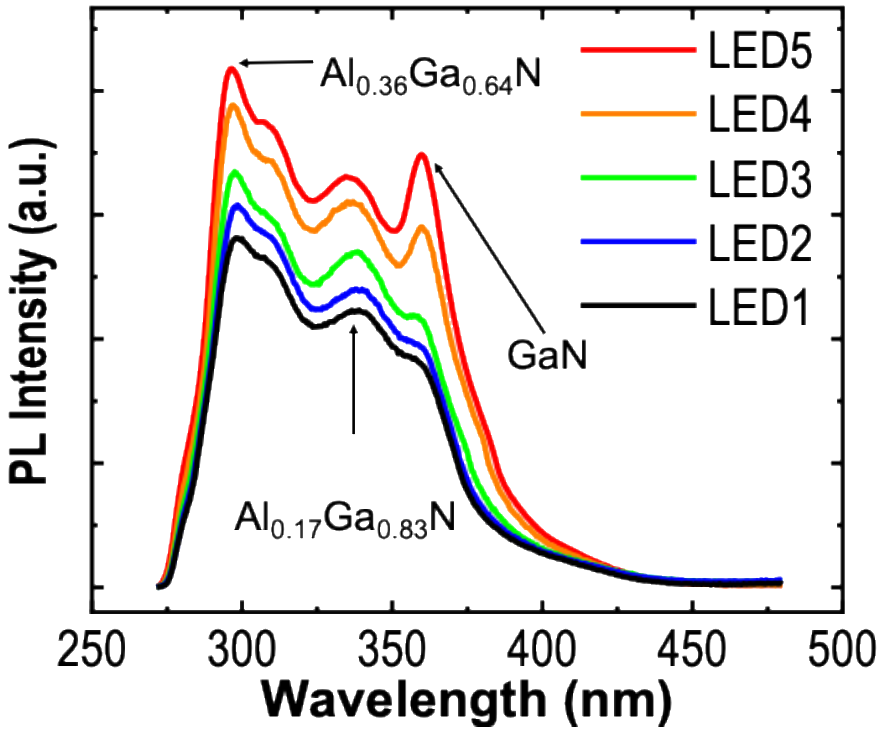

Figure 4.4 The PL spectra of as-grown nanowire UV LED1 and passivated nanowire UV LED2, LED3, LED4, and LED5.

We have found that KOH and $(NH_4)_2S_x$ surface treatments could improve the PL intensities of the nanowire UVA LEDs. LED5 yields the highest PL intensity, while as-grown UVA LED1 produces the lowest PL intensity. LED5 presents an increase in PL emission by 49%, compared to as-grown LED1. With a similar 30 min KOH treatment, a longer $(NH_4)_2S_x$ treatment makes the UVB LEDs stronger PL intensities. Particularly, LED2, LED3, and LED4 were treated with $(NH_4)_2S_x$ for 10, 20, and 30 min, respectively, the PL intensity of LED4 is higher than that of LED3 and the PL intensity of LED3 is higher than LED2's. The PL intensity enhancement is not significant for the LEDs treated

in $(NH_4)_2S_x$ for longer than 30 min. Therefore, LED5 was selected as the last set of the experiment for the presenting in this study.

The enhanced PL intensities are observed for all dominant peaks at 365 nm, 335 nm, and 295 nm, which are associated with *n*- and *p*-GaN segments, $Al_{0.17}Ga_{0.83}N$ active region, and $Al_{0.36}Ga_{0.64}N$ cladding layers. The PL intensity improvement is attributed to the suppression of the native oxides and defects on the surface of the nanowires. These reduced surface defects in turn suppress nonradiative recombination on the surface of the nanowires [184] thanks to the neutralized surface bonds [200, 201], the removal of the outermost oxides, and reduction of the surface nonradiative recombination velocity [200]. The results agree well with other studies reported for the enhanced PL intensities of AlGaN [194, 202] and InAs nanowires using KOH and $(NH_4)_2S_x$ passivation techniques [201]. A combination of KOH and $(NH_4)_2S_x$ treatment shows a significant improvement in PL intensity in UVA LEDs, compared to those only treated with KOH or $(NH_4)_2S_x$. The native oxide/defect on the nanowire surfaces could be significantly removed with KOH treatment [202]. However, after being treated in KOH, the nanowires are subjected to be oxidized again. $(NH_4)_2S_x$ treatment could form a sulfur atomic layer on the surface, preventing the adsorption of oxygen. Moreover, it is capable of deactivated dangling bonds on the nanowire surface. Therefore, the combination of KOH and $(NH_4)_2S_x$ is an efficient surface passivation approach to AlGaN nanowires.

4.4.5 Electroluminescence characteristics

Figure 4.5 shows the room temperature the EL spectra of UV LED1, LED3, and LED5 measured under 8 V forward bias condition. The EL spectra display a single emission peak at 335 nm. LED5 produces the strongest EL emission among these UVA LEDs. As grown

LED1 exhibits the lowest EL intensity; and LED3 shows a modest relative improvement in EL intensity compared to LED1. The EL enhancement of 83% recorded from LED5 compared with LED1 is attributed to the effective surface treatment with a combination of 30 min KOH and 30 min $(NH_4)_2S_x$. Obviously, from the characterization of these three UVA LEDs, the longer $(NH_4)_2S_x$ treatment results in a better EL emission by suppressing the impact of surface states on the radiative recombination in nanowire LEDs [200].

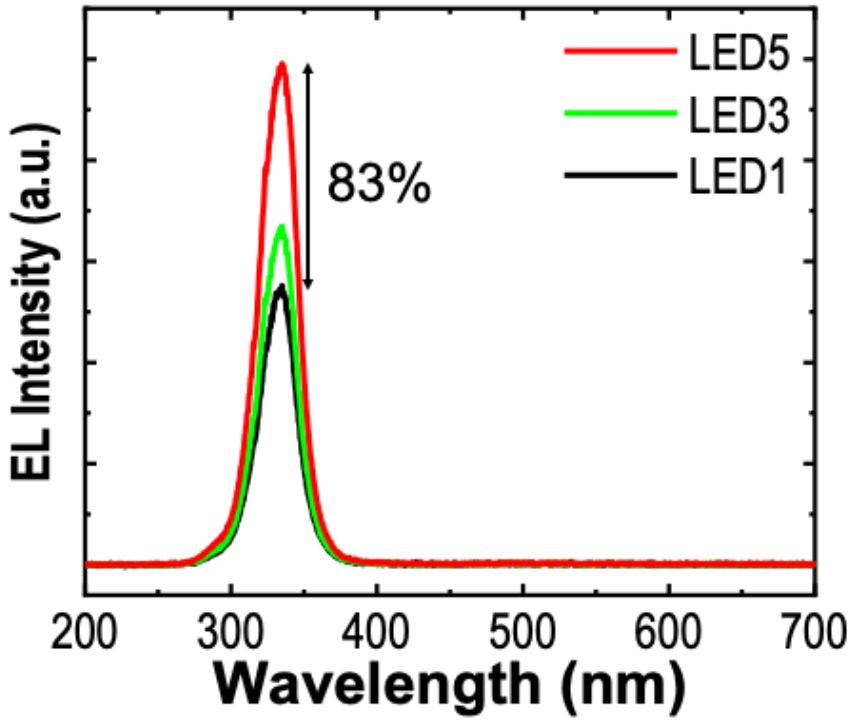

Figure 4.5 The EL spectra of UV LED1, UV LED3 with 30 min KOH and 10 min $(NH_4)_2S_x$ surface treatment, and UV LED5 with 30 min KOH and 30 min $(NH_4)_2S_x$ surface treatment.

4.4.6 Current-voltage and optical power characteristics

The I-V characteristics and optical power of LED1 and LED5 are presented in Figure 4.6. Illustrated in Figure 4.6a, LED5 shows an improved forward I-V characteristic and low series resistance, compared to LED1. The improved electrical properties are attributed to reduced *p*-GaN contact resistivity due to the removal of interfacial oxides, and surface

defects from *p*-GaN layer after KOH and $(NH_4)_2S_x$ treatment [22, 202]. Therefore, the wet chemical passivation of KOH combined with $(NH_4)_2S_x$ can increase the reliability and energy efficiency of AlGaN *n-i-p* nanowire UVA LEDs.

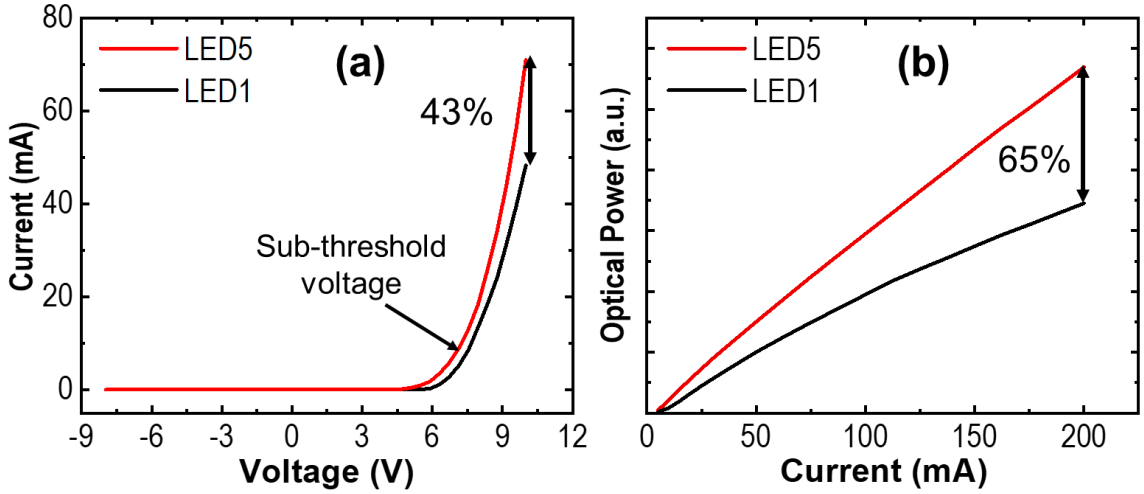

Figure 4.6 (a) The current-voltage characteristics; and (b) optical power of LED1 and LED5.

Figure 4.6b depicts the relative optical power of LED1 and LED5 as a function of the injection currents. The optical power of LED5 displays an increase by 65% compared to that of LED1. Figure 4.6b shows that the optical power of LED1 achieves slight increase upon the injected currents while that of LED5 presents a dramatic increase with the injection current increment, suggesting the high effectiveness of passivated AlGaN nanowire UV LEDs with KOH and $(NH_4)_2S_x$.

4.5 Conclusion

The simulation results from Si_3N_4, SiO_2, and $(NH_4)_2S_x$ surface passivation of AlGaN nanowire LEDs with the FDTD method indicate $(NH_4)_2S_x$ passivation is highly potential

with LEE up to nearly 42%. The simulation guides the experiment. We have demonstrated that wet chemical passivation using KOH and $(NH_4)_2S_x$ as a promising method to improve the performance of nanowire UVA LEDs grown by MBE. Our study shows that a sufficient surface passivation could increase the EL, the optical power, PL, and I-V characteristics of the AlGaN nanowire UVA LEDs at 335 nm by approximately 83%, 65%, 49%, and 43%, respectively. Such electrical and optical enhancements are attributed to the reduction of surface nonradiative recombination. A combination of KOH and $(NH_4)_2S_x$ treatment shows promising approach to high efficiency, high power AlGaN nanowire UV LEDs.

CHAPTER 5

NARROW BAND LEDS AND APPLICATIONS

5.1 Introduction

Artificial light sources with a narrow band emission are extremely important for many applications. Laser is well known as an ultra-narrow band light source. However, LEDs have been widely used since they exhibit significant advantages including safety, energy efficiency, flexibility, compact, chemical and physical stability, and long lifespan [95]. In addition, the emission wavelengths could be tuned from the ultraviolet to infrared regions. However, the spectrum of LEDs is relatively broad, limiting their practical applications. Currently, the EL spectra of III-nitride LEDs have a full width at half maximum (FWHM) or spectral linewidth, which is dependent on the injection current, of approximately 30-90 nm in visible LEDs [13, 28, 37] and around 10-30 nm in UV LEDs [161, 203, 204]. For reduced side effects of applications in life science, polymer curing, displays, and phototherapy, narrow band LEDs become desirable. For example, DNA and RNA molecules have an optical maximum absorption at 260 nm while proteins i.e., tyrosine and tryptophan have an intrinsic absorbance peak at 280 nm. Based on that knowledge, scientists have developed a method to evaluate the purity of DNA in the testing sample using polymerase chain reactions (PCR). Which is known as the A_{260}/A_{280} ratio, in which A is the absorbance [205].

In addition, narrow band LEDs generate light within a particular small bandwidth and highly potential in attempts to technical applications or visual acuity. Narrow band LEDs allow the applied science of color to be used for the development of high quality,

flexibility, optical-electronic platforms for narrow spectrum luminaires without using external bandpass filters. Narrow band LEDs, thus, would benefit specific demands in healthcare, scientific research, manufacturing industry, and disinfection, and other sophisticated lighting applications in art exhibition, cleanrooms, surgery rooms. For instance, 405 nm visible LEDs can continuously disinfect airborne and surface at the same time of lighting, leading to healthy environments for human beings [206].

Narrow band LEDs can be fabricated by adding a bandpass filter, quantum dots, nanostructures, photonic crystal gratings, or phosphors [207, 208] into LED structures. Among them, all-dielectric and metal dielectric multilayers are common types of bandpass structures [209]. All-dielectric structures work well for visible wavelengths while the latter is for the UV region. The operational principle of these bandpass filters is based on Fabry-Perot interferometer. The filters allow the desired passband to be transmitted by blocking wavelengths in both sides, wavelengths shorter and longer than the passband. The suppression bands are resulted by the destructive interference of multipath enhanced reflection into the transmitted side. The metal-dielectric multilayers also reduce unwanted wavelengths by the absorption. If the more metal layers are used, the transmission is reduced. Therefore, the number of the metal layers is limited up to a few layers for a reasonable transmissivity [210-212].

5.2 Importance of Narrow Band LEDs

The prevalence of narrow band LEDs is rapidly growing in the demand of numerous applications from lighting to life science and medicine. Narrow band LEDs allow sophisticated applications in terms of the spectral emissions.

In optogenetics, LEDs play an extremely important role in our life due to the low cost, long lifetime, highly flexibility, low electric power consumption, and huge applications. The spectral emission of III-nitride LEDs is easily tuned in a wide range of wavelengths from the ultraviolet to infrared. LEDs are predicted to become dominant light units for optogenetics. Optogenetics is the field in which light is used to control neurons on or off for the study of insight into the brain activity and neurological diseases' physiology. The activated or deactivated ion channels are controlled using the interaction of light with light-sensitive proteins, allowing deeper understanding of the biological and physiological functions or the working mechanism of the nerve cells. This method is also an extremely useful tool to study and treat brain-related diseases like Parkinson's and Autism. The triggering wavelength light sources used in optogenetics typically are within the visible region. The power of visible existing LEDs is high enough for most of the optogenetic applications.

The stimulation of the neurons is implemented by actuators, light-sensitive proteins. These proteins have been injected into the brain of a host. Widely used proteins include Channelrhodopsin-2, which is activated with a light stimulation to turn a neuron on, and Halorhodopsin used to silence a neuron. New types of proteins, sensitive to different wavelengths, have been continuously introduced [213]. Each of these proteins or opsins has a unique peak absorbance. For example, Channelrhodopsin-2 can pump the metal ions inward when activated under 450–470 nm blue light irradiation. Light-driven ion channel Halorhodopsin protein is used to silence neuronal activity. It is turned on with 632 nm red light illumination to pump chloride inward the cell's membrane [214]. Another sensitive protein, Archaerhodopsin allows protons to move outward if illuminated with 580

nm light [215, 216]. Therefore, narrow band LED based light sources would be an optimal lighting unit for studies in optogenetics. Especially, when implant LED devices are needed for wireless supplied energy [217, 218].

In photo curing, UV and visible LEDs have been used considerably in dental restoration [219] and hold great promise in industrial curing [220, 221]. In dental restoration, light-cured composites like Camphorquinone (2,3-bornanedione) are used widely [222]. They are exposed to visible light for photopolymerization. Common LED light curing units have become dominant since 2007 [223]. The LED curing efficiency is recorded higher than that from the conventional light sources [224]. Although high power blue LEDs have considerable advantages, the heating effect is still an issue. The heating problem could be reduced by using the narrow band LEDs for the avoidance of unwanted photons. Typically, the resin and initiators are based on the Camphorquinone material system, which has an absorbance peak at 468 nm. Therefore, narrow band LEDs with center wavelength 468 nm yield the most efficiency of curing. Narrow band LEDs have proven as a better light source compared to normal LEDs for curing effect [225]. Other photoinitiators being developed for dental restoration have a similar curing mechanism. They are optimally excited under a certain wavelength [226] to be broken out into free radicals, supporting the monomer polymerization.

In phototherapy, the advent of the laser light source 1960s, phototherapy became a medicine approach for many skin-related diseases. As stated in the section 1.2.3, phototherapy was already a well established method in healthcare. The list of diseases that can be cured with the phototherapy is continuously explored. Controlling the spectrum and intensity of the illumination is the key of the treatment. Today, LEDs are becoming a

critical light source for phototherapy in newborn jaundice, psoriasis, and vitiligo [69, 227]. Numerous studies indicate that wavelengths between 305 nm and 315 nm cause the most effective therapy for psoriasis and vitiligo [228-230], reducing acute and chronic risk. In jaundice treatment, bilirubin molecules absorb light highest at peak of 460 nm to change the molecular structure from *trans*- to *cis*-isomers [231]. As a result, narrow band LEDs around 460 nm with an abrupt attenuation at shorter and longer wavelengths can reduce side effects to the infants [232, 233]. Most of the existing phototherapy instruments for jaundice such as the Lullaby LED phototherapy system developed by GE Healthcare are based on LEDs. LED based phototherapy has also found impacts on oral mucositis where 880 nm [234] or 670 nm [235] irradiation are used for the treatment. Especially in wound healing, a wide range of wavelengths from the UV to red regions is needed during the treatment depending on stages of the wound healing. Such rapidly increased phototherapy, the narrow band LEDs would play an essential role in the future. In this work, narrow band LEDs were made on the purpose of wound healing phototherapy.

5.3 Methods to Obtain Optical Narrow Band LEDs

Narrow band LEDs can be produced by the integration of a bandpass filter into an LED structure. The emission from the normal LED will transmit through the integrated bandpass filter and the spectrum at the end is within a narrow band of wavelengths. The optical bandpass filter, as an enabling device, one of the most common optical components. It possesses a narrow transmission band of wavelengths by blocking the shorter and longer wavelength regions in both sides of the passband. The conventional bandpass filters are achieved by combining a short pass and long pass filter. The overlapping region of these

two passbands results in the passband of wavelength. However, in such a way, the passband is usually broad. Also, this method hardly achieves any desired passband because of the difficulty of finding materials for the right longwave pass and shortwave pass filters in the combination. These issues can be addressed with the interference bandpass filter.

Based on the interference phenomenon, the bandpass interference filter is very flexible in the design for nearly any narrow passband emission. In the visible wavelengths, the all-dielectric multilayers are commonly used while in the UV wavelengths, metal-dielectric multilayers are commonly used as UV bandpass filters.

5.3.1 All-dielectric multilayer bandpass filters

The structure of all-dielectric multilayers is one of the most common bandpass filters. It operates basically on the principle of the Fabry-Perot interferometer [209]. An all-dielectric filter structure consists of alternative high and low optical index dielectric transparent thin-film layers to take advantage of the interference. The simplest and the original Fabry-Perot filter includes two metal mirrors, which are separated by an air gap, called a cavity [210]. The all-dielectric single cavity bandpass filter, however, replaces the air gap with a transparent dielectric layer which is sandwiched by two parallel coating layers with a higher optical index. These parallel coating layers play the role of the mirrors whose reflection sides face each other. The incident light undergoes multiple reflections between the reflecting surfaces. The thickness of the cavity and the angle of incidence of the light beam define the interference of the reflected beams; construction or destruction. The reflected light rays experience constructive interference when the cavity optical thickness is equal to an integral of a half wavelength. In other words, the bandpass interference filter is designed to reduce the reflection of the expected passband wavelengths. Such all-

dielectric thin-film multilayers offer enormous design flexibility in designing visible and near-infrared bandpass filters.

The all-dielectric bandpass filters are usually a pair of high and low transparent dielectric. For example, the pairs of SiO_2/Si_3N_4, SiO_2/TiO_2, ZnS/Na_3AlF_6 are widely used for visible bandpass filters. The advantages of all-dielectric bandpass filter is that it can produce nearly any passband with an exceedingly narrow bandwidth.

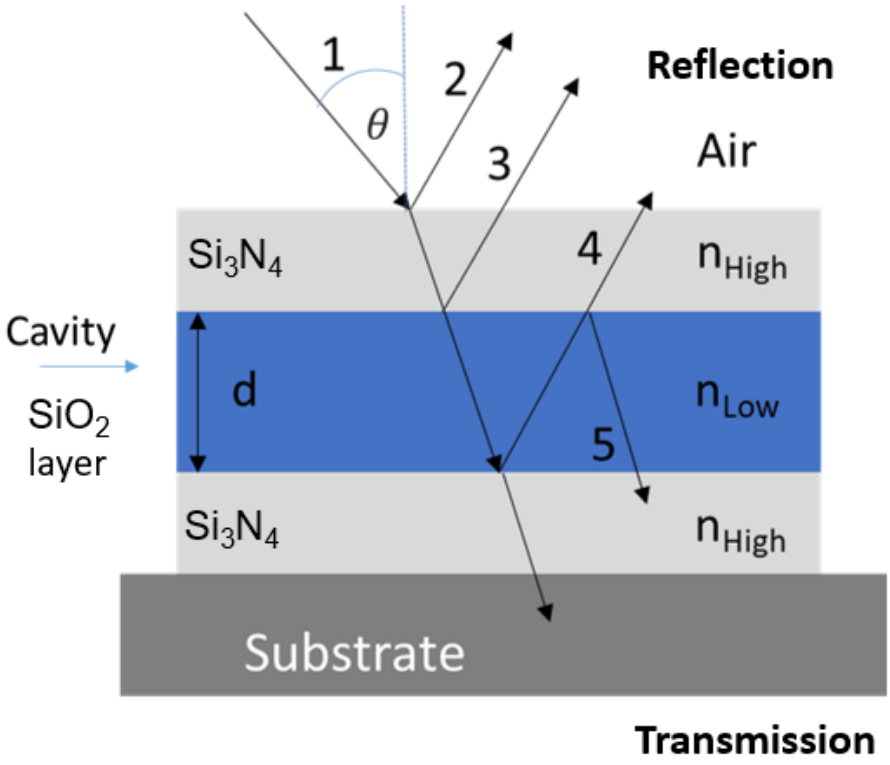

Figure 5.1 The structure of a single cavity metal-dielectric bandpass filter.

$$m\lambda = 2dcos\theta \tag{5.1}$$

In which d is the optical thickness, m = 0, 1, 2, and θ is the angle of incidence.

The all-dielectric single cavity filter usually obtains a relatively broad passband emission. To achieve a narrower passband, multiple cavity multilayers are used. The thickness of layers is changed to achieve an optical matching. Given that the interference depends on the wavelengths and difference of the light path. Thus, the passband characteristics of the filter depend on the wavelength and angle of incidence.

The structure of alternative dielectric multilayers could be deposited on a wide range of substrates such as silicon, sapphire, glass, and fused silica, using different coating techniques including PECVD, sputtering, E-beam evaporator, and so on. The bandpass filter structure could be applied for photodetectors, lasers, LEDs, solar cells, and cameras although there are some limitations related to the spectral shift by different angles of incidence and operating temperature needed to be taken into account.

5.3.2 Metal-dielectric multilayer bandpass filters

The all-dielectric bandpass filters work well for the visible and near-infrared bandpass filters, but the metal-dielectric multilayers are the favorable structure for the UV filters. Although all-dielectric bandpass filters were demonstrated for UV bandpass filters [236], the lack of low and high index pairs of the dielectrics in the UV wavelength makes it hard to develop UV bandpass filters for any desired wavelength. To achieve the out-of-band rejection, several all-dielectric structures need to be combined for overlapping stop bands. Occasionally, an absorptive metal layer is added to block unwanted wavelengths and the consequent transmission band is low. Also, the fabrication of all-dielectric with an additional metal coasting is complex. In many applications such as UV detectors, it is expected that if light is not transmitted, it should be absorbed rather than reflected.

For that reason, the structure of the metal-dielectric multilayer bandpass filter is dominantly used in the ultraviolet. The metal-dielectric filter presents an excellent capability of blocking the out-of-band wavelengths and allows for a desired passband transmission. The transmission spectrum is typically not a rectangular shape due to gradual cut-on and cut-off slopes. Also, the narrow band of the metal-dielectric bandpass filter could be obtained by increasing the thickness of the dielectric layers so that the construction of multiple beams could happen at higher interference modes [209]. However, if the dielectric layers are too thick, the roughness of the layer will increase in the deposition. The high rough surface will widen the spectrum of the filter while the high scattering increasing to corresponding larger thickness reduces the bandpass transmission [209].

In real filter devices, the number of layers of a metal-dielectric UV bandpass filter is chosen by considering the compensation of the transmissivity and narrow band width for particular applications. The thickness of the dielectric and metal layers are adjusted to tailor the performance of the bandpass filters across the UV region. For example, aluminum is highly reflective down to 200 nm so it can be combined with a dielectric such as Al_2O_3 and SiO_2 for development of UV bandpass filters operating in the whole UV region. Silver can also be used to develop the UV bandpass filter, not below 310 nm due to its highly absorbance at wavelengths below that region. The metal-dielectric filters were reported in solar-blind ultraviolet detectors, sensors. For example, two cavity Ag/SiO_2 multilayer has demonstrated 320 nm bandpass, which enables a suppression of visible and infrared wavelengths [237]. When the thickness of Ag metal layers is fixed and silica thickness is varied, the passband spectrum shifts into the longer wavelength. If the silica thickness is

fixed and Ag thickness is increased, the transmission is low and the passband becomes narrower. Such properties of Ag/SiO_2 agree with another report using Al/Al_2O_3 [212]. When the Al_2O_3 thickness is varied from 37, 48, and 56 nm, the passband shifts from 200 to 300 nm. In addition, the two-pair Al/Al_2O_3 filter results in a higher transmission but broader spectral linewidth, compared to that recorded from the three-pair filter.

Both all-dielectric and metal-dielectric multilayer coatings can be fabricated by deposition techniques, namely E-beam evaporator, ALD, MOCVD, PECVD, sputtering, physical vapor deposition (PVD), etc.

5.4 AlGaN/AlN Nanowire Far-UVC Narrow Band LEDs for Disinfection

Narrow band far-ultraviolet C (200-230 nm) LEDs (far-UVC LEDs) are strongly detrimental to airborne and surface pathogens while minimally invasive to human health. They can be used as a disinfectant to suppress the outbreak of infectious diseases with minimum safety concerns. Herein, we investigate a design of the AlGaN/AlN nanowire structure in combination with a bandpass filter for a narrow band far-UVC LED at 222 nm center wavelength. The LED achieves an ultra-narrow FWHM of ~12 nm after introducing a metal-dielectric Fabry-Perot optical bandpass interference filter with three periods of $Al/MgF_2/Al$ layers. The electrical and optical properties of the nanowire LEDs show the high performances with an IQE up to 80% and the maximum power exceeding 10 mW at 60 mA current injection. This narrow band far-UVC LED is a promising candidate for airborne and surface disinfection in occupied spaces to prevent the spread of contagious diseases such as COVID pandemic.

III-nitride compounds have gained momentum in the research and development of LEDs. Far-UVC LEDs, however, suffer from challenges of inefficient Mg-doped *p*-type activation, high spontaneous polarization, and piezoelectric polarization induced by lattice mismatch between AlN and GaN. Due to a high density of threading dislocations (over $10^8/cm^2$) resulted by a very high Al amount in AlGaN, far-UVC LED epitaxial layers are very limited in the quantum efficiency.

Nanowire structures with several advantages have emerged as a promising candidate for highly efficient far-UVC LEDs. First, unlike thin-film counterpart, since the induced strain energy of nanowires can release effectively into its sidewall, grown nanowires can attain a low level of threading dislocations and total polarization [38, 238], thereby minimizing defects and QCSE [239], compared to the thin-film UV LEDs. Second**,** due to the high surface area-to-volume ratio, the diffusion of atomic Mg acceptors at the nanowire's surface could easily happen, beneficial for a highly doping concentration in AlGaN/AlN nanowires [30]. Third, nanowire structure LEDs outperforms their thin-film counterpart LEDs in terms of the LEE [173]. Finally, high quality crystalline nanowires could be realized on a wide variety of substrates including cost-beneficial Si wafers [179].

Airborne and surface disinfection are promising applications from far-UVC LEDs among their various applications in water/air purification, UV curing, phototherapy, biology, and neuroscience [1, 7, 142]. In airborne and surface disinfection in occupied spaces, far-UVC LEDs at 222 nm is preferable because 222 nm photons are almost absorbed by the human's dead skin cell layer, thereby being surely harmless to humans [240]. In this section, nanowire far-UVC LEDs at 222 nm are investigated with an advanced numerical device simulation method to the nanowire LED structure, simple

enough for an easily epitaxial MBE growth in the empirical research. Advanced Physical Models of Semiconductor Devices (APSYS) software is used to study the performance of the UV nanowire LED in this study. The far-UVC LED structure consists of a single quantum well in the $Al_{0.855}Ga_{0.145}N$ active region. APSYS is a commercial computational simulator which has been widely used in LED design and validation. Its solvers utilize the self-consistent solutions of many quantum mechanics equations including Schrodinger, Poisson, carrier transport, current continuity, quantum mechanical wave, and photon rate equations with suitable boundary conditions. Simulation results yield necessary parameters for the evaluation of the LED through its energy band diagram, IQE, current-voltage characteristic, output power, etc.

In terms of airborne surface disinfection, a far-UVC narrow spectrum is highly desirable because it can avoid harmful impacts on humans [241] when these wavelengths do not penetrate deep into the living cells in the dermis and epidermis layers [242-244]. Generally, UVC LEDs usually possess a FWHM of >25 nm. Therefore, to produce a narrow spectrum, an integrated bandpass interference filter is necessary to achieve narrow band far-UVC LEDs. A filter is designed from a Fabry-Perot structure having the stack of Al/MgF_2 layers. A starting structure includes three periods of $Al/MgF_2/Al$ layers. OpenFilters, an open-source software, is used to optimize the bandpass filter by adjusting the thickness of each layer. The maximum transmission is achieved over 50% with a FWHM of ~12 nm. With two simulation tools, APSYS and OpenFilters, a simple effective AlGaN/AlN nanowire structure has been demonstrated for high performance 222 nm narrow band far-UVC LEDs for surface disinfection applications.

5.4.1 Device structure and simulation parameters

Because the growth of a high crystalline quality of Al-rich AlGaN LEDs with multi-quantum wells is challenging, so a simple *n-i-p* LED structure was designed for the far-UVC LED. This single quantum well nanowire LED is expected to be grown with a high crystalline quality.

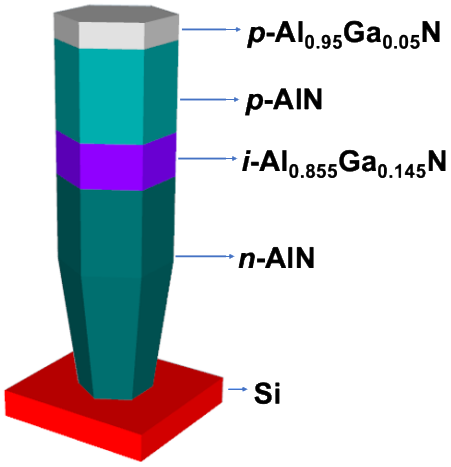

Figure 5.2 The schematic structure of the AlGaN/AlN nanowire far-UVC LEDs.

For the simulation study, the advanced numerical device simulation with APSYS software is applied to investigate the performance of the *n-i-p* AlGaN/AlN nanowire UV LED at 222 nm. The LED nanowire schematic consists of *300 nm n-AlN/ 40 nm i-AlGaN/ 100 nm p-AlN/ 20 nm p*-$Al_{0.95}Ga_{0.05}N$, which is considered to be grown on a (111) silicon wafer, as shown in Figure 5.2. The *n*-AlN layer is the Si-doped ($n_D = 2x10^{18}$ cm^{-3}). The Si energy activation is set at 15 meV [245]. The active region is an intrinsic $Al_{0.855}Ga_{0.145}N$ of 40 nm. The *p*- region is a Mg doped *p*-AlN ($N_A = 2x10^{18}$ cm^{-3}) with the thickness of 100 nm. Finally, a thin *p*-$Al_{0.95}Ga_{0.05}N$ ($N_A = 10^{20}$ cm^{-3}) is employed on the top of the nanowire to form an ohmic contact. The Mg activation energy for *p*-AlN and *p*-$Al_{0.95}Ga_{0.05}N$ is set

at 630 meV and 608.5 meV, respectively [245]. To obtain 222 nm emission, 85.5% of AlN composition in $Al_xGa_{1-x}N$ is calculated from the formula: Where b = 1 is chosen [246].

$$E_{AlGaN} = xE_{AlN} + (1-x)E_{GaN} - bx(1-x) \quad (5.2)$$

The radiative recombination coefficient is set at 2.13×10^{-11} cm^3/s, Auger recombination coefficient 2.88×10^{-30} cm^6/s and the Shockley-Read-Hall (SRH) recombination lifetime 15 ns. The interface charge densities are considered to be 50%. The LED chip size is 300 μm^2.

5.4.2 Results and discussions

The energy band diagram and IQE of an AlGaN/AlN nanowire UV LED are essential characteristics for providing an insight into inherent nanowire properties.

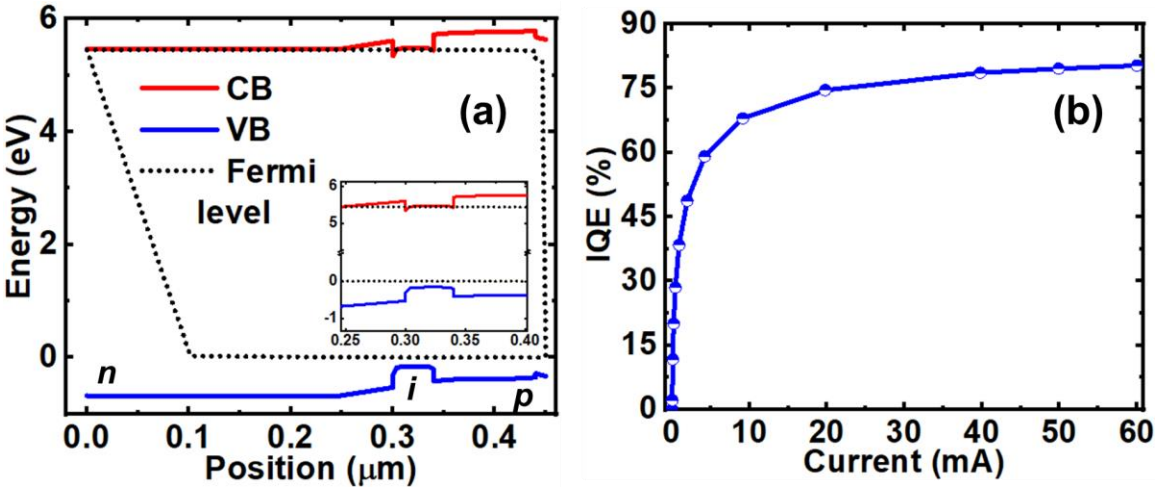

Figure 5.3 (a) Energy band diagram; and (b) IQE of the AlGaN nanowire far-UVC LED.

Figure 5.3a shows the calculated band-energy diagram of the *n*-*i*-*p* AlGaN/AlN nanowire far-UVC LED at 60 mA injection current. The inset shows that at the *n*-AlN/*i*-

AlGaN interface, closely toward the *n*-side, the conduction band is bended down while the valence band is curved up. Due to the single quantum well and nanowire structure, the strain induced piezoelectric polarization is small, and only the spontaneous polarization mainly affects the performance of the device. In order words, the hole and electron carriers are accumulated in the same side of the quantum well, so their wave functions are likely overlapped, leading to a high radiative recombination rate. Therefore, the IQE is as high as ~80% at 60 mA injection current, as shown in Figure 5.3b. The IQE increases from 65% at 10 mA to reach a maximum value of 80% at 60 mA without efficiency droop.

5.4.3 Current-voltage characteristic and output power

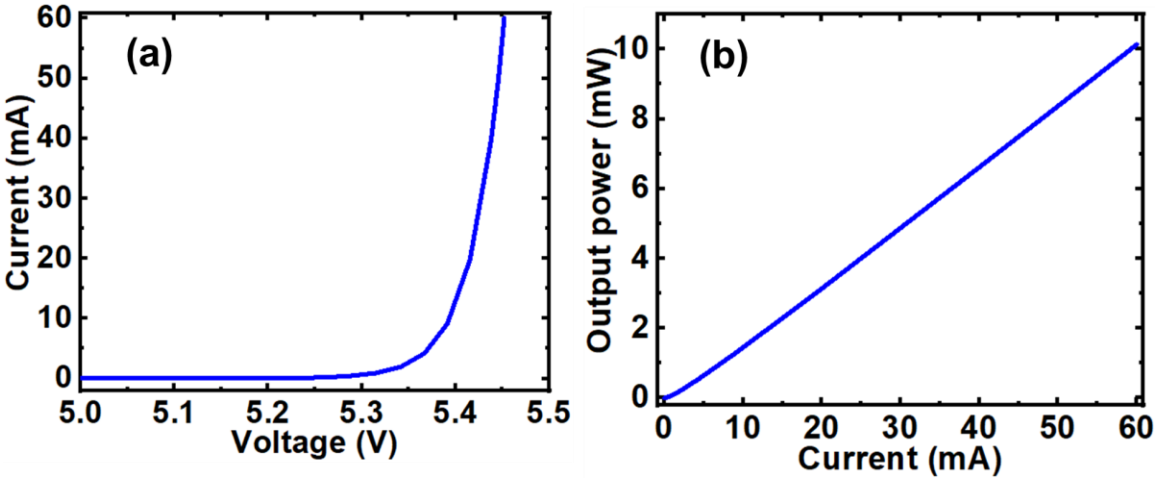

Figure 5.4 (a) Current-voltage characteristic; and (b) output power of the AlGaN/AlN nanowire far-UVC LED.

The current-voltage (I-V) characteristic and the output power are quantitatively determined and presented in Figure 5.4. An exponential increase in the injection currents as a function of the forward voltage is shown in the curve of Figure 5.4a. When the applied voltage is smaller than 5.3 V, the injected current is almost no change. However, a small

increase by ~ 0.1 V to 5.45 V in the operation voltage leads to an exponential rise in the injection current, from below 5 mA to more than 60 mA, indicating a relatively small resistivity value of the far-UVC LED [6]. For example, the bias voltage at 5.35 V (V_T), defined as the threshold voltage, produces a current of 5 mA, and at 5.45 V, the current of 60 mA are recorded, respectively. Figure 5. 4b shows a linear dependence of the output power on the injection current. The output power increases from 1.75 mW to 10 mW with increasing current from 10 mA to 60 mA.

An optical bandpass filter is a structure that eliminates most wavelengths, except a narrow interval with a very high transmission. The narrow spectral LED is ideal for airborne and surface disinfection applications since the precise stimulation could be achieved when targeted molecules or pathogens merely interact with photons at particular energy levels. The LEDs integrated with a bandpass filter would create narrow band LEDs. The bandpass filter is usually developed from a number of metal/dielectric/metal layers. It is based on the typical metal-dielectric Fabry-Perot interferometer. Shown in Figure 5.5a is the design of a bandpass interference filter, consisting of three Al/MgF_2/Al periods after the optimization by OpenFilters software [247]. Al and MgF_2 are common materials for UV bandpass filters. MgF_2 transparent in a wide range from 210 nm to 10 μm [209] is used as the spacer, and aluminum plays a role as mirrors. Al metal is superior reflective in the far-UVC wavelength, compared to other common reflective metals [248]. The designed bandpass filter includes three MgF_2 layers sandwiched by four parallel Al layers. The thickness of the filter is of ~265 nm, shown in Figure 5.5a. This bandpass filter is easily fabricated and it results in a relatively high transmission, up to 50% at 222 nm with a FWHM of ~12 nm, presented in Figure 5.5b. The numerically realized bandpass filter

shows promising for narrow far-UVC LEDs. The far-UVC LEDs pave the way for effectively disinfecting airborne and surface pathogen organisms without harmful effects i.e. phototoxicity in occupied spaces. For example, 222 nm UV LEDs having the FWHM of 12 nm, the emissive spectrum is from 209.5 nm to 234.5 nm. Photons in that range of wavelengths are highly absorbed by the layer of dead skin cells, so they will be harmless to living skin cells. Compared to the longer wavelengths such as 254 nm, 222 nm far-UVC LEDs are safer in disinfection since 245 nm UV LED is able to penetrate deep into the dermis, causing detrimental health problems [249].

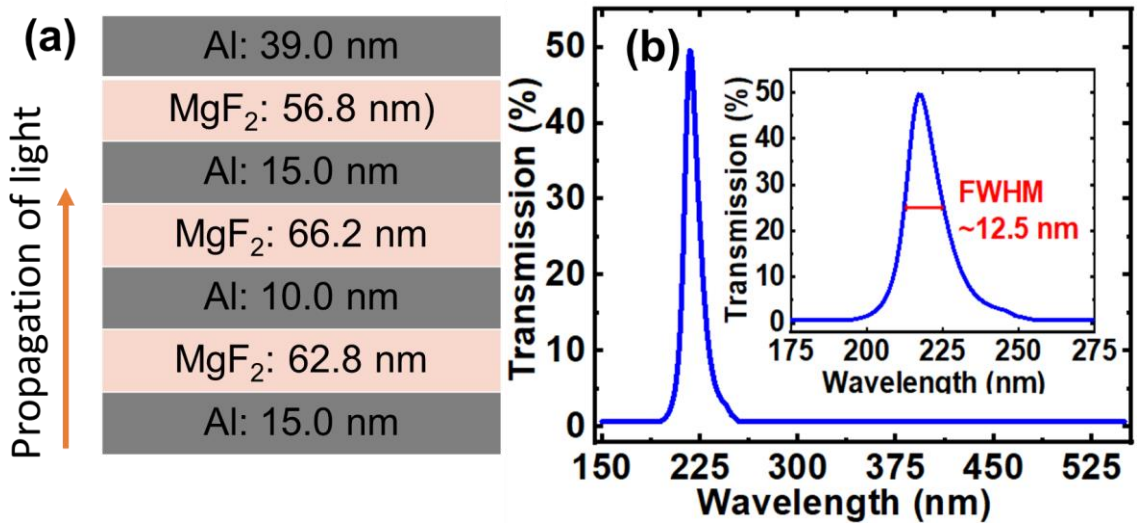

Figure 5.5 (a) The bandpass filter of three periods of Al/MgF_2/Al layers; and (b) the obtained narrow spectrum from the filter at 222 nm.

We have designed a simple *n-i-p* AlGaN nanowire far-UVC LED, with a single quantum well for the emission at 222 nm, targeting for airborne and surface disinfection. The IQE of 80%, corresponding output power of 10 mW, and an excellent I-V characteristic suggest a remarkable design for AlGaN/AlN nanowire far-UVC LEDs. Such far-UVC LED chips are also able to be integrated with a bandpass UV filter for a narrow-

spectral emission. The FWHM of the obtained narrow band far-UVC LED is as small as ~12 nm, superior to its current broadband counterparts for the airborne and surface disinfection. To that end, the integration of an on-chip optical bandpass filter with the LED structures is proposed. The emission of that LED would be very narrow, suitable for precision applications including phototherapy.

An on-chip optical filter is manipulated dedicatedly to make narrow band LEDs. The integration of optical filters with a normal LED chip allows a narrow spectrum for exactly practical precision treatment. The ultra-narrow band spectra of ultraviolet, visible, and infrared LEDs can be achieved by means of deposition of Al/Al_2O_3 and Si_3N_4/SiO_2 thin-film multilayers, respectively. With this technique, narrow UV and visible region can be sorted out. Before the fabrication of the optical filters, computer-assisted simulations from OpenFilters software have been done.

5.5 Narrow Band LEDs for Chronic Wound Healing Phototherapy

The chronic wound causes a significant burden to patients, physicians, healthcare systems, and societies, affect tens of millions of people, and cost billions annually [250, 251]. Several existing methods for wound care are almost drugs and wound dressings in combination with other advanced techniques such as negative pressure, electric stimulation, ultrasound, etc [252]. Phototherapy as an alternative method becomes a promising tool for wound treatment when LEDs become highly flexible in terms of the spectrum, power, and design. A smart light system based on LEDs was funded by European Commission in 2015 for the wound healing purpose [253]. The findings show that 620-750 nm red spectrum triggers layers of the skin for the growth of keratinocytes and fibroblasts

while the blue 450-495 nm wavelengths enable dominantly antibacterial effects of the skin surface [254].

Wound healing is a complex but physiologically coordinated process. The wound healing typically experiences three stages: inflammation, proliferation, and remodeling. Each stage is associated with considerable behaviors and functions from cells, proteins, macromolecules, and signal molecules. If a wound is prevented from healing due to some risk factors, it will become the delayed healing wound or chronic wound. Some possible risk factors are antibiotic resistant infection, diabetes, obesity, malnutrition, bedsores, and weakened immune system [255, 256]. As a result, chronic wounds are, but not limited to, those infected with antibiotic-resistant bacteria, and associated with diabetes, venous insufficiency, bedsores, poor circulation, and weakened immune system [257]. Currently, antibiotic-resistant chronic wounds have received much attention due to the challenges and threats to the public health and economy [251, 256].

Recently, LEDs have been extensively studied as an alternative treatment for wound healing without side effects compared to antibiotics [258]. To implement a phototherapy treatment for wound healing, it requires an illuminating light source, which covers a wide range of wavelengths from the ultraviolet to infrared during the treatment. Also, the LED light sources could finely emit photons in very different narrow band wavelengths for specifically induced healing functions in each healing stage. If external bandpass optical filters are applied to create the narrow wavelength illuminations from normal LEDs, the phototherapy' light source is highly probably bulky and expensive. Such challenges limit the efficiency of the phototherapy devices and prevent them from

ubiquitous applications in hospitals and at home. Therefore, demand for narrow band LEDs light sources is very critical for wound healing treatment with phototherapy.

For that reason and to the best of my knowledge, the combination of visible and ultraviolet narrow band LEDs would be the first-ever demonstrated for wound healing. The narrow band LEDs could also be used in other phototherapy light units. These units enable selectively stimulating multi-biological effects in different wound healing processes. In detail, antibiotic-resistant bacteria in chronic wounds such as Methicillin-resistant Staphylococcus aureus (MRSA) can be eliminated by UV illuminations. Three main stages of inflammation, cell proliferation, and remodeling in wound healing processes could be facilitated with visible and UV illuminations later. Because currently available phototherapy devices, which are limited in a few wavelength irradiations, are not designed for wound healing treatment, the narrow band LEDs based on III-nitride nanowires will be the best option for chronic wouns phototherapy.

5.5.1 Impacts of visible and near-infrared light to wound healing

Besides UV light, photons in 400-760 nm visible and near-infrared (760-1000 nm) wavelengths show therapeutic effects on wound healing which were proven in studies based on model, animals, and preliminary clinical trials [259-261]. In this section, healing effects of three primitive colors: red, green, and blue, are studied. Normally, a low irradiation can stimulate cell proliferation, wound closure, and scarless healing. Surprisingly, a short time intense exposure of the visible light into bacterial-antibiotic resistant infected wounds has resulted in a significant reduction of a bacteria colony [260].

a) Red and infrared phototherapy: In 2002, NASA conducted a pilot research into the space. Illuminations with red and near-infrared wavelengths (650-1000 nm) were found very important in helping healing wounds. [262]. As the long wavelengths, red and near-infrared photons, in one hand, can penetrate deep into the dermis layer [263] and trigger molecules and proteins in the low dermis layer; on the other hand, they are carcinogenic free and do not cause mutagenic effects. Red light is known as a metabolism promoter. It induces cells to produce more energy with production of more adenosine triphosphate (ATP) by bringing about biochemical effects related to mitochondria [264]. The more energy the cells acquire, the better a wound can be healed. The red-light irradiation also produces the cell proliferation no matter what a wound has been treated with and without steroids [265]. A study on incisional and burn wounds of mice has shown that 760 nm LED irradiation can accelerate the healing process. Compared with the reference wounds which lacked a phototherapy treatment, the wounds treated with the red light enhance epithelial migration, suggesting red light illumination for post-operative wound repair [266]. In vitro study, an irradiation at 636 nm makes diabetic wounded cells hastened wound closure, increased cell proliferation, and normalized cellular function.

b) Green light: Green LED phototherapy has been found to offer beneficial mechanisms for wound healing [267]. Migratory and proliferative mediators, known as signals for the healing process, have been significantly expressed in excision wounds from mice a few days after irradiations with green LEDs. *In-vitro* studies show that green light could stimulate human fibroblasts to highly secrete mRNA, cytokine proteins, and HaCat keratinocytes. Min-Woo Cheon et al. implemented 525 nm green LEDs on wounds of male Sprague Dawley rats. The findings present clear evidence of the cell proliferation and

reepithelization enhanced in the wound bed, and at the same time, the neighboring environment is found to have an increase in the cell proliferation [268]. It was found that genes related to wound healing, i.e. presents G protein-coupled receptors (GPR) class are upregulated after 520 nm (green) irradiation. The GPR class is known as the highly related factor to wound healing process [269]. This is the biological beneficial effects of green LEDs illumination. Green light also induces stem cells by the activation of signaling the pathway stem cell [270]. In the remodeling stage, green light has potential for sealing wounds with less scars by the formation of crosslinking within tissues and between tissues with the surface.

c) Blue wavelength: Blue light (450 -500 nm) is widely used to treat neonatal jaundice, a yellow skin disease in newborns, due to the capability of blue light irradiation in reducing the level of bilirubin in the blood [271]. In wound healing, like red and green, blue light has received considerable attention. Several studies have confirmed blue light is of antimicrobial effects. Many supporting factors such as anti-inflammatory and keratin expression associated with wound healing promotion were found after blue light treatment [272, 273]. Several antibiotic-resistant bacterial strains including MRSA can be killed under 460-470 nm blue LED irradiation [76, 274-276]. Furthermore, blue LED illumination can shorten wound healing process by stimulating a higher keratin expression and enhanced epithelialization [277, 278]. The LED irradiations at 420 nm have been found to facilitate the keratin expression, increased metabolism, and fibroblast proliferation [279]. Such biological behaviors are related to wound healing effects. The expression of keratin was also found with 470 nm blue treatment [277]. After six days of treatment, full-thickness wounds have shown an improvement in healing [280], indicating the healing

biological effects from blue LEDs. Blue LED irradiations on different types of mice have been studied by Giada Magni et al. [281]. The immediate hemostasis and an acceleration of wound healing was presented. The blue light irradiation enables immediate hemostasis by evidence of rapidly observed coagulation with non-linear microscopic imaging [281]. These findings suggest that UV and visible LED phototherapy provides a safe and cost-effective approach for wound healing treatment.

5.5.2 Impacts of ultraviolet light to wound healing

Ultraviolet light is well known for its infection due to the ionization effects [282-286]. In medical significance UV light is divided into three regions: UVC (200-280 nm), UVB (280–320 nm) and UVA (320-400 nm). Although prolonged UV exposure can damage the skin, a short-term UV irradiation in a controlled dose results in positive effects in chronic wound healing wound sites [75, 77, 287].

Chronic wounds infected with antibiotic resistant bacteria can be treated with UV therapy. For example, S. aureus and E. faecalis superbugs in wound sites can be killed or deactivated by 254 nm UV irradiation in a matter of seconds [288]. The sterile effect of UV light is mainly from UVC, but the UVB and UVA illumination has also contributed to killing bacteria in wounds [289]. Bacteria are killed or inactivated by direct or indirect mechanisms. The direct damage of UV light to the bacteria's nucleic acids or DNA [290] or the intermediate agents including radicals and reactive oxygen species (ROS). The bactericidal effect of the UV irradiation is also verified via a study of the intravenous infusion. In addition to the germicide, other biological effects by UV light irradiation have been reported. An enhancement of cell signals has been seen by UVA irradiation. The boosted immune system and increased vascular endothelial factor receptor-2 signaling

have been seen from UVB illumination [291]. UV radiations could facilitate angiogenesis [292]. An increase in leukocytes infiltration, VEGF expression, and erythema reduction is recorded as well [293].

It turns out that UV exposure can lead to various biological consequences, correspondingly photons at different wavelengths, critical for wound healing. It is attributed to the different depth levels of penetration into the skin layers. As a result, UV narrow band LEDs are possible for phototherapy lighting units for wound treatment regardless of side effects.

a) UVA: UVA (320-400 nm) has the longest wavelength in the UV region, and it can penetrate deeper into the skin, compared to UVB and UVC. UVA at 341 nm can penetrates 60 μm into the dermis layer while 314 nm UVB penetrate only 19.4 μm, and 290 nm UVB goes to the depth at 10.9 μm at the layers of the epidermis [294]. The wound healing facilitation by UVA modality comes from a precise UVA irradiation in order to induce a variety of biological effects in support of the wound healing process. Vascular endothelial growth factors (VEGF) as angiogenic factors in the proliferative stage are significantly increased after the UVA treatment [294]. Stroma cells in the dermis can be controlled via UVA irradiation with the evidence of growth factors for keratinocyte proliferation and fibroblasts [295]. UVA is also able to stimulate erythema [296], one of the first inflammatory responses in the wound healing process. UVA-induced signaling factors implicate the helpful UVA irradiation in the cell proliferation [296, 297]. UVA irradiation is able to activate mast cells (MC), hypergranulation, and induce histamine release *ex-vivo* [298]. Such wound healing effects induced by UVA irradiation clearly indicate the healing effects.

b) UVB: UVB (280-320 nm) can penetrate to the lowest level of the epidermis and can help a wound heal efficiently. It is widely known that UVB illumination support vitamin D synthesis. Vitamin D deficiency is one of the reasons delaying healing chronic wound illnesses [298-300]. UVB LEDs have been found in support of the synthesis of Vitamin D in human skin more efficiently than the sunlight [137]. Moreover, UVB irradiation also increases in neutrophils moving into a lesion. Neutrophils function as phagocytes that eat, digest, and destroy pathogen microorganisms. An increase in the filtration of leukocytes and reduction in erythema are also observed after UVB irradiation [293]. A moderate dose UVB illumination is able to express T-Cells, surface markers, and cytokines [301]. It means UVB exposure could be used for immune upregulation and inflammation. In addition, a moderate dose of UVB irradiation can cause a considerable increase in VEGFRs and human keratinocytes in the epidermis [302]. The high presence of secreted VEGFs consisting of the deposition of collagen, angiogenesis, and epithelization has been reported after UVB illumination [303, 304]. Another study shows that acute UVB irradiation is likely to create a supporting environment for the formation of capillary (small blood vessels). Such a proangiogenic environment comes from the downregulation of thrombospondin-1 [304], supporting angiogenesis growth. The role of UVB in wound healing is also supported as the epithelialization in slow-healing wounds [305], and angiogenesis [292] are enhanced after the exposure. Antimicrobial effects of UVB were also reported in several papers [306-308]. Based on the reported benefits, UVB LED irradiation is clearly to benefit wound healing treatment.

c) UVC: UVC (200–280 nm) light is an ionized radiation so that UVC illumination is likely to directly damage DNA and RNA molecules. It also can produce free radicals and ROS

throught intermediate events. The germicidal properties of UVC were well reported [156, 290]. A single UVC exposure enables a reduction over 90% of fungal burden and bacteria culture on a burn wound [309]. UVC illumination is found to reduce the bacterial colony in antibiotic-resistant infected wounds [75, 287]. Many antibiotic resistant bacterial strains such as MRSA, vancomycin-resistant enterococcus (VRE), and Pseudomonas can be killed or inhibited by UVC exposure. One report presented that aspergillus, pseudomonas aeruginosa, and mycobacterium abscessus are inhibited after 3-15s UVC irradiation. Importantly, keratinocytes and other cells are seldomly damaged by such a short period of exposure like that [244, 310]. Immediately germicidal effects of UVC irradiation are superior to common antibiotics [290]. Consequently, UVC narrow band LEDs could be used for phototherapy for chronic wounds caused by bacterial infections.

5.5.3 Design and fabrication of visible bandpass filters

To have narrow band LEDs, the idea is to add a bandpass filter which has maximum transmission within the central wavelength of the LEDs. Historically, the design of an optical bandpass filter is sophisticated and implemented using graphical methods. Today, however, this becomes easier with computer-assisted calculation methods using software. The design of optical filters using computers was first demonstrated by Baumeister 60 years ago [311]. Since then, many methods have been explored to realize optical filters for any special applications. In this work, OpenFilters software is used. It is an open-source license, released by Stéphane Larouche and Ludvik Martinu under GNU General Public License software [247]. The software utilizes the step and transfer matrix method to optimize the structure of filters. The designed bandpass filters are based on Fabry-Perot

multiplayer interferometer. The all-dielectric and metal-dielectric multilayers are used for visible and ultraviolet LEDs, respectively.

Initially, the bandpass visible filters have been designed with pairs of Si_3N_4/SiO_2 multilayers. These materials are transparent in visible wavelengths and the difference of their optical index is favorable for the reflection.

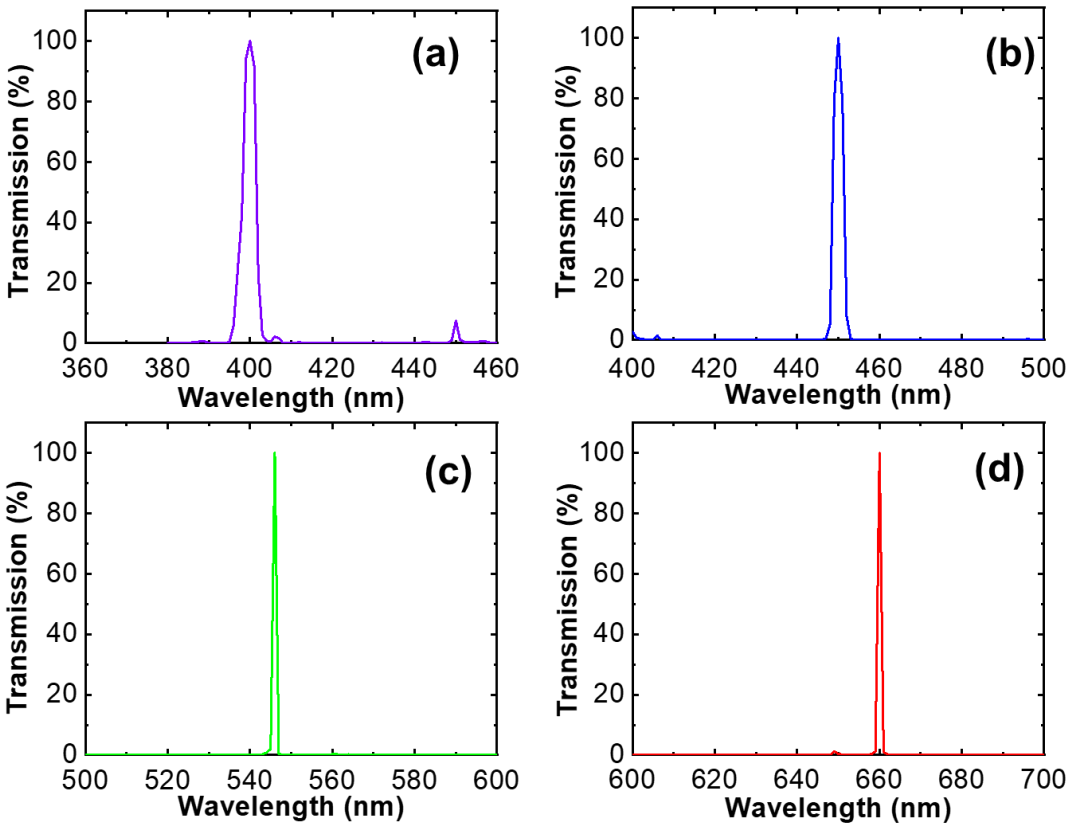

Figure 5.6 The bandpass filters at 400 nm violet, 450 nm blue, 545 nm green, and 660 nm red transmission designed with OpenFilters.

The structure of initial bandpass filters includes 96 alternative layers of Si_3N_4/SiO_2 pairs. The performance of this Si_3N_4/SiO_2 filter results in very high performance, the transmission over 90%. Figure 5.6 shows the transmission calculated for red, green, and blue optical filters. Their bandpass multilayer structures were achieved by varying in the

thickness for ultra-narrow spectra at 400 nm, 450 nm, 545 nm, and 660 nm. These wavelengths correspond to violet, blue, green, and red colors.

Moreover, based on the Si_3N_4/SiO_2 material system, we designed bandpass filters operating in almost every wavelength in the visible region. Figure 5.7a illustrates seventeen visible bandpass spectra consisting of 400, 405, 410, 420, 450, 470, 530, 535, 550, 560, 575, 590, 600, 630, 650, 660, and 670 nm. Such optical bandpass filters are developed from 96 alternative Si_3N_4/SiO_2 multilayers.

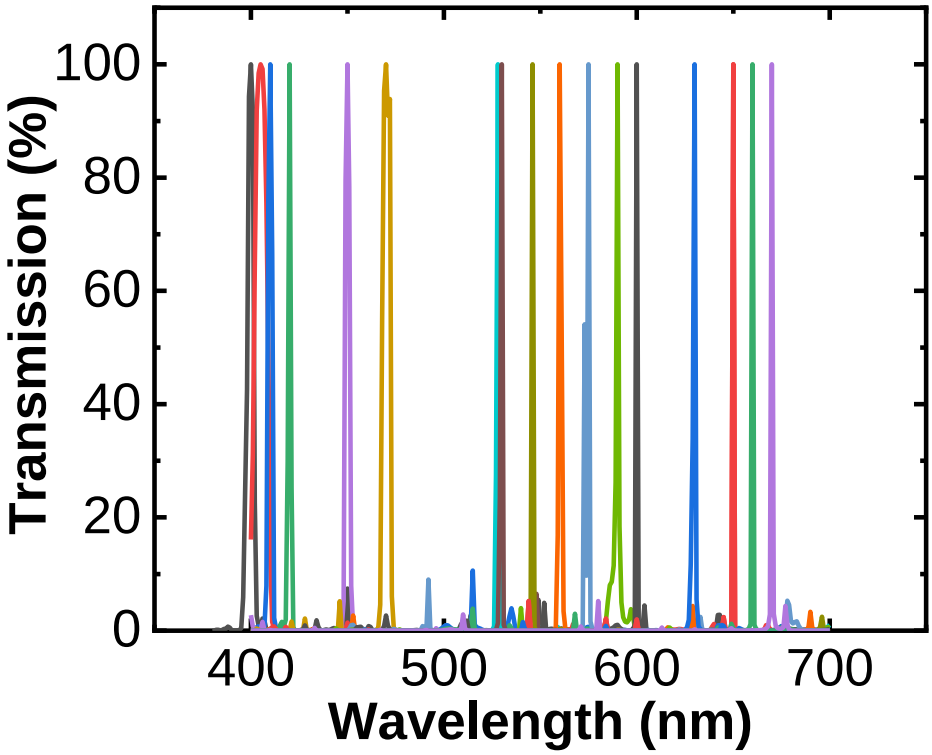

Figure 5.7 (a) The normalized narrow spectra of calculated bandpass filters at different visible wavelengths from the simulations.

Figure 5.8 shows the absorption, transmission, and reflection of sixteen bandpass filters forementioned. The bandpass filters with wavelengths longer than 450 nm have an ultra-narrow passband and nearly 100% transmission.

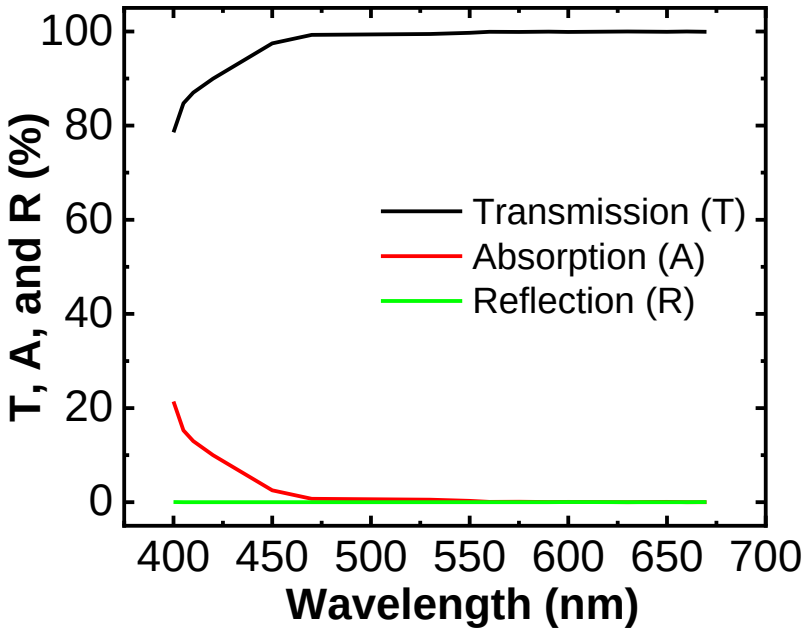

Figure 5.8 The overall transmission, absorption, and reflection of visible bandpass filters.

Although the bandpass filter constructed by a high number of layers obtains an extremely narrow passband, the device deposition of many layers at nanoscale accuracy is quite difficult. In an attempt at the fabrication of narrow band LEDs, narrow bandpass filters are integrated into the typical visible LEDs which typically have the FWHM in the range of 50 and 80 nm. Taking this into account, the integrated bandpass filters only need to operate in a short range of wavelengths within the LED's spectrum so that the spectrum of LEDs passing through the filter becomes a narrower band spectrum. For example, a 550 nm bandpass filter is evaluated for its bandpass performance only in the range of 500 to 600 nm. Even the 550 nm bandpass filter could not block all the out-of-band wavelengths, it still has full value to be integrated into the green LED for obtaining a narrow band emission.

The value of transmission, absorption, and reflection of the filter are presented in Table 5.1 in the next page.

Table 5.1 The Transmission, Absorption, and Reflection of Optical Bandpass Filters Designed with 96 layers of Si_3N_4/SiO_2.

No.	Wavelength (nm)	Transmission	Absorption	Reflection
1.	400	0.785594	0.213909	4.97E-04
2.	405	0.847422	0.152577	1.23E-06
3.	410	0.87004	0.129783	1.77E-04
4.	420	0.89973	0.100072	1.98E-04
5.	450	0.974772	0.025208	1.97E-05
6.	470	0.992596	7.40E-03	3.29E-06
7.	530	0.994475	5.51E-03	1.72E-05
8.	550	0.997217	2.78E-03	8.76E-07
9.	560	0.999204	7.96E-04	4.85E-08
10.	575	0.998914	1.09E-03	2.57E-07
11.	590	0.999633	3.67E-04	1.46E-08
12.	600	0.998801	8.06E-04	3.93E-04
13.	630	0.999874	1.25E-04	1.08E-06
14.	650	0.999294	7.06E-04	4.45E-08
15.	660	0.999842	1.53E-04	5.03E-06
16.	670	0.999365	8.69E-05	5.48E-04

Besides, the bandpass filter including 96 layers of Si_3N_4/SiO_2, a bandpass filter consisting of 21 alternative Si_3N_4/SiO_2 layers acting as a bandpass filter was designed and fabricated. The structure of the bandpass filter is presented in **Table 5.2,** and the total thickness of the filter is 1,853 nm.

Table 5.2 The Detailed Thickness of the Bandpass Filter with 21 Alternative Si_3N_4/SiO_2 Layers Grown on a 0.5 mm Fused Silica Substrate

No	**Materials**	**Thickness** (nm)
1	Si_3N_4	73
2	SiO_2	90
3	Si_3N_4	62
4	SiO_2	83
5	Si_3N_4	60
6	SiO_2	84
7	Si_3N_4	63
8	SiO_2	88
9	Si_3N_4	171
10	SiO_2	74
11	Si_3N_4	55
12	SiO_2	77
13	Si_3N_4	56
14	SiO_2	77
15	Si_3N_4	245
16	SiO_2	77
17	Si_3N_4	56
18	SiO_2	77
19	Si_3N_4	53
20	SiO_2	176
21	Si_3N_4	56

The calculated transmission spectrum of the 21 layer bandpass filter is presented in Figure 5.9. The transmission of the calculated Si_3N_4/SiO_2 bandpass filter is over 95%.

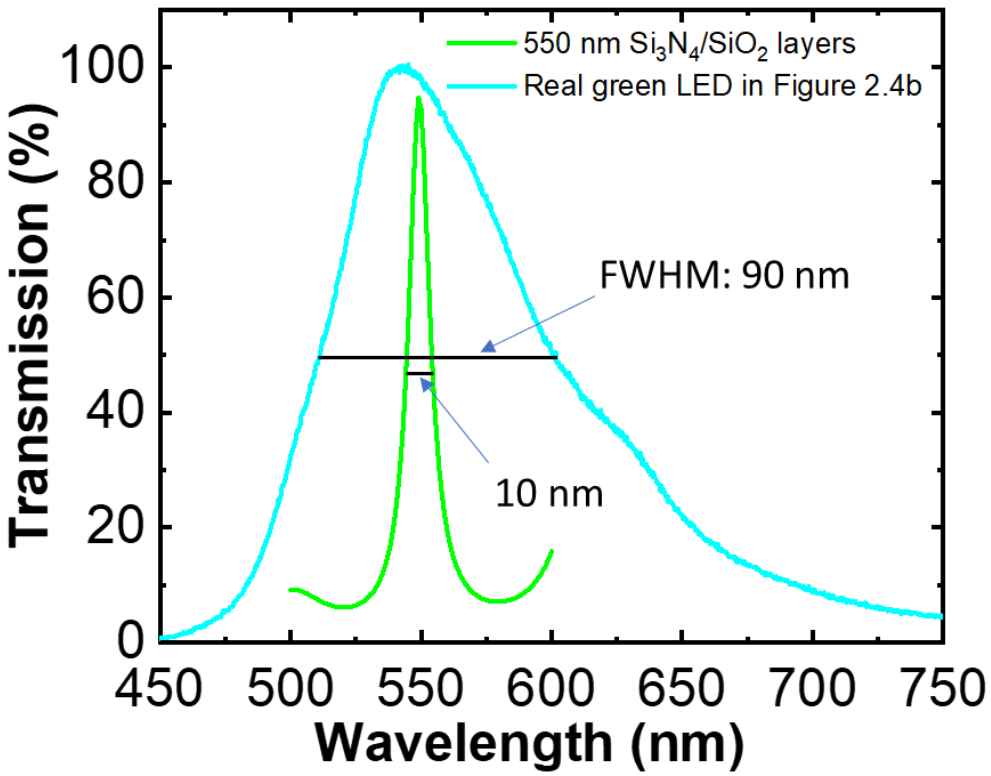

Figure 5.9 The spectrum of the real green LED, and transmission of the bandpass filter with 21 layers of Si_3N_4/SiO_2 on a fused silica substrate.

For comparison, the EL spectrum of a real green μLED device, which has been reported in Figure 2.4b, is also illustrated again in Figure 5.9. The FWHM of transmission spectrum of the bandpass filter achieves a very narrow band of 10 nm, nine times smaller than comparing FWHM of 90 nm from the real green LED, presented in Chapter 2.

Also, the transmission spectrum with different angles of incidence was studied. In addition to high transmission of the expected passband, the filter results in a good angular variation. When the incident angle with respect to the normal to the surface increases, the center wavelength of the emission spectra of the filter shifts into the shorter region, shown

in Figure 5.10. The emission peaks change from 550 nm to 510 nm in respect to incident light from 0 to 45 degree in respect to the normal to the filter's plane, respectively.

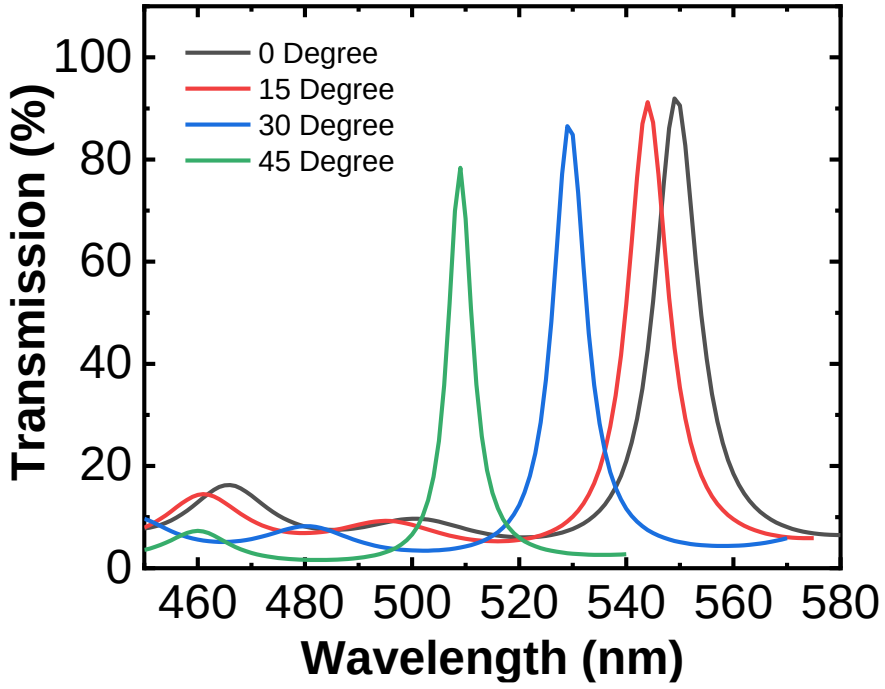

Figure 5.10 The transmission spectra of the Si_3N_4/SiO_2 filter under 0, 15, 30 and 45 degree.

The angular tolerance of the designed filter is 0.98 nm/degree, which is defined as the ratio of the wavelength shift to the incident angles. From the figure, the transmission of the filter reduces in conjunction with increasing angles of incidence. Herein, under 45-degree incident angle, the transmission of the filter is around 80% while under normal incidence (perpendicular to the filter's plane), the transmission is over 90%. The reduced transmission is less than 10% over the 45 degree variation of incident angles. Although the shift of passband spectrum is a drawback of the interference-based filers, this can benefit in some cases. When the bandpass can be tuned by an adjustment of the angle of the incident light as long as the transmission is still high for practical uses.

All-dielectric visible bandpass filters have been fabricated with various tools depending on the accuracy and materials available in the instruments. In this work, Si_3N_4/SiO_2 multilayers were deposited using a PECVD Oxford PlasmaLab 100 system. The substrate's temperature is kept at 350 °C during the deposition process. For Si_3N_4 coatings, the precursors are silane (SiH_4) inflow at 220 sccm, N_2 plasma at 1000 sccm, and NH_3 at 10 sccm. The precursors for the deposition of SiO_2 include SiH_4 at 265 sccm gas, N_2 gas flow is at 500 sccm, and N_2O plasma is at 1000 sccm. The pressure in the growth chamber is approximately 1800 mTorr. The deposition rate is at 72.38 nm/m and 189.4 nm/m for Si_3N_4 and SiO_2, respectively. The fabricated structure of the filter can be seen in the cross-sectional SEM image, shown in Figure 5.11. In the structure, the 9th and 15th layers of Si_3N_4 are 171 nm and 245 nm – the two thickest layers in the structure. They noticeably appear on the SEM image, respectively.

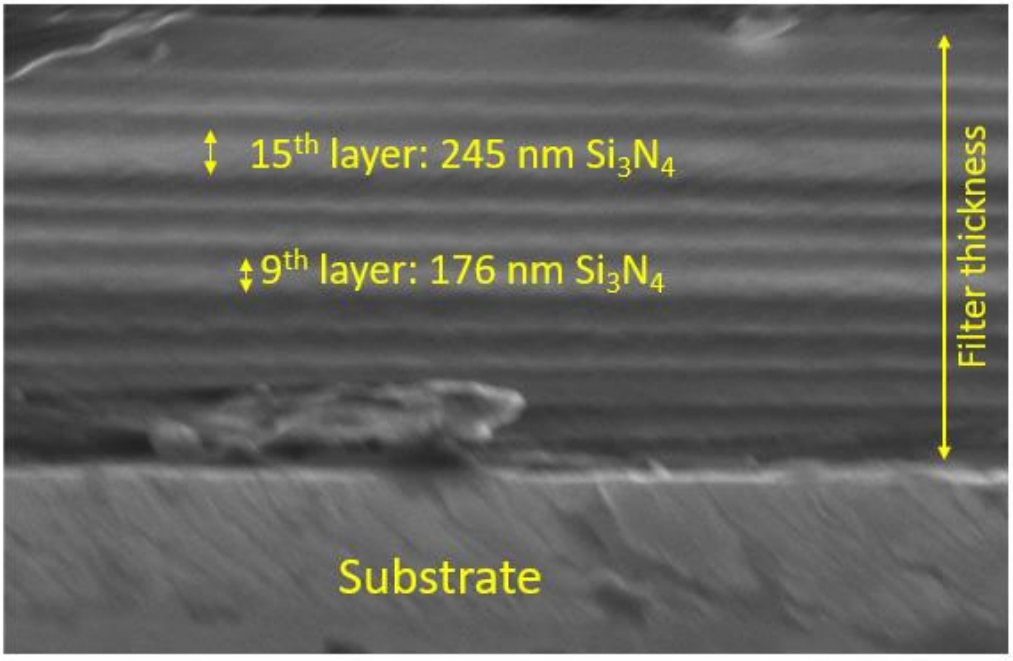

Figure 5.11 The cross-sectional SEM image of 21 alternative Si_3N_4/SiO_2 layers as a 550 nm bandpass filter. The thickness of each layer is presented in Table 5.2.

The performance of the 550 nm Si_3N_4/SiO_2 bandpass filter was evaluated using a reference light source made of off-the-shelf white LEDs. The spectrum of the reference light source is the red curve in Figure 5.12. The green curve is the transmitted spectrum of the 550 bandpass filter.

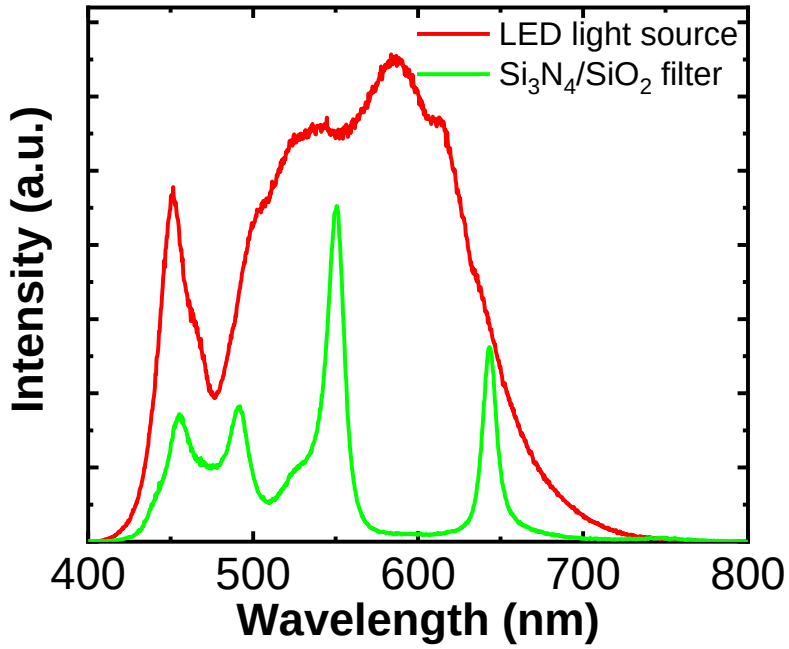

Figure 5.12 The performance of the 550 nm bandpass filter consisting of 21 alternative Si_3N_4/SiO_2 layers deposited with PECVD.

It is seen that the bandpass filter permits a passband around 550 nm to transmit with the highest intensity, compared to others. The passband is very narrow around 550 nm. There is another peak of emission close to 650 nm and the shoulders appear in a range of 400-500 nm region. The spectral features are alike with the calculated spectrum. Because the bandpass filter is to be integrated into green LEDs, the performance of the filter from 500 to 600 nm is interestedly, illustrated in Figure 5.13. The transmission T of the bandpass filter is given by equation 5.3, in which I and I_0 is the transmitted and incident intensity, respectively.

$$T = \frac{I}{I_0} \tag{5.3}$$

In this case, the transmission of the filter is the result of the transmitted intensity divided by the incident intensity of the reference LED light source. The transmission of the bandpass filter is approximately 80%, illustrated in Figure 5.13. The FWHM of the filter is 12 nm, larger than that of the designed filter (10 nm). The wider bandwidth of the experimental filter is attributed to incident light beams coming under a range of angles while the simulated spectrum is calculated under only for perpendicular incidence. The inset of Figure 5.13 shows the fabricated filter on the fused silica substrate. The total thickness of the substrate and filter is 501,853 µm in which 500 µm substrate and 1.853 µm filter.

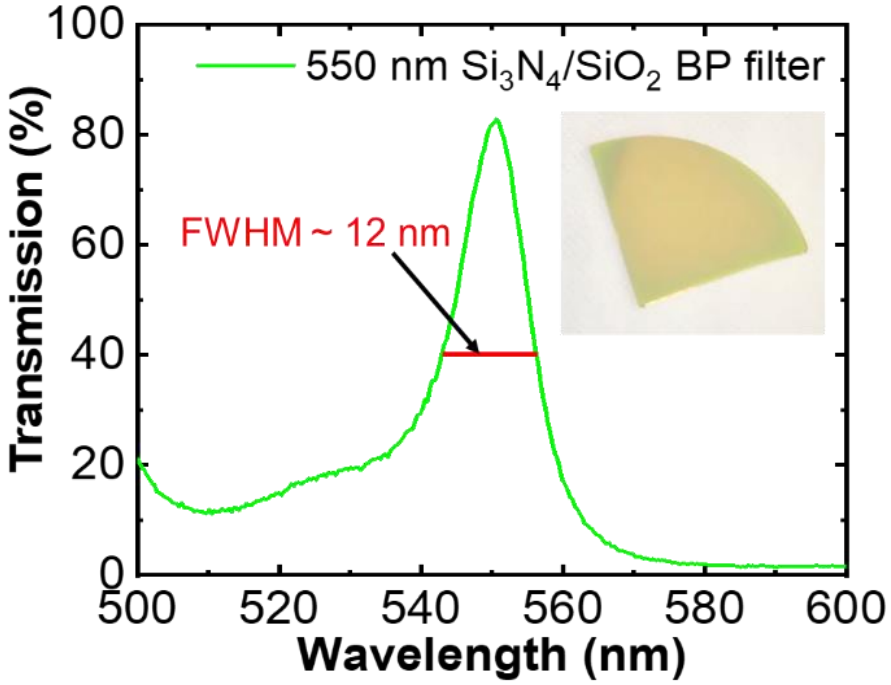

Figure 5.13 The transmission of the 550 nm bandpass filter consisting of 21 alternative Si_3N_4/SiO_2 multilayers.

5.5.4 Design and fabrication of UV bandpass filters

The UV bandpass Fabry-Perot interference filters were designed from metal-dielectric alternative Ag/SiO_2 multilayers. Metal Ag can be used for UV bandpass filters with wavelength down to 300 nm [209]. Given that the number of metal layers of the UV bandpass structure is limited for a high transmission. Three pairs of Ag/SiO_2 were designed for two 310 nm UV bandpass filters. The thickness of Ag layers is set at 10 nm and 20 nm for filter 1 and filter 2, respectively. The SiO_2 layers are the same in both filters and they play a role of cavities where multiple beam reflections of light between two reflecting Ag layers. The detailed layers of two filters are illustrated in Figure 5.14. The total thickness of filter 1 and filter 2 is 163.4 nm and 193.4 nm, respectively.

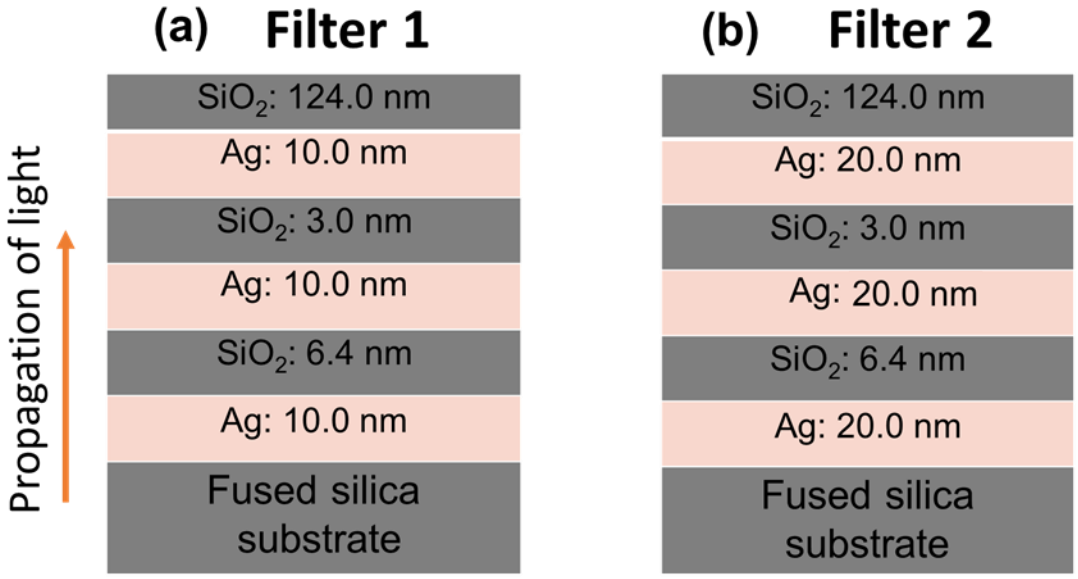

Figure 5.14 The structure of two 310 nm bandpass filters of six alternative Ag/SiO_2 layers.

The transmission characteristics of these filters are calculated by OpenFilters software. Filter 1 with 10 nm Ag layers achieves the transmission over 70% while filter 2 with 20 nm Ag layer obtains nearly 40% transmission. The lower transmission of filter 2

is caused by the higher absorption of Ag with its increasing thickness. However, filter 2 results in a narrower passband compared to filter 1. In metal-dielectric multilayer bandpass filters, the thicker metal layer of a UV filter results in a narrower passband but the transmission is low. In practical applications, a tradeoff between transmission and the narrow band needs to be considered.

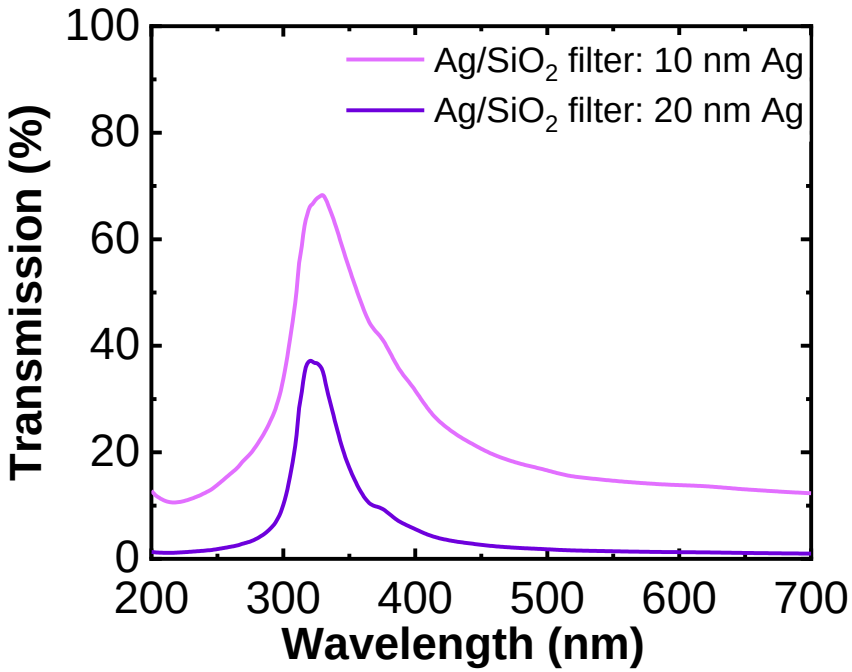

Figure 5.15 The illustration of designed spectra of 310 nm bandpass filters including 6 alternative Ag/SiO_2 layers.

The two filters were implemented using an E-beam evaporator, Orion-8E by AJA International. The thickness can be coated at 0.1 nm accuracy. The deposition rate could be controlled by the high voltage and electron current. The Ag and SiO_2 coatings were deposited in an ultra-high vacuum chamber, approximately at 10^{-7} Torr on 0.5 mm thick double polished fused silica substrates. The substrate has over 90% transmission at 310 nm. Figure 5.16 shows the cross-sectional SEM image of filter 1. Although the SEM image does not clearly detail each layer of the bandpass filter structure, the total measured

thickness of filter 1 is of 162 nm, close to the value from the designed structure (163.4 nm). The passband of the filter 1 and filter 2 measured with a deuterium StellarNet UV light source and the results are presented in Figure 5.17.

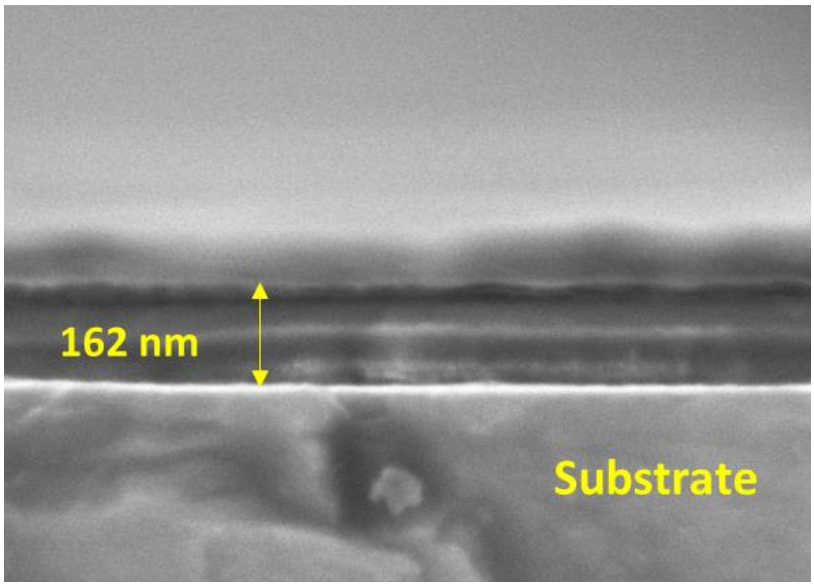

Figure 5.16 The cross-sectional SEM image of Ag/SiO_2 bandpass filter 1.

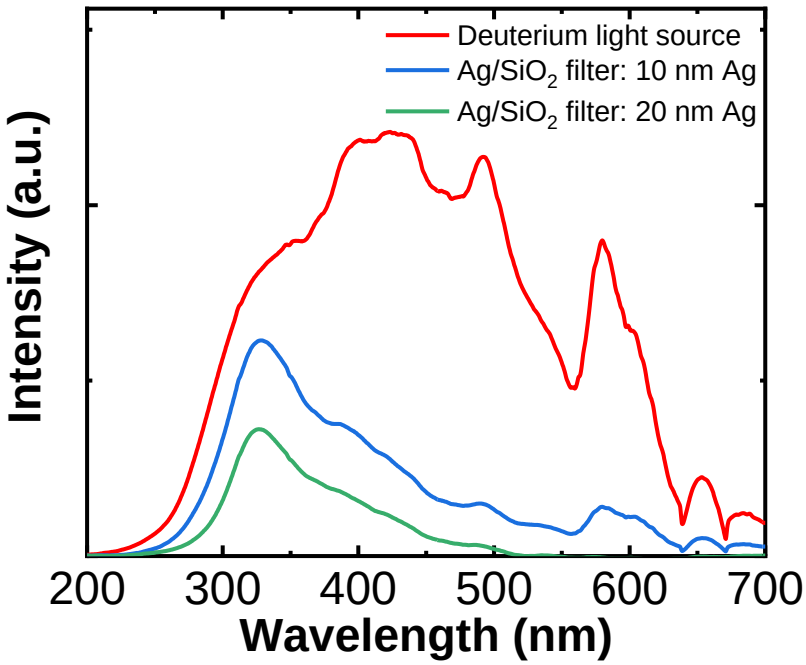

Figure 5.17 Intensity of the deuterium light source, 310 nm bandpass filter 1, and filter 2.

The filters block almost all the visible wavelengths and allow a maximum transmission around 310 nm. The transmission spectra of two fabricated filters are shown in Figure 5.18. The transmission is calculated by equation 5.3.

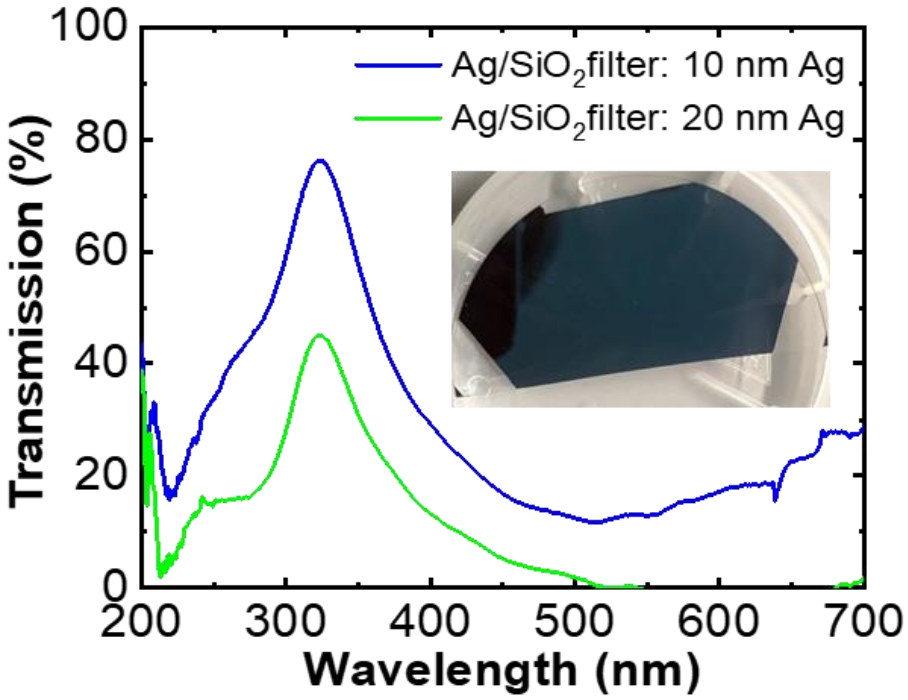

Figure 5.18 The transmission of 310 nm UV bandpass filter 1 with 10 nm Ag and filter 2 with 20 nm Ag. The inset shows the real filter 1 on a 0.5 mm thick fused silica wafer.

It can be seen from Figure 5.17 that the filter 1 of 10 nm Ag has a high transmission over 70% at 310 nm central wavelength while filter 2 with 20 nm Ag bandpass filter obtains only approximately 35% transmission. The thicker metal layer, the lower transmission and a narrower spectral linewidth.

We also investigated new material systems including six alternative layers of Al/Al_2O_3 and Al/MgF_2 for UV bandpass filters. The performance of designed 310 nm bandpass filters based on alternative Al/Al_2O_3 and Al/MgF_2 in Figure 5.19. Due to Al metal is highly reflective down to 200 nm, it is an ideal material for UV bandpass filters. The

spectra achieve a relatively narrow band emission with a FWHM of 26 nm, having the cut-on and cut-off wavelengths around 290 nm and 316 nm, respectively. The narrow passband of the filters is inversely proportional to the transmission. Both bandpass filters achieve a transmission over 35% at 310 nm.

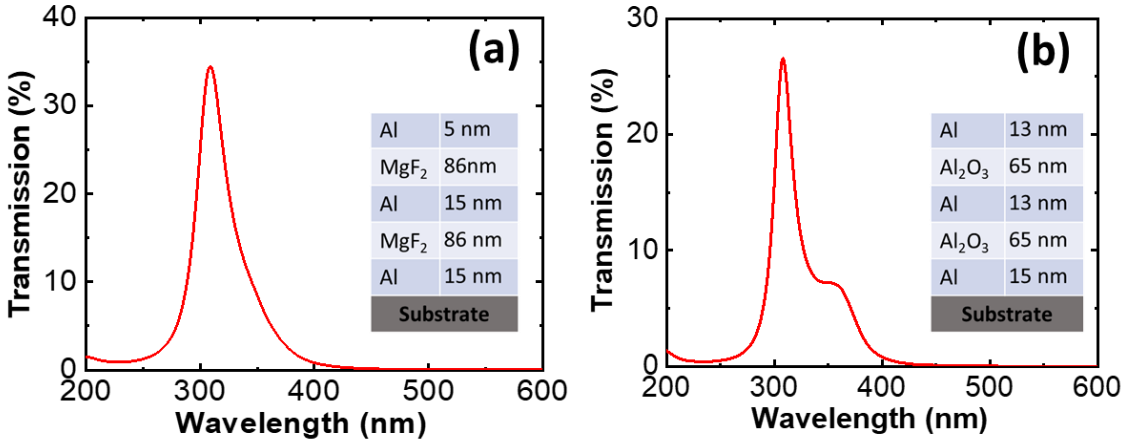

Figure 5.19 (a) The transmission spectra of 310 nm Al/MgF_2 bandpass filters; and (b) that of the Al/Al_2O_3 bandpass filter. The insets show detailed layers of these filters.

5.6 Conclusion

In conclusion, in this chapter, we have presented a simple design of AlGaN/AlN far-UVC LEDs at 222 nm central wavelength. The simulated EL spectrum is narrow of 12 nm FWHM. This simple structure of far-UVC LEDs could be grown with MBE technique. If the EL spectrum of experimental LEDs is not narrow, a 222 nm bandpass filter, made of 6 alternative layers of Al/MgF_2 could be integrated for narrow band far-UVC LEDs. Disinfection with 222 nm far-UVC LEDs is safe for humans and thus it could be the future efficient technology for reducing contagious diseases.

In addition, the 550 nm visible bandpass filter using 21 alternative all-dielectric Si_3N_4/SiO_2 layers and 310 nm UVB bandpass filters using 6 alternative metal-dielectric Ag/SiO_2 layers have been designed and fabricated. The calculated and experimental performance of the filters are highly matched. The visible filter results in a FWHM around 10 nm, five to eight times smaller than the recorded number from typical LEDs. The UV bandpass filters have the broader FWHM and lower transmission, compared to visible bandpass filters. However, the UV LEDs typically achieve a narrow spectral linewidth so that the integration of an UV bandpass filter into UV LEDs would create an expected narrow band emission. Due to the absorption of metal Ag layers, the transmission of the UV bandpass filters is approximately 30-70% and the FWHM is around 70 nm. FWHM is larger than that of UV LEDs, but the filters could block wavelengths in both sides of the central peak so it could make UV LEDs to have a narrower spectrum. More importantly, the UV bandpass filter can block all visible wavelengths, and this feature is very important for order photonic platforms such as solar-blind detectors, machine vision, and hyperspectral cameras. These visible and UV bandpass filters are ready to be integrated into LEDs for narrow band LEDs. The narrow band LEDs have huge applications in disinfection and chronic wound healing treatment using phototherapy.

CHAPTER 6

CONCLUSIONS AND FUTURE WORK

The wide direct tunable bandgap energy, high carrier mobility, and thermal and mechanical properties of III-nitrides are critical for optoelectronics devices. High quality nanowires grown on silicon substrates by MBE techniques have demonstrated the promising solutions for advanced photonic platforms for lighting, next generations of displays, disinfection, phototherapy and so on. Accelerating the development of better LED devices for environmentally friendly technologies is essential for science, technology, and whole societal development.

In this dissertation, PAMBE was successfully employed to grow III-nitride nanowires for visible and UV LEDs towards numerous applications in lighting, display technologies, disinfection, and phototherapy. In the future, an attempt to increase the MBE growth rate of III-nitrides will be implemented. Although PAMBE growth technique is superior to other synthesis methods in terms of crystalline quality and structure complexity, the MBE growth rate is still low (~ 1Å/s), compared to other popular synthesis techniques such as MOCVD. The low rate of MBE growth limits its popularity in the industry. The growth rate of MBE needs to be higher than currently established status to gain benefits in terms of the economic point of view. The more efficient approaches of synthesis of III-nitride nanostructures will result in economic advantages. The faster MBE growth rate of III-nitride nanowires is desirable. Therefore, one of the duties and responsibilities for the ongoing research focuses on improving MBE growth rate.

By changing the composition of Ga/In ratio and growth temperature during the MBE growing process, optimal conditions of III-nitride nanowires on silicon substrates

were realized for visible full-color, white-color, and UV LEDs. Tuning the indium composition of the quantum wells (10%–50%) in the structure of dot-in-wire InGaN/GaN heterostructures for full-color μLEDs and phosphor-free white-color LEDs have successfully demonstrated on silicon substrates, paving the way for monolithic μLED display technologies. These RGB μLEDs with central wavelengths at 645, 550, and 475 nm achieved consistent emissions under injection currents up to 350 mA. It means the QCSE, one of the challenges of LEDs, has been addressed. The combination of different quantum wells with indium composition varied in such a range, the developed white-color LEDs without using phosphors resulted in a desirable color gamut of color rendering index > 92. Phosphor-free white-color LEDs are environmentally friendly, reducing carbon footprint, and help to accelerate the next generation solid-state lighting. Such visible μLEDs are perfectly suited for advanced photonics applications such as the next generation display technology. The solving of some remaining issues of nanowire visible LEDs such as Green Gap, low efficiency of III-nitride green LEDs, would gain benefits to the lighting technology. A special attention will be paid to increase the efficiency of green LEDs.

III-nitrides are only the material system that can be tuned compositionally for a wide range of emissions from UV to IR regions, but EQE of III-nitride green LEDs is still insufficient. Some of the reasons are the difficulty of the epitaxial growth of indium rich-InGaN nanowire LEDs and the large polarization field in the quantum wells, mitigating the radiative recombination. For these reasons, significant attention to utilizing polarization effects and realized growth conditions at a lower temperature may improve the efficiency of true green LEDs. In addition, an investigation of the impact of photonic crystals from different nanowire arrangements could be used to improve LEE. Some of our recent

research has shown that periodic photonic crystals of patterned nanowires lead to a better performance. The hexagonal nanowire arrangement is the best for increasing EQE of LEDs. Adopting this idea of photonic crystals to green LEDs would create the differences in sufficient green LEDs.

Moreover, because the phosphore-free white LEDs are promising for many advanced applications, especially in visible light communication (VLC), the integration of a lighting system for a communication purpose would become a disruptive technology. The nature of high mobility of electrons, III-nitride have been used for visible communications. Lighting and high-speed communication integration by harvesting nanowire phosphor-free white-color LEDs would be one of the directions for our research in coming years and being a part of that trend is exciting.

In terms of UV LEDs, MBE growth conditions for high performance AlGaN nanowire UV LEDs have been mastered so that we have demonstrated AlGaN nanowire UVB and UVA LEDs from 290 nm to 335 nm emission. The performance of UV LEDs has seen an improvement with utilized photonic crystals and surface passivation of the nanowires. The discovered FDTD simulation's results show that ordered nanowires or periodic nanowire structures resulted in a better quality of nanowire UV LEDs in terms of LEE. For example, UVB at 290 nm achieved a high LEE of ~ 90% and 92% for emissions at 290 nm and 320 nm, respectively – higher than that from the random nanowire structures.

Likewise, nonradiative recombination caused by surface defects is reduced with surface passivation for demonstrated 335 nm nanowire UVA LEDs. That using KOH, followed by $(NH_4)_2S_x$ treatment could improve the performance of nanowire UV LEDs at 335 nm central wavelengths was realized. The increases in the EL, optical power, PL, and

I-V characteristics of the 335 nm AlGaN nanowire UV LED after the passivation treatment by 83%, 65%, 49%, and 43%, respectively. Such electrical and optical enhancements are attributed to the reduction of the surface nonradiative recombination. A combination of KOH and $(NH_4)_2S_x$ treatment shows a promising approach for high efficiency and high power AlGaN nanowire UV LEDs. In the future, our research is continued on UV LEDs with surface passivation and photonic crystal, not for UVA and UVB LEDs but for far-UVC LEDs. Because 222 nm UVC LEDs are ideal healthy disinfectant, eliminating contagious diseases spreading in the air and surfaces. The 222 nm UVC LEDs can be used in man-occupied rooms without nearly concern so that the growth of 222 nm UVC LEDs is going be focused and investigated for the disinfection properties in airborne and foodborne pathogens. The simple structure of AlGaN/AlN far-UVC LED has been designed and more structures of far-UVC LEDs and the experimental research will be needed in the future. We are doing research and realizing different nanowire structures as well as MBE conditions for far-UVC AlGaN LEDs. It is likely to use photonic crystals for a sufficient LEE, polarization effects in design, and different doping conditions like alpha doping to improve the hole transport and gain high hole careers in *p*-type semiconductor segments.

Lastly, narrow band LEDs are well suited to biological, medical, and water purification applications due to the selective capability of the interaction with living matters such as bacteria, cells, viruses, and macromolecules. Thus, narrow band LEDs are a novel lighting technology. They can enable new significant applications in advancing phototherapy instruments, safety disinfection systems, and biological imaging. In Chapter 5, we presented numerous bandpass filters on fused silica substrates for visible narrow band

LEDs with over 90% transmission and the FWHM is approximately 12 nm. Based on the same Fabry-Perot bandpass interference principle, narrow band LEDs in almost wavelengths could be achieved. The 550 nm narrow band LEDs have been fabricated with popular all-dielectric multilayers of Si_3N_4/SiO_2 using PECVD. The characteristics of experimental filters are similar to the expected outcome designed by OpenFilters. In addition, UV bandpass filters based on metal-dielectric multilayers have been demonstrated. Due to the absorption of metals, the number of layers is limited in three or four layers and thus the narrow band of the UV filters is not as good as that of visible bandpass filters.

Based on this established work of narrow band LEDs at 550 nm and 310 nm, we will develop and fabricate more bandpass filters in visible and UV regions and integrate them into the LEDs towards the production of narrow band LEDs targeted specific applications. The integration of an on-chip bandpass filter to obtain narrow band LEDs is doable by the deposition of the multilayer structure of the bandpass filter on nanowire LEDs. The 310 nm UV narrow band UV LEDs and 550 nm visible narrow band LEDs have been demonstrated in this dissertation by the deposition of multilayer bandpass structure. New narrow band LEDs at different wavelengths are desirable for many more applications. Therefore, the development of narrow band LEDs at other wavelengths and higher transmission especially in the UV region would receive attention. The structure of the designed alternative Al/Al_2O_3 and Al/MgF_2 would be fabricated and compared their performance to the Ag/SiO_2 bandpass filters.

Our research has demonstrated high performance visible and UV LEDs which have been reported in several articles [34, 95, 115, 119, 312]. Taking advantage of the MBE

system, and the team's expertise, the production of the advanced narrow band LEDs in the ultraviolet and visible wavelengths, suitable for disinfection and wound healing treatment will be reachable. The expected wavelengths can be obtained by the precisely manipulated III-nitride nanowires using MBE growth in terms of the material compounds, morphology, size, and spacing of nanowires by means of controlling the elemental composition, surface morphology, surface passivation, and design. We continue to contribute to photonics science and technology via research and development of new materials, structure, and engineering.

In summary, the advent of the LED has changed the way we light up the world and it continues to change the world we live in. When essential roles of LED could continually be explored, the use of LED will enable critical technologies and science in manufacture, inspection, communication, disinfection, water treatment, medicine requires ongoing efforts, pouring resources and LED based technologies will have greater impacts on the whole society in the next decade.

REFERENCES

[1] J. R. Bolton and C. A. Cotton, *The Ultraviolet Disinfection Handbook*. Denver, CO, USA, American Water Works Association, 2008.

[2] Z. Mi and C. Jagadish, *III-Nitride Semiconductor Optoelectronics*. London, UK, Academic Press, 2017.

[3] T. Koutchma, *Ultraviolet Light in Food Technology: Principles and Applications*. Boca Raton, FL, CRC press, 2019.

[4] W. J. Masschelein and R. G. Rice, *Ultraviolet Light in Water and Wastewater Sanitation*. Boca Raton, FL, CRC Press, 2017.

[5] P. J. Aphalo, A. Albert, L. O. Björn, A. R. McLeod, T. M. Robson, and E. Rosenqvist, *Beyond the Visible: A Handbook of Best Practice in Plant UV Photobiology*. COST Action FA0906 UV4growth. Helsinki: University of Helsinki, Division of Plant Biology, Helsinki, Finland, 2012.

[6] E. F. Schubert, *Light-Emitting Diodes*, Troy, NY, USA, E. Fred Schubert, 2018.

[7] K. Wladyslaw, *Ultraviolet Germicidal Irradiation Handbook: UVGI for Air and Surface Disinfection*. New York, NY, USA, Springer, 2010.

[8] M. Kneissl and J. Rass, *III-Nitride Ultraviolet Emitters* (Springer Series in Materials Science). vol. 227, New York, NY, USA, Springer, 2016.

[9] J. Dong and D. Xiong, "Applications of Light Emitting Diodes in Health Care," *Annals of Biomedical Engineering*, vol. 45, no. 11, pp. 2509-2523, 2017.

[10] C. D'Souza, H.-G. Yuk, G. H. Khoo, and W. Zhou, "Application of Light-Emitting Diodes in Food Production, Postharvest Preservation, and Microbiological Food Safety," *Comprehensive Reviews in Food Science and Food Safety*, vol. 14, no. 6, pp. 719-740, 2015.

[11] M. Koike, N. Shibata, H. Kato, and Y. Takahashi, "Development of High Efficiency GaN-Based Multiquantum-Well Light Emitting Diodes and Their Applications," *IEEE Journal of Selected Topics in Quantum Electronics*, vol. 8, no. 2, pp. 271-277, 2002.

[12] A. Fujioka, T. Misaki, T. Murayama, Y. Narukawa, and T. Mukai, "Improvement in Output Power of 280-nm Deep Ultraviolet Light-Emitting Diode by Using AlGaN Multi Quantum Wells," *Applied Physics Express*, vol. 3, no. 4, 2010.

[13] S. Nakamura, M. Senoh, N. Iwasa, and S. Nagahama, "High-Brightness InGaN Blue, Green and Yellow Light-Emitting Diodes with Quantum Well Structures," *Japanese Journal of Applied Physics*, vol. 34, no. 7A, 2, pp. L797-L799, 1995.

[14] J. Q. Wu, "When group-III nitrides go infrared: New Properties and Perspectives," *Journal of Applied Physics*, vol. 106, no. 1, pp. 011101-011128, 2009.

[15] J. Piprek, *Nitride Semiconductor Devices: Principles And Simulation*. Berlin, Germany, Wiley-VCH, 2007.

[16] B. Arnaudov, T. Paskova, P. P. Paskov, B. Magnusson, E. Valcheva, B. Monemar, H. Lu, W. J. Schaff, H. Amano, and I. Akasaki, "Energy Position of Near-Band-Edge Emission Spectra of InN Epitaxial Layers with Different Doping Levels," *Physical Review B,* vol. 69, no. 11, pp. 115216-5, 2004.

[17] H. P. Maruska and J. J. Tietjen, "The Preparation and Properties of Vapor-Deposited Single-Crystal-Line GaN," *Applied Physics Letters,* vol. 15, no. 10, pp. 327-329, 1969.

[18] F. Medjdoub, ed. *Gallium Nitride (GaN): Physics, Devices, and Technology*. New York, NY, CRC Press, 2017.

[19] H. P. T. Nguyen, S. Zhang, K. Cui, X. Han, S. Fathololoumi, M. Couillard, G. A. Botton, and Z. Mi, "p-Type Modulation Doped InGaN/GaN dot-in-a-wire White-Light-Emitting Diodes Monolithically Grown on Si(111)," *Nano Letters*, vol. 11, no. 5, pp. 1919-1924, 2011.

[20] F. Chen, X. Ji, and S. P. Lau, "Recent Progress in Group III-Nitride Nanostructures: from Materials to Applications," *Materials Science and Engineering R*, vol. 142, pp. 100578 (1-55), 2020.

[21] J. Li, D. Wang, and R. R. LaPierre, *Advances in III-V Semiconductor Nanowires and Nanodevices*. Sharjah, UAE, Bentham Science Publishers, 2011.

[22] S. Zhao, H. P. T. Nguyen, M. G. Kibria, and Z. Mi, "III-Nitride Nanowire Optoelectronics," *Progress in Quantum Electronics*, vol. 44, pp. 14-68, 2015.

[23] H. Sun and X. Li, "Recent Advances on III-Nitride Nanowire Light Emitters on Foreign Substrates – Toward Flexible Photonics," *Physica Status Solidi (a)*, vol. 216, no. 2, pp. 1800420(1-13), 2018.

[24] R. T. Velpula, B. Jain, H. Q. T. Bui, and H. P. T. Nguyen, "Full-Color III-Nitride Nanowire Light-Emitting Diodes," *Journal of Advanced Engineering and Computation*, vol. 3, no. 4, pp. 551-588, 2019.

[25] W. Guo, M. Zhang, P. Bhattacharya, and J. Heo, "Auger Recombination in III-Nitride Nanowires and Its Effect on Nanowire Light-Emitting Diode Characteristics," *Nano Letters*, vol. 11, no. 4, pp. 1434-1438, 2011.

[26] C. Zhao, T. K. Ng, R. T. Elafandy, A. Prabaswara, G. B. Consiglio, I. A. Ajia, I. S. Roqan, B. Janjua, C. Shen, J. Eid, A. Y. Alyamani, M. M. El-Desouki, and B. S. Ooi, "Droop-Free, Reliable, and High-Power InGaN/GaN Nanowire Light-

Emitting Diodes for Monolithic Metal-Optoelectronics," *Nano Letters*, vol. 16, no. 7, pp. 4616-4623, 2016.

[27] H. P. T. Nguyen, K. Cui, S. Zhang, M. Djavid, A. Korinek, G. A. Botton, and Z. Mi, "Controlling Electron Overflow in Phosphor-Free InGaN/GaN Nanowire White Light-Emitting Diodes," *Nano Letters*, vol. 12, no. 3, pp. 1317-1323, 2012.

[28] H. Q. T. Bui, R. T. Velpula, B. Jain, O. H. Aref, H. D. Nguyen, T. R. Lenka, and H. P. T. Nguyen, "Full-Color InGaN/AlGaN Nanowire Micro Light-Emitting Diodes Grown by Molecular Beam Epitaxy: A Promising Candidate for Next Generation Micro Displays," *Micromachines*, vol. 10, no. 8, pp. 492-499, 2019.

[29] F. Glas, "Critical Dimensions for The Plastic Relaxation of Strained Axial Heterostructures in Free-Standing Nanowires," *Physical Review B*, vol. 74, no. 12, pp. 121302-4, 2006.

[30] N. H. Tran, B. H. Le, S. Zhao, and Z. Mi, "On the Mechanism of Highly Efficient p-Type Conduction of Mg-Doped Ultra-Wide-Bandgap AlN Nanostructures," *Applied Physics Letters*, vol. 110, no. 3, pp. 032102-5, 2017.

[31] S. Zhao, B. H. Le, D. P. Liu, X. D. Liu, M. G. Kibria, T. Szkopek, H. Guo, and Z. Mi, "p-Type InN Nanowires," *Nano Letters*, vol. 13, no. 11, pp. 5509-5513, 2013.

[32] S. Zhao, A. T. Connie, M. H. Dastjerdi, X. H. Kong, Q. Wang, M. Djavid, S. Sadaf, X. D. Liu, I. Shih, H. Guo, and Z. Mi, "Aluminum nitride nanowire light emitting diodes: Breaking the fundamental bottleneck of deep ultraviolet light sources," *Scientific Report*, vol. 5, pp. 8332-5, 2015.

[33] S. Zhao and Z. Mi, "Recent Advances on p-Type III-Nitride Nanowires by Molecular Beam Epitaxy," *Crystals*, vol. 7, no. 9, pp. 268(1-17), 2017.

[34] M. R. Philip, D. D. Choudhary, M. Djavid, M. N. Bhuyian, T. H. Q. Bui, D. Misra, A. Khreishah, J. Piao, H. D. Nguyen, K. Q. Le, and H. P. T. Nguyen, "Fabrication of Phosphor-Free III-Nitride Nanowire Light-Emitting Diodes on Metal Substrates for Flexible Photonics," *ACS Omega*, vol. 2, no. 9, pp. 5708-5714, 2017.

[35] A. Y. Polyakov, T. Kim, I. H. Lee, and S. J. Pearton, "III-Nitride Nanowires as Building Blocks for Advanced Light Emitting Diodes," *Physica Status Solidi (b)*, vol. 256, no. 5, pp. 1800589(1-14), 2019.

[36] V. Ramesh, A. Kikuchi, K. Kishino, M. Funato, and Y. Kawakami, "Strain Relaxation Effect by Nanotexturing InGaN/GaN Multiple Quantum Well," *Journal of Applied Physics*, vol. 107, no. 11, pp. 114303-114306, 2010.

[37] J. Bai, Q. Wang, and T. Wang, "Characterization of InGaN-Based Nanorod Light Emitting Diodes with Different Indium Compositions," *Journal of Applied Physics*, vol. 111, no. 11, 2012.

[38] Q. Li, K. R. Westlake, M. H. Crawford, R. Stephen, D. D. Lee, and J. J. Koleske, K. C. Cross, S. Fathololoumi, Z. Mi, and G.T. Wang, "Optical Performance of Top-Down Fabricated InGaN/GaN Nanorod Light Emitting Diode Arrays," *Optics Express*, vol. 19, no. 25, pp. 25528-25534, 2011.

[39] R. S. Wagner and W. C. Ellis, "Vapor-Liquid-Solid Mechanism of Single Crystal Growth," *Applied Physics Letters***,** vol. 4, no. 5, pp. 89-90, 1964.

[40] K. A. Bertness, A. Roshko, L. M. Mansfield, T. E. Harvey, and N. A. Sanford, "Mechanism for Spontaneous Growth of GaN Nanowires with Molecular Beam Epitaxy," *Journal of Crystal Growth***,** vol. 310, no. 13, pp. 3154-3158, 2008.

[41] R. K. Debnath, R. Meijers, T. Richter, T. Stoica, R. Calarco, and H. Luth, "Mechanism of Molecular Beam Epitaxy Growth of GaN Nanowires on Si(111)," *Applied Physics Letters***,** vol. 90, no. 12, pp. 123117-3, 2007.

[42] J. Orton, and T. Foxon, *Molecular Beam Epitaxy: A Short History*. Oxford, UK, Oxford University Press, 2015.

[43] S. Zhao, R. Wang, S. Chu, and Z. Mi, "Molecular Beam Epitaxy of III-Nitride Nanowires: Emerging Applications from Deep-Ultraviolet Light Emitters and Micro-LEDs to Artificial Photosynthesis," *IEEE Nanotechnology Magazine***,** vol. 13, no. 2, pp. 6-16, 2019.

[44] S. Irvine, and Peter Capper, *Metalorganic Vapor Phase Epitaxy (MOVPE)*. Hoboken, NJ, Wiley, 2019.

[45] T. Kuykendall, P. Pauzauskie, S. Lee, Y. Zhang, J. Goldberger, P. Yang, "Metalorganic chemical vapor deposition route to GaN nanowires with triangular cross sections," *Nano Letter*, vol. 2, no. 8, pp. 1063–1066, 2003.

[46] O. Schön, B. Schineller, M. Heuken, and R. Beccard, "Comparison of hydrogen and nitrogen as carrier gasfor MOVPE growth of GaN," *Journal of Crystal Growth*, vol. 189–190, pp. 335-339, 1998.

[47] J. Su, G. Cui, M. Gherasimova, H. Tsukamoto, J. Han, D. Ciuparu, S. Lim, L. Pfefferle, Y. He, A. V. Nurmikko, C. Broadbridge, and A. Lehman, "Catalytic growth of group III-nitride nanowires and nanostructures by metalorganic chemical vapor deposition," *Applied Physics Letters*, vol. 86, no. 1, pp. 013105-3, 2005.

[48] J. Su, M. Gherasimova, G. Cui, H. Tsukamoto, J. Han, T. Onuma, M. Kurimoto, S. F. Chichibu, C. Broadbridge, Y. He, and A. V. Nurmikko, "Growth of AlGaN nanowires by metalorganic chemical vapor deposition," *Applied Physics Letters*, vol. 87, no. 18, pp. 183108-3, 2005.

[49] P. Deb, H. Kim, V. Rawat, M.Oliver, S. Kim, M. Marshall, E. Stach, and T. Sands, "Faceted and Vertically Aligned GaN Nanorod Arrays Fabricated without Catalysts or Lithography," *Nano Letters***,** vol. 5, no. 9, pp. 1847-1851, 2005.

[50] K. Tomioka, T. Tanaka, S. Hara, K. Hiruma, and T. Fukui, "III–V Nanowires on Si Substrate: Selective-Area Growth and Device Applications," *IEEE Journal of Selected Topics in Quantum Electronics*, vol. 17, no. 4, pp. 1112-1129, 2011.

[51] D. H. Stephen, X. Sun, and X. Wang, "The Controlled Growth of GaN Nanowires," *Nano Letters*, vol. 6, no. 8, pp. 1808–1811, 2006.

[52] A. Y. Cho, and J. R. Arthur, "Molecular Beam Epitaxy," *Progress in Solid State Chemical*, vol. 10, no. 3, pp. 157-191, 1975.

[53] H. P. Nguyen, K. Cui, S. Zhang, S. Fathololoumi, and Z. Mi, "Full-color InGaN/GaN dot-in-a-wire Light Emitting Diodes on Silicon," *Nanotechnology*, vol. 22, no. 44, p. 445202, 2011.

[54] M. Mata, X. Zhou, F. Furtmayr, J. Teubert, S. Gradečak, M. Eickhoff, A. Fontcuberta i Morral, and J. Arbiol, "A Review of MBE Grown 0D, 1D and 2D Quantum Structures in a Nanowire," *Journal of Materials Chemistry C*, vol. 1, no. 28, pp. 4300-4312, 2013.

[55] C. Skierbiszewski, H. Turski, G. Muziol, M. Siekacz, M. Sawicka, G. Cywiński, Z. R. Wasilewski, and S. Porowski, "Nitride-Based Laser Diodes Grown by Plasma-Assisted Molecular Beam Epitaxy," *Journal of Physics D: Applied Physics*, vol. 47, no. 7, pp. 073001(1-18), 2014.

[56] J. M. Van Hove, R. Hickman, J. J. Klaassen, P. P. Chow, and P. P. Ruden, "Ultraviolet-Sensitive, Visible-Blind GaN Photodiodes Fabricated By Molecular Beam Epitaxy," *Applied Physics Letters*, vol. 70, no. 17, pp. 2282-2284, 1997.

[57] M. Henini, *Molecular Beam Epitaxy: From Research to Mass Production*. Waltham, MA, USA, Elsevier, 2012.

[58] H. Sekiguchi, K. Kishino, and A. Kikuchi, "Ti-Mask Selective-Area Growth of GaN by RF-Plasma-Assisted Molecular-Beam Epitaxy for Fabricating Regularly Arranged InGaN/GaN Nanocolumns," *Applied Physics Express*, vol. 1, no. 12, pp. 124002-3, 2008.

[59] A. B. Encabo, F. Barbagini, S. Fernandez-Garrido, J. Grandal, J. Ristic, M. A. Sanchez-Garcia, E. Calleja, U. Jahn, E. Luna, and A. Trampert, "Understanding the Selective Area Growth of GaN Nanocolumns by MBE Using Ti Nanomasks," *Journal of Crystal Growth*, vol. 325, no. 1, pp. 89-92, 2011.

[60] B. H. Le, S. Zhao, X. Liu, S. Y. Woo, G. A. Botton, and Z. Mi, "Controlled Coalescence of AlGaN Nanowire Arrays: An Architecture for Nearly Dislocation-Free Planar Ultraviolet Photonic Device Applications," *Advanced Materials*, vol. 28, no. 38, pp. 8446-8454, 2016.

[61] T. Schumann, T. Gotschke, F. Limbach, T. Stoica, and R. Calarco, "Selective-Area Catalyst-Free MBE Growth of GaN Nanowires Using A Patterned Oxide Layer," *Nanotechnology,* vol. 22, no. 9, pp. 095603(1-6), 2011.

[62] J. E. Kruse, L. Lymperakis, S. Eftychis, A. Adikimenakis, G. Doundoulakis, K. Tsagaraki, M. Androulidaki, A. Olziersky, P. Dimitrakis, V. Ioannou-Sougleridis, P. Normand, T. Koukoula, T. Kehagias, P. Komninou, G. Konstantinidis, and A. Georgakilas, "Selective-Area Growth of GaN Nanowires on SiO_2-Masked Si (111) Substrates by Molecular Beam Epitaxy," *Journal of Applied Physics,* vol. 119, no. 22, pp. 224305-10, 2016.

[63] M. Musolino, A. Tahraoui, S. Fernandez-Garrido, O. Brandt, A. Trampert, L. Geelhaar, and H. Riechert, "Compatibility of the Selective Area Growth of GaN Nanowires on AlN-Buffered Si Substrates with the Operation of Light Emitting Diodes," *Nanotechnology,* vol. 26, no. 8, p. 085605(1-8), 2015.

[64] K. A. Bertness, A. W. Sanders, D. M. Rourke, T. E. Harvey, A. Roshko, J. B. Schlager, and N. A. Sanford, "Controlled Nucleation of GaN Nanowires Grown with Molecular Beam Epitaxy," *Advanced Functional Materials,* vol. 20, no. 17, pp. 2911-2915, 2010.

[65] H. P. T. Nguyen, M. Djavid, K. Cui, and Z. Mi, "Temperature-Dependent Nonradiative Recombination Processes in GaN-Based Nanowire White-Light-Emitting Diodes on Silicon," *Nanotechnology,* vol. 23, no. 19, pp. 194012(1-6), 2012.

[66] DOE Solid-State Lighting Program, Modest Investments, Extraordinary Impacts" Derpartment of Energy, Energy Efficiency & Renewable Energy, Building Technologies Office, vol. DOE/EE-1149, 2014.

[67] K.-J. Chen, H.-C. Chen, K.-A. Tsai, C.-C. Lin, H.-H. Tsai, S.-H. Chien, B.-S. Cheng, Y.-J. Hsu, M.-H. Shih, C.-H. Tsai, H.-H. Shih, and H.-C. Kuo, "Resonant-Enhanced Full-Color Emission of Quantum-Dot-Based Display Technology Using a Pulsed Spray Method," *Advanced Functional Materials*, vol. 22, no. 24, pp. 5138-5143, 2012.

[68] M. Hartensveld and J. Zhang, "Monolithic Integration of GaN Nanowire Light-Emitting Diode with Field Effect Transistor," *IEEE Electron Device Letters,* vol. 40, no. 3, pp. 427-430, 2019.

[69] A. F. McDonagh, "Phototherapy: From Ancient Egypt to the New Millennium," *Journal of Perinatology,* vol. 21, pp. S7-S12, 2001.

[70] *NobelPrize.org*, The Nobel Prize in Physiology or Medicine 1903. Nobel Media AB 2019. Accessed on5 Feb 2021. Available at: <https://www.nobelprize.org/prizes/medicine/1903/summary/>

[71] D. Barolet, "Light-emitting diodes (LEDs) in Dermatology," *Seminars in Cutaneous Medicine and Surgery,* vol. 27, no. 4, pp. 227-238, 2008.

[72] M. Mohammadizadeh, F. K. Eliadarani,and Z. Badiei, "Is The Light-Emitting Diode A Better Light Source Than Fluorescent Tube for Phototherapy of Neonatal Jaundice in Preterm Infants?," *Advanced Biomedical Research,* vol. 1, pp. 51-5, 2012.

[73] H. T. Whelan, L. S. Robert, E. V. Buchman, S. G. Turner, D. A. Margolis, V. Cevenini, H. Stinson, R. Ignatius, T. Martin, J. Cwiklinski, "Effect of NASA Light-Emitting Diode Irradiation on Wound Healing," *Journal of Clinical Laser Medicine & Surgery,* vol. 19, no. 16, pp. 305-314, 2001.

[74] H. T. Whelan, E. V. Buchman, A. Dhokalia, M. P. Kane, N. T. Whelan, T. T. W. R. Margaret, J. T. Eells, L. J. Gould, R. Hammamieh, R. Das, M. Jett, "Effect of NASA Light-Emitting Diode Irradiation on Molecular Changes for Wound Healing in Diabetic Mice," *Journal of Clinical Laser Medicine & Surgery,* vol. 21, no. 2, pp. 67-74, 2003.

[75] T. P. Thai, D. H. Keast. K. E. Campbell, M. G. Woodbury, and P. E. Houghton, "Effect of Ultraviolet Light C on Bacterial Colonization in Chronic Wounds," *Ostomy Wound Manage,* vol. 51, no. 10, pp. 32-45, 2005.

[76] T. Dai, A. Gupta, Y. Y. Huang, M. E. Sherwood, C. K. Murray, M. S. Vrahas, T. Kielian, and M. R. Hamblin, "Blue Light Eliminates Community-Acquired Methicillin-Resistant Staphylococcus Aureus in Infected Mouse Skin Abrasions," *Photomedicine and Laser Surgery,* vol. 31, no. 11, pp. 531-538, 2013.

[77] A. Gupta, P. Avci, T. Dai, Y. Y. Huang, and M. R. Hamblin, "Ultraviolet Radiation in Wound Care: Sterilization and Stimulation," *Advance Wound Care (New Rochelle),* vol. 2, no. 8, pp. 422-437, 2013.

[78] A. P. C. De Sousa, J. N.Santos, J. A. D. Reis Jr., T. A. Ramos, J. D. Souza, M. C. T. Cangussú, and A. L. B. Pinheiro, "Effect of LED Phototherapy of Three Distinct Wavelengths on Fibroblasts on Wound Healing A Histological Study in A Rodent Model," *Photomedicine and Laser Surgery,* vol. 28, no. 4, pp. 547-552, 2010.

[79] M. E. Chaves, A. R. Araujo, A. C. Piancastelli, and M. Pinotti, "Effects of Low-Power Light Therapy on Wound Healing: LASER x LED," *Anais Brasileiros de Dermatologia,* vol. 89, no. 4, pp. 616-623, 2014.

[80] E. Virey, "Are microLEDs Really the Next Display Revolution?," *Information Display,* vol. 34, no. 3, pp. 22-27, 2018.

[81] M. K. Choi, J. Yang, T. Hyeon, and D.-H. Kim, "Flexible Quantum Dot Light-Emitting Diodes for Next-Generation Displays," *npj Flexible Electronics,* vol. 2, no. 1, pp. 1-14, 2018.

[82] Y. Sun, Y. Jiang, X. W. Sun, S. Zhang, and S. Chen, "Beyond OLED: Efficient Quantum Dot Light-Emitting Diodes for Display and Lighting Application," *The Chemical Record*, vol. 19, no. pp. 1729-1752. 2019.

[83] X. Zhang, P. Li, X. Zou, J. Jiang, S. H. Yuen, C. W. Tang, and K. M. Lau, "Active Matrix Monolithic LED Micro-Display Using GaN-on-Si Epilayers," *IEEE Photonics Technology Letters***,** vol. 31, no. 11, pp. 865-868, 2019.

[84] L. Z. Jun, C. W. Cheung, W. K. Ming, and L. K. May, "360 PPI Flip-Chip Mounted Active Matrix Addressable Light Emitting Diode on Silicon (LEDoS) Micro-Displays," *Journal of Display Technology***,** vol. 9, no. 8, pp. 678-682, 2013.

[85] K. Ding, V. Avrutin, N. Izyumskaya, Ü. Özgür, and H. Morkoç, "Micro-LEDs, A Manufacturability Perspective," *Applied Sciences***,** vol. 9, no. 6, pp.1206(1-15), 2019.

[86] L. Zhang, F. Ou, W. C. Chong, Y. Chen, and Q. Li, "Wafer-Scale Monolithic Hybrid Integration of Si-Based IC and III-V Epi-Layers-A Mass Manufacturable Approach for Active Matrix Micro-LED Micro-Displays," *Journal of the Society for Information Display***,** vol. 26, no. 3, pp. 137-145, 2018.

[87] R. S. Cok, M. Meitl, R. Rotzoll, G. Melnik, A. Fecioru, A. J. Trindade, B. Raymond, S. Bonafede, D. Gomez, T. Moore, C. Prevatte, E. Radauscher, S. Goodwin, P. Hines, and C. A. Bower, "Inorganic Light-Emitting Diode Displays Using Micro-Transfer Printing," *Journal of the Society for Information Display***,** vol. 25, no. 10, pp. 589-609, 2017.

[88] B. Corbetta, R. Loi, W. Zhoub, D. Liu, Z. Ma, "Transfer Print Techniques for Heterogeneous Integration of Photonic Components," *Progress in Quantum Electronics***,** vol. 52, pp. 1-17, 2017.

[89] S.-W. H. Chen, C.-C. Shen, T. Wu, Z.-Y. Liao, L.-F. Chen, J.-R. Zhou, C.-F. Lee, C.-H. Lin, C.-C. Lin, C.-W. Sher, P.-T. Lee, A.-J. Tzou, Z. Chen, and H.-C. Kuo, "Full-Color Monolithic Hybrid Quantum Dot Nanoring Micro Light-Emitting Diodes with Improved Efficiency Using Atomic Layer Deposition and Nonradiative Resonant Energy Transfer," *Photonics Research***,** vol. 7, no. 4, pp. 416-422, 2019.

[90] C.-H. Teng, L. Zhang, H. Deng, and P.-C. Ku, "Strain-Induced Red-Green-Blue Wavelength Tuning in InGaN Quantum Wells," *Applied Physics Letters***,** vol. 108, no. 7, pp. 071104-4, 2016.

[91] K. Chung, J. Sui, B. Demory, and P.-C. Ku, "Color Mixing From Monolithically Integrated InGaN-Based Light-Emitting Diodes by Local Strain Engineering," *Applied Physics Letters***,** vol. 111, no. 4, pp. 041101, 2017.

[92] R. Wang, H. P. T. Nguyen, A. T. Connie, J. Lee, I. Shih, and Z. Mi, "Color-Tunable, Phosphor-Free InGaN Nanowire Light-Emitting Diode Arrays Monolithically Integrated On Silicon," *Optics Express***,** vol. 22, no. 7, pp. A1768-1775, 2014.

[93] H. Sekiguchi, K. Kishino, and A. Kikuchi, "Emission Color Control From Blue to Red with Nanocolumn Diameter of InGaN/GaN Nanocolumn Arrays Grown on Same Substrate," *Applied Physics Letters***,** vol. 96, no. 23, pp. 231104-4, 2010.

[94] Y. H. Ra, R. Wang, S. Y. Woo, M. Djavid, S. M. Sadaf, J. Lee, G. A. Botton, and Z. Mi, "Full-Color Single Nanowire Pixels for Projection Displays," *Nano Letters***,** vol. 16, no. 7, pp. 4608-4615, 2016.

[95] M. R. Philip, D. D. Choudhary, M. Djavid, M. N. Bhuyian, J. Piao, T. T. Pham, D. Misra, and H. P. T. Nguyen, "Controlling Color Emission of InGaN/AlGaN Nanowire Light-Emitting Diodes Grown by Molecular Beam Epitaxy," *Journal of Vacuum Science & Technology B, Nanotechnology and Microelectronics: Materials, Processing, Measurement, and Phenomena***,** vol. 35, no. 2, pp. 02B108-5, 2017.

[96] M. H. Kim, M. F. Schubert, Q. Dai, J. K. Kim, E. F. Schubert, J. Piprek, and Y. Park, "Origin of Efficiency Droop in GaN-Based Light-Emitting Diodes," *Applied Physics Letters***,** vol. 91, pp. 183507-3, 2007.

[97] M. F. Schubert, J. Xu, J. K. Kim, E. F. Schubert, M. H. Kim, S. Yoon, S. M. Lee, C. Sone, T. Sakong, and Y. Park, "Polarization-Matched GaInN/AlGaInN Multi-Quantum-Well Light-Emitting Diodes with Reduced Efficiency Droop," *Applied Physics Letters***,** vol. 93, no. 4, pp. 041102-3, 2008.

[98] Y. C. Shen, G. O. Mueller, S. Watanabe, N. F. Gardner, A. Munkholm, and M. R. Krames, "Auger Recombination in InGaN Measured by Photoluminescence," *Applied Physics Letters***,** vol. 91, no. 14, pp. 141101-3, 2007.

[99] M. Zhang, P. Bhattacharya, J. Singh, and J. Hinckley, "Direct Measurement of Auger Recombination in $In_{0.1}Ga_{0.9}N$/GaN Quantum Wells and Its Impact on the Efficiency of $In_{0.1}Ga_{0.9}N$/GaN Multiple Quantum Well Light Emitting Diodes,", *Applied Physics Letters***,** vol. 95, no. 20, pp. 201108-3, 2009.

[100] J. Q. Xie, X. F. Ni, Q. Fan, R. Shimada, U. Ozgur, and H. Morkoc, "On the Efficiency Droop in InGaN Multiple Quantum Well Blue Light Emitting Diodes and Its Reduction with p-Doped Quantum Well Barriers,"*Applied Physics Letters***,** vol. 93, no. 12, pp. 121107-3, 2008.

[101] B. Monemar and B. E. Sernelius, "Defect Related Issues in the "Current Roll-Off" in InGaN Based Light Emitting Diodes," *Applied Physics Letters***,** vol. 91, no. 18, pp. 181103-3, 2007.

[102] Y. Yang, X. A. Cao, and C. H. Yan, "Investigation of the Nonthermal Mechanism of Efficiency Rolloff in InGaN Light-Emitting Diodes," *IEEE Transactions on Electron Devices*, vol. 55, no. 7, pp. 1771-1775, 2008.

[103] U. Ozgur, X. Ni, X. Li, J. Lee, S. Liu, S. Okur, V. Avrutin, A. Matulionis, and H. Morkoc, "Ballistic Transport in InGaN-based LEDs: Impact on Efficiency," *Semiconductor Science and Technology*, vol. 26, no. 1, pp. 014022(1-12), 2011.

[104] X. Ni, X. Li, J. Lee, S. Liu, V. Avrutin, U. Ozgur, H. Morkoc, A. Matulionis, T. Paskova, G. Mulholland, and K. R. Evans, "InGaN Staircase Electron Injector for Reduction of Electron Overflow in InGaN Light Emitting Diodes," *Applied Physics Letters*, vol. 97, no. 3, pp. 031110-3, 2010.

[105] K. J. Vampola, M. Iza, S. Keller, S. P. DenBaars, and S. Nakamura, "Measurement of Electron Overflow in 450 nm InGaN Light-Emitting Diode Structures," *Applied Physics Letters*, vol. 94, no. 6, pp. 061116-3, 2009.

[106] Z. Gong, S. Jin, Y. Chen, J. McKendry, D. Massoubre, I. M. Watson, E. Gu, and M. D. Dawson, "Size-Dependent Light Output, Spectral Shift, and Self-Heating of 400 nm InGaN Light-Emitting Diodes," *Journal of Applied Physics*, vol. 107, no. 1, pp. 013103-013106, 2010.

[107] T. Kim, Y. H. Jung, J. Song, D. Kim, Y. Li, H.-s. Kim, I.-S. Song, J. J. Wierer, H. A. Pao, Y. Huang, and J. A. Rogers, "High-Efficiency, Microscale GAN Light-Emitting Diodes and Their Thermal Properties on Unusual Substrates," *Small*, vol. 8, no. 11, pp. 1643-1649, 2012.

[108] D. S. Meyaard, Q. Shan, J. Cho, E. F. Schubert, S.-H. Han, M.-H. Kim, C. Sone, S. J. Oh, and J. K. Kim, "Temperature Dependent Efficiency Droop in GaInN Light-Emitting Diodes with Different Current Densities," *Applied Physics Letters*, vol. 100, no. 8, pp. 081106-3, 2012.

[109] T. Wu, C.-W. Sher, Y. Lin, C.-F. Lee, S. Liang, Y. Lu, S.-W. H. Chen, W. Guo, H.-C. Kuo, and Z. Chen, "Mini-LED and Micro-LED: Promising Candidates for the Next Generation Display Technology," *Applied Sciences*, vol. 8, no. 9, pp. 1557(1-17), 2018.

[110] S. X. Jin, J. Li, J. Z. Li, J. Y. Lin, and H. X. Jiang, "GaN microdisk light emitting diodes," *Applied Physics Letters*, vol. 76, no. 5, pp. 631-633, 2000.

[111] H. X. Jiang, S. X. Jin, J. Li, J. Shakya, and J. Y. Lin, "III-nitride blue microdisplays," *Applied Physics Letters*, vol. 78, no. 9, pp. 1303-1305, 2001.

[112] C. H. Lin, C. F. Lee, A. Verma, H. Y. Lin, C. C. Lin, C. W. Sher, and H. C. Kuo, "A Full-color Micro-light-emitting-diode Display by a Lithographic-fabricated Photoresist Mold," in SID Symposium Digest of Technical Papers, vol, 49, no. 1, pp. 779-781, 2018.

[113] C. M. Kang, D. J. Kong, J. P. Shim, S. Kim, S. B. Choi, J. Y. Lee, J. H. Min, D. J. Seo, S. Y. Choi, and D. S. Lee, "Fabrication of a vertically-stacked passive-matrix micro-LED array structure for a dual color display," *Optics Express*, vol. 25, no. 3, pp. 2489-2495, 2017.

[114] F. Olivier, S. Tirano, L. Dupré, B. Aventurier, C. Largeron, and F. Templier, "Influence of size-reduction on the performances of GaN-based micro-LEDs for display application," *Journal of Luminescence*, vol. 191, pp. 112-116, 2017.

[115] H. P. T. Nguyen, M. Djavid, S. Y. Woo, X. Liu, A. T. Connie, S. Sadaf, Q. Wang, G. A. Botton, I. Shih, and Z. Mi, "Engineering the Carrier Dynamics of InGaN Nanowire White Light-Emitting Diodes by Distributed p-AlGaN Electron Blocking Layers," *Scietific Reports***,** vol. 5, no. 1, pp. 1-7, 2014.

[116] M. Tchernycheva, V. Neplokh, H. Zhang, P. Lavenus, L. Rigutti, F. Bayle, F. H. Julien, A. Babichev, G. Jacopin, L. Largeau, R. Ciechonski, G. Vescovi, and O. Kryliouk, "Core-Shell InGaN/GaN Nanowire Light Emitting Diodes Analyzed by Electron Beam Induced Current Microscopy and Cathodoluminescence Mapping," *Nanoscale***,** vol. 7, no. 27, pp. 11692-11701, 2015.

[117] H. P. T. Nguyen, M. Djavid, S. Y. Woo, X. Liu, Q. Wang, G. A. Botton, and Z. Mi, "High-Power Phosphor-Free InGaN/AlGaN Dot-in-a-wire Core-Shell White Light-Emitting Diodes," *in Proceeding of SPIE Conference, the Light-Emitting Diodes: Materials, Devices, and Applications for Solid State Lighting XIX*, vol. 9383, San Diego, CA, USA, 9-13 August, 2015, pp. 938307-8.

[118] H. P. T. Nguyen. Z. Mi, M. Djavid, S. Zhang, A. T. Connie, S. M. Sadaf, Q. Wang, S. Zhao, and I. Shih, "High Power Phosphor-Free InGaNGaNAlGaN Core-Shell Nanowire White Light Emitting Diodes on Si Substrates," *ECS Transactions***,** vol. 61, no. 5, pp. 9-15, 2014.

[119] M. R. Philip, D. D. Choudhary, M. Djavid, K. Q. Le, J. Piao, and H. P. T. Nguyen, "High Efficiency Green/Yellow and Red InGaN/AlGaN Nanowire Light-Emitting Diodes Grown by Molecular Beam Epitaxy," *Journal of Science: Advanced Materials and Devices***,** vol. 2, no. 2, pp. 150-155, 2017.

[120] M. R. Philip, T. H. Q. Bui, D. D. Choudhary, M. Djavid, P. Vu, T. T. Pham, H.-D. Nguyen, H. P. T Nguyen, "Molecular Beam Epitaxial Growth and Device Characterization of AlGaN UV-B Nanowire Light-Emitting Diodes," *Journal of Advanced Optics and P hotonics***,** vol. 1, no. 1, pp. 1-11, 2018.

[121] H. P. Nguyen, S. Zhang, A. T. Connie, M. G. Kibria, Q. Wang, I. Shih, and Z. Mi, "Breaking the Carrier Injection Bottleneck of Phosphor-Free Nanowire White Light-Emitting Diodes," *Nano Letters***,** vol. 13, no. 11, pp. 5437-5442, 2013.

[122] H. P. T. Nguyen, M. Djavid, and Z. Mi, "Nonradiative Recombination Mechanism in Phosphor-Free GaN-Based Nanowire White Light Emitting Diodes and the

Effect of Ammonium Sulfide Surface Passivation," *ECS Transactions***,** vol. 53, no. 2, pp. 93-100, 2013.

[123] T.Takeuchi, S. Sota1, M. Katsuragawa, M. Komori1, H. Takeuchi, H. Amano H. Amano, and I. A. I. Akasaki, "Quantum-Confined Stark Effect due to Piezoelectric Fields in GaInN Strained Quantum Wells," *Japanese Journal of Applied Physics*, vol. 36, no. 4A, pp. L382-L385, 1997.

[124] J. Piprek, "Efficiency Droop in Nitride-Based Light-Emitting Diodes," *Physica Status Solidi (a)***,** vol. 207, no. 10, pp. 2217-2225, 2010.

[125] X.-F. Wang, Q. Yang, G.-G. Wang, X.-Z. Wang, and J.-C. Han, "A New Single-Component $KCaY(PO_4)_2:Dy^{3+}$, Eu^{3+} Nanosized Phosphor with High Color-Rendering Index and Excellent Thermal Resistance for Warm-White NUV-LED," *RSC Advances***,** vol. 6, no. 98, pp. 96263-96274, 2016.

[126] T. W. Kuo, W.-R. Liu, and T. M. Chen "High Color Rendering White Light-Emitting-Diode Illuminator Using the Red-Emitting Eu^{2+}-activated CaZnOS Phosphors Excited by Blue LED," *Optics Express***,** vol. 18, pp. 8187-8192, 2010.

[127] N. D. Quoc Anh, H.-Y. Lee, T. Thanh Phuong, N. H. Khanh Nhan, T. H. Quang Minh, and T. Huu Ly, "$Y_2O_3:Eu^{3+}$ Phosphor: A Novel Solution for An Increase in Color Rendering Index of Multi-Chip White LED Packages," *Journal of the Chinese Institute of Engineers***,** vol. 40, no. 3, pp. 228-234, 2017.

[128] S. Nizamoglu, G. Zengin, and H. V. Demir, "Color-Converting Combinations of Nanocrystal Emitters for Warm-White Light Generation with High Color Rendering Index," *Applied Physics Letters***,** vol. 92, no. 3, pp. 031102-3, 2008.

[129] L. Y. Chen, J. K. Chang, W. C. Cheng, J. C. Huang, Y. C. Huang, and W. H. Cheng, "Chromaticity Tailorable Glass-Based Phosphor-Converted White Light-Emitting Diodes with High Color Rendering Index," *Optics Express***,** vol. 23, no. 15, pp. A1024-1029, 2015.

[130] C. H. Huang and T. M. Chen, "Novel Yellow-Emitting $Sr_8MgLn(PO_4)_7:Eu^{2+}$ (Ln=Y, La) Phosphors for Applications in White LEDs With Excellent Color Rendering Index," *Inorgnic Chemistry***,** vol. 50, no. 12, pp. 5725-5730, 2011.

[131] N. H. Alvi, S. M. Usman Ali, S. Hussain, O. Nur, and M. Willander, "Fabrication and Comparative Optical Characterization of n-ZnO Nanostructures (Nanowalls, Nanorods, Nanoflowers and Nanotubes)/p-GaN White-Light-Emitting Diodes," *Scripta Materialia***,** vol. 64, no. 8, pp. 697-700, 2011.

[132] M. H. Fang, C. Ni, X. Zhang, Y. T. Tsai, S. Mahlik, A. Lazarowska, M. Grinberg, H. S. Sheu, J. F. Lee, B. M. Cheng, and R. S. Liu, "Enhance Color Rendering Index via Full Spectrum Employing the Important Key of Cyan Phosphor," *ACS Appllied Materials & Interfaces***,** vol. 8, no. 45, pp. 30677-30682, 2016.

[133] Z. Wang, F. Yuan, X. Li, Y. Li, H. Zhong, L. Fan, and S. Yang, "53% Efficient Red Emissive Carbon Quantum Dots for High Color Rendering and Stable Warm White-Light-Emitting Diodes," *Advanced Materials***,** vol. 29, no. 37, pp. 170291(1-7), 2017.

[134] M. Raeiszadeh and B. Adeli, "A Critical Review on Ultraviolet Disinfection Systems Against COVID-19 Outbreak: Applicability, Validation, and Safety Considerations," *ACS Photonics***,** vol. 7, no. 11, pp. 2941-2951, 2020.

[135] H.Y. Ryu, I. G. Choi, H. S. Choi, and J. Shim, "Investigation of Light Extraction Efficiency in AlGaN Deep-Ultraviolet Light-Emitting Diodes," *Applied Physics Express*, vol. 6, no. 6, pp. 062101-4, 2013 .

[136] A. Cosentino, "Practical Notes on Ultraviolet Technical Photography for Art Examination," *Conservar Património***,** vol. 21, pp. 53-62, 2015.

[137] T. A. Kalajian, A. Aldoukhi, A. J. Veronikis, K. Persons, and M. F. Holick, "Ultraviolet B Light Emitting Diodes (LEDs) Are More Efficient and Effective in Producing Vitamin D3 in Human Skin Compared to Natural Sunlight," *Scientific Reports***,** vol. 7, no. 1, pp. 1-8, 2017.

[138] A. Reich and K. Medrek, "Effects of Narrow Band UVB (311 nm) Irradiation on Epidermal Cells," *International Journal of Molecular Sciences***,** vol. 14, no. 4, pp. 8456-8466, 2013.

[139] K.-H. Lee and T.-H. Park, "Image Segmentation of UV Pattern for Automatic Paper-Money Inspection," in the 11th International Conference on Control Automation Robotics & Vision Singapore, 2010, pp. 1175-1180.

[140] M. T. Chen, M. P. Lu, Y. J. Wu, J. Song, C. Y. Lee, M. Y. Lu, Y. C. Chang, L. J. Chou, Z. L. Wang, and L. J. Chen, "Near UV LEDs Made with in situ Doped p-n Homojunction ZnO Nanowire Arrays," *Nano Letters***,** vol. 10, no. 11, pp. 4387-4393, 2010.

[141] C. Coughlan, S. Schulz, M. A. Caro, and E. P. O'Reilly, "Band Gap Bowing and Optical Polarization Switching in AlGaN alloys," *Physica Status Solidi (b)***,** vol. 252, no. 5, pp. 879-884, 2015.

[142] M. Kneissl, T.-Y. Seong, J. Han, and H. Amano, "The Emergence and Prospects of Deep-Ultraviolet Light-Emitting Diode Technologies," *Nature Photonics***,** vol. 13, no. 4, pp. 233-244, 2019.

[143] J. Cho, E. F. Schubert, and J. K. Kim, "Efficiency Droop in Light-Emitting Diodes: Challenges and Countermeasures," *Laser & Photonics Reviews***,** vol. 7, no. 3, pp. 408-421, 2013.

[144] M. Yamada., T. Mitani, Y. Narukawa, S. Shioji, I. Niki, S.Sonobe1, K. Deguchi, M. Sano, and T.Mukai, "InGaN-Based Near-Ultraviolet and Blue-Light-Emitting

Diodes with High External Quantum Efficiency Using a Patterned Sapphire Substrate and A Mesh Electrode," *Journal of Advanced Optics And Photonics,* vol. 41, no. 12B, pp. L1431-L1433, 2002.

[145] M. Djavid, X. Liu, and Z.Mi, "Improvement of the Light Extraction Efficiency of GaN-Based LEDs Using Rolled-Up Nanotube Arrays," *Optics Express,* vol. 22, no. S7, pp. A1680-A1686, 2014.

[146] C. E. Lee, B. S. Cheng, Y. C. Lee, H. C. Kuo, T. C. Lu, and S. C. Wang, "Output Power Enhancement of Vertical-Injection Ultraviolet Light-Emitting Diodes by GaN-Free and Surface Roughness Structures," *Electrochemical and Solid-State Letters,* vol. 12, no. 2, pp. H44-H46, 2009.

[147] J. Shakya, K. H. Kim, J. Y. Lin, and H. X. Jiang, "Enhanced Light Extraction in III-Nitride Ultraviolet Photonic Crystal Light-Emitting Diodes," *Applied Physics Letters,* vol. 85, no. 1, pp. 142-144, 2004.

[148] M. Djavid and Z. Mi, "Enhancing the Light Extraction Efficiency of AlGaN Deep Ultraviolet Light Emitting Diodes by Using Nanowire Structures," *Applied Physics Letters,* vol. 108, no. 5, 2016.

[149] J. P. Berenger, "Evanescent Waves in PML's Origin of the Numerical Reflection in Wave-Structure Interaction Problems," *IEEE Transactions on Antennas and Propagation.* vol. 47, no. 10, 1497-1503, 1999.

[150] Y. Liu, C. D. Sarris, "AMR-FDTD: A Dynamically Adaptive Mesh Refinement Scheme for the Finite-Difference Time-Domain Technique," *Proceedings of IEEE Antennas and Propagation Society International Symposium. 1A,* 2005, pp. 134–137.

[151] J. Zhang, S. Wu, S. Rai, V. Mandavilli, V. Adivarahan, A. Chitnis, M. Shatalov, and M. A. Khan, "AlGaN Multiple-Quantum-Well-Based, Deep Ultraviolet Light-Emitting Diodes with Significantly Reduced Long-Wave Emission," *Applied Physics Letters,* vol. 83, no. 17, pp. 3456-3458, 2003.

[152] K. X. Chen, Y. A. Xi, F. W. Mont, J. K. Kim, E. F. Schubert, W. Liu, X. Li, and J. A. Smart, "Recombination Dynamics in Ultraviolet Light-Emitting Diodes with Si-Doped $Al_xGa_{1-x}N/Al_yGa1_{-y}N$ Multiple Quantum Well Active Regions," *Journal of Applied Physics,* vol. 101, no. 11, pp. 113102-5, 2007.

[153] B. Jain, R. T. Velpula, H. Q. T. Bui, H. D. Nguyen, T. R. Lenka, T. K. Nguyen, and H. P. T. Nguyen, "High Performance Electron Blocking Layer-Free InGaN/GaN Nanowire White-Light-Emitting Diodes," *Optics Express,* vol. 28, no. 1, pp. 665-675, 2020.

[154] N. B. Eric and H. Virey, "Status and Prospects of MicroLED Displays," *the Society for Information Display,* vol. 45, no.1, pp. 593-596, 2018.

[155] N. Yeh and J.-P. Chung, "High-Brightness LEDs—Energy Efficient Lighting Sources and Their Potential in Indoor Plant Cultivation," *Renewable and Sustainable Energy Reviews,* vol. 13, no. 8, pp. 2175-2180, 2009.

[156] K. Song, M. Mohseni, and F. Taghipour, "Application of Ultraviolet Light-Emitting Diodes (UV-LEDs) for Water Disinfection: A Review," *Water Research,* vol. 94, pp. 341-349, 2016.

[157] W.-S. Won, L. G. Tran, W.-T. Park, K.-K. Kim, C. S. Shin, N. Kim, Y.-J. Kim, and Y.-J. Yoon, "UV-LEDs for the Disinfection and Bio-Sensing Applications," *International Journal of Precision Engineering and Manufacturing,* vol. 19, no. 12, pp. 1901-1915, 2018.

[158] M. Kneissl, T. Kolbe, C. Chua, V. Kueller, N. Lobo, J. Stellmach, A. Knauer, H. Rodriguez, S. Einfeldt, Z. Yang, N. M. Johnson, and M. Weyers, "Advances in Group III-Nitride-Based Deep UV Light-Emitting Diode Technology," *Semiconductor Science and Technology,* vol. 26, no. 1, pp. 014036-6. 2011.

[159] K. Uesugi, Y. Hayashi, K. Shojiki, and H. Miyake, "Reduction of Threading Dislocation Density and Suppression of Cracking in Sputter-Deposited AlN Templates Annealed at High Temperatures," *Applied Physics Express,* vol. 12, no. 6, pp. 065501-4, 2019.

[160] H. Hirayama, S. Fujikawa, and N. Kamata, "Recent Progress in AlGaN-Based Deep-UV LEDs," *Electronics and Communications in Japan,* vol. 98, no. 5, pp. 1-8, 2015.

[161] R. H. Horng, W. K. Wang, S. C. Huang, S. Y. Huang, S. H. Lin, C. F. Lin, and D. S. Wuu, "Growth and Characterization of 380-nm InGaN/AlGaN LEDs Grown on Patterned Sapphire Substrates," *Journal of Crystal Growth,* vol. 298, pp. 219-222, 2007.

[162] T. K. John E. Ayers, Paul Rago, Johanna Raphael, "Metamorphic Devices" in *Heteroepitaxy of Semiconductors*: *Theory, Growth, and Characterization*. CRC Press, 2017, ch.9, p.576.

[163] M. R. Krames, O. B. Shchekin, R. Mueller-Mach, G. O. Mueller, L. Zhou, G. Harbers, and M. G. Craford, "Status and Future of High-Power Light-Emitting Diodes for Solid-State Lighting," *Journal of Display Technology,* vol. 3, no. 2, pp. 160-175, 2007.

[164] O. Ambacher, "Growth and Applications of Group III-Nitrides," *Journal of Physics D: Applied Physics,* vol. 31, pp. 2653–2710, 1998.

[165] M. L. Nakarmi, K. H. Kim, M. Khizar, Z. Y. Fan, J. Y. Lin, and H. X. Jiang, "Electrical and Optical Properties of Mg-Doped $Al_{0.7}Ga_{0.3}N$ Alloys," *Applied Physics Letters,* vol. 86, no. 9, pp. 092108-3, 2005.

[166] X. Wang, W. Wang, J. Wang, H. Wu, and C. Liu, "Experimental Evidences for Reducing Mg Activation Energy in High Al-Content AlGaN Alloy by Mg_{Ga} δ Doping in $(AlN)_m/(GaN)_n$ Superlattice," *Scietific Reports***,** vol. 7, no. 1, pp. 1-6, 2017.

[167] Y. Chen, H. Wu, E. Han, G. Yue, Z. Chen, Z. Wu, G. Wang, and H. Jiang, "High Hole Concentration in p-Type AlGaN by Indium-Surfactant-Assisted Mg-Delta Doping," *Applied Physics Letters***,** vol. 106, no. 16, pp. 2015.

[168] K. Ban, J. Yamamoto, K. Takeda, K. Ide, M. Iwaya, T. Takeuchi, S. Kamiyama, I. Akasaki, and H. Amano, "Internal Quantum Efficiency of Whole-Composition-Range AlGaN Multiquantum Wells," *Applied Physics Express***,** vol. 4, no. 5, pp. 052101-3, 2011.

[169] K. B. Nam, J. Li, M. L. Nakarmi, J. Y. Lin, and H. X. Jiang, "Unique Optical Properties of AlGaN Alloys and Related Ultraviolet Emitters," *Applied Physics Letters*, vol. 84, no. 25, pp. 5264-5266, 2004.

[170] T. Kolbe, A. Knauer, C. Chua, Z. Yang, S. Einfeldt, P. Vogt, N. M. Johnson, M. Weyers, and M. Kneissl, "Optical Polarization Characteristics of Ultraviolet (In)(Al)GaN Multiple Quantum Well Light Emitting Diodes," *Applied Physics Letters*, vol. 97, no. 17, pp. 171105-3, 2010.

[171] B. T. Tran and H. Hirayama, "Growth and Fabrication of High External Quantum Efficiency AlGaN-Based Deep Ultraviolet Light-Emitting Diode Grown on Pattern Si substrate," *Scietific Reports***,** vol. 7, no. 1, pp. 1-6, 2017.

[172] B. T. Tran, N. Maeda, M. Jo, D. Inoue, T. Kikitsu, and H. Hirayama, "Performance Improvement of AlN Crystal Quality Grown on Patterned Si(111) Substrate for Deep UV-LED Applications," *Scietific Reports***,** vol. 6, no. 1, pp. 1-6, 2016.

[173] J. Li, J. Wang, Y. Zhang, J. Yan, and Y. Guo, "Enhancing the Light Extraction of AlGaN-Based Ultraviolet Light-Emitting Diodes in the Nanoscale," *Journal of Nanophotonics***,** vol. 12, no. 4, pp. 043510-12, 2018.

[174] F. H. Fan, Z. Y. Syu, C. J. Wu, Z. J. Yang, B. S. Huang, G. J. Wang, Y. S. Lin, H. Chen, C. Hauer Kao, and C. F. Lin, "Ultraviolet GaN Light-Emitting Diodes with Porous-AlGaN Reflectors," *Scietific Reports***,** vol. 7, no. 1, pp.1-6, 2017.

[175] H. Hirayama, T. Takano, J. Sakai, T. Mino, K. Tsubaki, N. Maeda, M. Jo, I. Ohshima, T. Matsumoto, N. Kamata, ""Over 10% EQE AlGaN Deep-UV LED Using Transparent p-AlGaN Contact Layer," *in Proceedings of SPIE 10104, Gallium Nitride Materials and Devices XII*, vol. 101041P, San Francisco, CA, USA, 28 January-2 Febuary, 2017, pp. 101041P.

[176] Z. H. Zhang, C. Chu, K. Tian, and Y. Zhang, *Deep Ultraviolet LEDs Understanding the Low External Quantum Efficiency*. Singapore, Springer, 2019.

[177] Y. Nagasawa and A. Hirano, "A Review of AlGaN-Based Deep-Ultraviolet Light-Emitting Diodes on Sapphire," *Applied Sciences***,** vol. 8, no. 8, pp. 1264(1-36), 2018.

[178] N. Maeda and H. Hirayama, "Realization of High-Efficiency Deep-UV LEDs Using Transparent p-AlGaN Contact Layer," *Physica Status Solidi (c)***,** vol. 10, no. 11, pp. 1521-1524, 2013.

[179] C. Zhao, N. Alfaraj, R. Chandra Subedi, J. W. Liang, A. A. Alatawi, A. A. Alhamoud, M. Ebaid, M. S. Alias, T. K. Ng, and B. S. Ooi, "III-Nitride Nanowires on Unconventional Substrates: From Materials to Optoelectronic Device Applications," *Progress in Quantum Electronics***,** vol. 61, pp. 1-31, 2018.

[180] Y. K. Ooi, "Light Extraction Efficiency of Nanostructured III-Nitride Light-Emitting diodes," Ph.D Desertation, Department of Electrical and Microelectron. Engineering, RIT, Rochester, NY, 2019.

[181] Y. K. Ooi, C. Liu, and J. Zhang, "Analysis of Polarization-Dependent Light Extraction and Effect of Passivation Layer for 230-nm AlGaN Nanowire Light-Emitting Diodes," *IEEE Photonics Journal***,** vol. 9, no. 4, pp. 1-12, 2017.

[182] D. Q. Fang, A. L. Rosa, T. Frauenheim, and R. Q. Zhang, "Band Gap Engineering of GaN Nanowires by Surface Functionalization," *Applied Physics Letters***,** vol. 94, no. 7, pp. 073116-3, 2009.

[183] M. Speckbacher, J. Treu, T. J. Whittles, W. M. Linhart, X. Xu, K. Saller, V. R. Dhanak, G. Abstreiter, J. J. Finley, T. D. Veal, and G. Koblmuller, "Direct Measurements of Fermi Level Pinning at the Surface of Intrinsically n-Type InGaAs Nanowires," *Nano Letters***,** vol. 16, no. 8, pp. 5135-5142, 2016.

[184] B. K. Li, M. J. Wang, K. J. Chen, and J. N. Wang, "Fermi-Level Depinning and Hole Injection Induced Two-Dimensional Electron Related Radiative Emissions from A Forward Biased Ni/Au-AlGaN/GaN Schottky Diode," *Applied Physics Letters***,** vol. 95, no. 23, pp. 232111-3, 2009.

[185] A. Armstrong, Q. Li, Y. Lin, A. A. Talin, and G. T. Wang, "GaN Nanowire Surface State Observed Using Deep Level Optical Spectroscopy," *Applied Physics Letters***,** vol. 96, no. 16, pp. 163106-3, 2010.

[186] S. L. Chen, W. M. Chen, F. Ishikawa, and I. A. Buyanova, "Suppression of Non-Radiative Surface Recombination by N Incorporation in GaAs/GaNAs Core/Shell Nanowires," *Scientific Reports***,** vol. 5, no. 1, pp. 1-9, 2015.

[187] S. A. Chevtchenko, M. A. Reshchikov, Q. Fan, X. Ni, Y. T. Moon, A. A. Baski, and H. Morkoç, "Study of SiN_x and SiO_2 Passivation of GaN Surfaces," *Journal of Applied Physics***,** vol. 101, no. 11, pp. 113709-7, 2007.

[188] T. Hashizume, S. Ootomo, S. Oyama, M. Konishi, and H. Hasegawa, "Chemistry and Electrical Properties of Surfaces of GaN and GaN/AlGaN Heterostructures," *Journal of Vacuum Science & Technology B: Microelectronics and Nanometer Structures***,** vol. 19, no. 4, pp. 1675-1681, 2001.

[189] M. Meneghinil, L.R. Trevisanello, R. Penzol, M. Benedetti, U.Zehnder, U. Strauss, G. Meneghesso, and E. Zanoni, "Reversible Degradation of GaN LEDs Related to Passivation," *in Proceedings, the 45th Annual IEEE International Reliability Physics Symposium*, 15 Apr. 2007, pp. 457-461.

[190] M. Meneghini, L. R. Trevisanello, S. Levada, Meneghesso G, Tamiazzo G, Zanoni E, T. Zahner, U. Zehnder, V. Harle, U. Straus, "Failure Mechanisms of Gallium Nitride LEDs Related with Passivation," in *International Electron Devices Meeting. IEDM Technical Digest, 2005.* pp. 4-pp.

[191] Y.-Y. H. L. Y. Chen, C. H. Chang, Y.-H. Sun, Y. W. Cheng, M. Y. Ke, C. P. Chen, and J Huang, "High Performance InGaN/GaN Nanorod Light Emitting Diode Arrays Fabricated by Nanosphere Lithography and Chemical Mechanical Polishing Processes," *Optics Express***,** vol. 18, no. 8, pp. 7664-7669, 2010.

[192] O. Brandt, C. Pfüller, C. Chèze, L. Geelhaar, and H. Riechert, "Sub-meV Linewidth of Excitonic Luminescence in Single GaN Nanowires: Direct Evidence for Surface Excitons," *Physical Review B***,** vol. 81, no. 4, pp. 045302-7. 2010.

[193] A. Waag, X. Wang, S. Fündling, J. Ledig, M. Erenburg, R. Neumann, M. Al Suleiman, S. Merzsch, J. Wei, S. Li, H. H. Wehmann, W. Bergbauer, M. Straßburg, A. Trampert, U. Jahn, and H. Riechert, "The nanorod approach: GaN NanoLEDs for solid state lighting," *Physica Status Solidi (c)***,** vol. 8, no. 7-8, pp. 2296-2301, 2011.

[194] M. Biswas, V. Chavan, S. Zhao, Z. Mi, and S. Chakrabarti, "Passivation of Surface States of AlGaN Nanowires Using H_3PO_4 Treatment to Enhance the Performance of UV-LEDs and Photoanodes," *ACS Applied Nano Materials***,** vol. 1, no. 4, pp. 1968-1975, 2018.

[195] Q. Wang, H. P. T. Nguyen, K. Cui, and Z. Mi, "High Efficiency Ultraviolet Emission from $Al_xGa_{1-x}N$ Core-Shell Nanowire Heterostructures Grown on Si (111) by Molecular Beam Epitaxy," *Applied Physics Letters***,** vol. 101, no. 4, pp. 043115-4, 2012.

[196] M. Hartensveld, G. Ouin, C. Liu, and J. Zhang, "Effect of KOH Passivation for Top-Down Fabricated InGaN Nanowire Light Emitting Diodes," *Journal of Applied Physics***,** vol. 126, no. 18, pp. 183102-6, 2019.

[197] H. Oigawa, J. F. Fan, Y. Nannichi, H. Sugahara, and M. Oshima, "Universal Passivation Effect of $(NH_4)_2S_x$ Treatment on the Surface of III-V Compound Semiconductors," *Japanese journal of applied physics***,** vol. 30, no. 3A, pp. L322-L325, 1991.

[198] Q. Wang, A. T. Connie, H. P. Nguyen, M. G. Kibria, S. Zhao, S. Sharif, I. Shih, and Z. Mi, "Highly Efficient, Spectrally Pure 340 nm Ultraviolet Emission from $Al_xGa_{(1-x)}N$ Nanowire Based Light Emitting Diodes," *Nanotechnology***,** vol. 24, no. 34, pp. 345201-6, 2013.

[199] J. C. Zhang, Y. H. Zhu, T. Egawa, S. Sumiya, M. Miyoshi, and M. Tanaka, "Suppression of the Subband Parasitic Peak by 1 nm *i*-AlN Interlayer in AlGaN Deep Ultraviolet Light-Emitting Diodes," *Applied Physics Letters***,** vol. 93, no. 13, pp. 131117, 2008.

[200] G. L. Martinez, M. R. Curiel, B. J. Skromme & R. J. Molnar, "Surface Recombination and Sulfide Passivation of GaN," *Journal of Electronic Materials***,** vol. 29, pp. 325–331, 2000.

[201] M. H. Sun, H. J. Joyce, Q. Gao, H. H. Tan, C. Jagadish, and C. Z. Ning, "Removal of Surface States and Recovery of Band-Edge Emission in InAs Nanowires Through Surface Passivation," *Nano Letters***,** vol. 12, no. 7, pp. 3378-3384, 2012.

[202] H. Sun, M. K. Shakfa, M. M. Muhammed, B. Janjua, K.-H. Li, R. Lin, T. K. Ng, I. S. Roqan, B. S. Ooi, and X. Li, "Surface-Passivated AlGaN Nanowires for Enhanced Luminescence of Ultraviolet Light Emitting Diodes," *ACS Photonics***,** vol. 5, no. 3, pp. 964-970, 2017.

[203] X. Liu, Y. Mou, H. Wang, R. Liang, X. Wang, Y. Peng, and M. Chen, "Enhanced Light Extraction of Deep Ultraviolet Light-Emitting Diodes by Using Optimized Aluminum Reflector," *Applied Optices*, vol. 57, no. 25, pp. 7325-7328, 2018.

[204] H. Q. T. Bui, R. T. Velpula, B. Jian, M. R. Philip, H. D. Tong, T. R. Lenka, and H. P. T. Nguyen, "High-Performance Nanowire Ultraviolet Light-Emitting Diodes with Potassium Hydroxide and Ammonium Sulfide Surface Passivation," *Applied Optics*, vol. 59, no. 24, pp. 7352-7356, 2020.

[205] S. L. Upstone, "Ultraviolet/Visible Light Absorption Spectrophotometry in Clinical Chemistry," in *Encyclopedia of Analytical Chemistry: Applications, Theory and Instrumentation*. Hoboken, NJ, Wiley, 2006.

[206] J. B. Gillespie, M. Maclean, M. J. Given, M. P. Wilson, M. D. Judd, I. V. Timoshkin, and S. J. MacGregor, "Efficacy of Pulsed 405-nm Light-Emitting Diodes for Antimicrobial Photodynamic Inactivation: Effects of Intensity, Frequency, and Duty Cycle," *Photomedicine and Laser Surgery*, vol. 35, no. 3, pp. 150-156, 2016.

[207] M. Zhao, H. Liao, M. S. Molokeev, Y. Zhou, Q. Zhang, Q. Liu, and Z. Xia, "Emerging Ultra-Narrow-Band Cyan-Emitting Phosphor for White LEDs with Enhanced Color Rendition," *Light: Science & Applications*, vol. 8, no. 1, pp. 1-9, 2019.

[208] J. L. Leaño, M.-H. Fang, and R.-S. Liu, "Critical Review—Narrow-Band Emission of Nitride Phosphors for Light-Emitting Diodes: Perspectives and Opportunities," *ECS Journal of Solid State Science and Technology*, vol. 7, no. 1, pp. R3111-R3133, 2017.

[209] H. A. Macleod, *Thin-Film Optical Filters*. Boca Raton, FL, USA, CRC press, 2017.

[210] A. Perot and C. Fabry, "On the Application of Interference Phenomena to the Solution of Various Problems of Spectroscopy and Metrology," *Astrophysical Journal*, vol. 9, no. 87, 1899.

[211] J. Hennessy, A. D. Jewell, M. E. Hoenk, and S. Nikzad, "Metal-Dielectric Filters for Solar-Blind Silicon Ultraviolet Detectors," *Applied Optics*, vol. 54, no. 11, pp. 3507-3512, 2015

[212] J. Mu, P.-T. Lin, L. Zhang, J. Michel, L. C. Kimerling, F. Jaworski, and A. Agarwal, "Design and Fabrication of a High Transmissivity Metal-Dielectric Ultraviolet Band-Pass Filter," *Applied Physics Letters*, vol. 102, no. 21, 2013

[213] N. A. Repina, A. Rosenbloom, A. Mukherjee, D. V. Schaffer, and R. S. Kane, "At Light Speed: Advances in Optogenetic Systems for Regulating Cell Signaling and Behavior," *Annual Review of Chemical and Biomolecular Engineering*, vol. 8, pp. 13-39, 2017.

[214] A. S. Chuong, M. L. Miri, V. Busskamp, G. A. Matthews, L. C. Acker, A. T. Sorensen, A. Young, N. C. Klapoetke, M. A. Henninger, S. B. Kodandaramaiah, M. Ogawa, S. B. Ramanlal, R. C. Bandler, B. D. Allen, C. R. Forest, B. Y. Chow, X. Han, Y. Lin, K. M. Tye, B. Roska, J. A. Cardin, and E. S. Boyden, "Noninvasive Optical Inhibition with A Red-Shifted Microbial Rhodopsin," *Nature Neuroscience*, vol. 17, no. 8, pp. 1123-1129, 2014.

[215] E. S. Boyden, "A History of Optogenetics: The Development of Tools for Controlling Brain Circuits with Light," *F1000 Biology Report*, vol. 3, pp. 1-12, 2011.

[216] A. Krishnarao, *Optogenetics: From Neuronal Function to Mapping and Disease Biology*. Cambridge University Press, 2017.

[217] K Y. Kwon, H.-M. Lee, M. Ghovanloo, A.Weber, and W. Li, "A Wireless Slanted Optrode Array with Integrated Micro LEDs for Optogenetics," *in Proceeding of the IEEE 27th International Conference on Micro Electro Mechanical Systems (MEMS)*, San Francisco, CA, USA, January 26-30, 2014, pp. 813-816.

[218] G. Shin, A. M. Gomez, R. Al-Hasani, Y. R. Jeong, J. Kim, Z. Xie, A. Banks, S. M. Lee, S. Y. Han, C. J. Yoo, J. L. Lee, S. H. Lee, J. Kurniawan, J. Tureb, Z. Guo, J. Yoon, S. I. Park, S. Y. Bang, Y. Nam, M. C. Walicki, V. K. Samineni, A. D. Mickle, K. Lee, S. Y. Heo, J. G. McCall, T. Pan, L. Wang, X. Feng, T. I. Kim, J. K. Kim, Y. Li, Y. Huang, R. W. t. Gereau, J. S. Ha, M. R. Bruchas, and J. A. Rogers,

"Flexible Near-Field Wireless Optoelectronics as Subdermal Implants for Broad Applications in Optogenetics," *Neuron*, vol. 93, no. 3, pp. 509-521 e503, 2017.

[219] F. A. Rueggeberg, "State-of-the-art: Dental Photocuring--A Review," *Dental Materials*, vol. 27, no. 1, pp. 39-52, 2011.

[220] J.-P. Fouassier and J. Lalevée, *Photoinitiators for Polymer Synthesis: Scope, Reactivity, And Efficiency*. Singapore, Wiley, 2012.

[221] R. Schwalm, *UV Coatings: Basics, Recent Developments and New Applications*. Amsterdam, Th Netherlands, Elsevier, 2006.

[222] J. Nicholson and B. Czarnecka, *Materials for the Direct Restoration of Teeth*. Cambridge, MA, Woodhead Publishing, 2016.

[223] N. Krämer, U. Lohbauer, F. García-Godoy, and R. Frankenberger, "Light Curing of Resin-Based Composites in the LED Era," *American Journal of Dentistry*, vol. 21, no. 3, pp. 135-142, 2008.

[224] M. G. Neumann, C. C. Schmitt, G. C. Ferreira, and I. C. Correa, "The Initiating Radical Yields and the Efficiency of Polymerization for Various Dental Photoinitiators Excited by Different Light Curing Units," *Dental Materials*, vol. 22, no. 6, pp. 576-584, 2006.

[225] D. C. R. S. Oliveira, M. G. Rocha, A. Gatti, A. B. Correr, J. L. Ferracane, and M. A. C. Sinhoret, "Effect of Different Photoinitiators and Reducing Agents on Cure Efficiency and Color Stability of Resin-Based Composites Using Different LED Wavelengths," *Journal of Dentistry*, vol. 43, no. 12, pp. 1565-1572, 2015.

[226] F. A. Rueggeberg, M. Giannini, C. A. G. Arrais, and R. B. T. Price, "Light Curing in Dentistry and Clinical Implications: A Literature Review," *Brazilian Oral Research*, vol. 31, no. 1, pp. 65-91, 2017.

[227] H. J. Vreman, R. J. Wong, D. K Stevenson, R. K. Route, S. D Reader, M. M. Fejer, R. Gale, and D. S. Seidman, "Light-Emitting Diodes: A Novel Light Source for Phototherapy," *Pediatric Research* vol. 44, no. 5, pp. 804-809, 1998.

[228] J. A. Parrish and K. F. Jaenicke, "Action Spectrum for Phototherapy of Psoriasis," *Journal of Investigative Dermatology*, vol. 76, no. 5, pp. 359-362, 1981.

[229] P. Zhang and M. X. Wu, "A Clinical Review of Phototherapy for Psoriasis," *Lasers in Medical Science*, vol. 33, no. 1, pp. 173-180, 2018.

[230] L. M. Madigan, M. Al-Jamal, and I. Hamzavi, "Exploring the Gaps in the Evidence-Based Application of Narrowband UVB for the Treatment of Vitiligo," *Photodermatology, Photoimmunology & Photomedicine*, vol. 32, no. 2, pp. 66-80, 2016.

[231] H. J. Vreman, R. J. Wong, and D. K. Stevenson, "Phototherapy: Current Methods and Future Directions," *Seminars in Perinatology*, vol. 28, no. 5, pp. 326-333, 2004.

[232] M. McEwen, and K. Reynolds, "Noninvasive Detection of Bilirubin Using Pulsatile Absorption," *Autralasian Physical & Engineering Science in Medicine*, vol. 29, no. 1 pp.78-83, 2006.

[233] B. M. Martins, M. de Carvalho, M. E. Moreira, and J. M. Lopes, "Efficacy of New Microprocessed Phototherapy System with Five High Intensity Light Emitting Diodes (Super LED)," *Jornal de Pediatria*, vol. 83, no. 3, pp. 253-258, 2007.

[234] L. Lang-Bicudo, F. E. P. Eduardo, C. D. P. Eduardo, and D. M. Zezell, "LED Phototherapy to Prevent Mucositis: A Case Report," *Photomedicine and Laser Surgery*, vol. 26, no. 6, pp. 609-613, 2008.

[235] H. T. Whelan, J. F. Connelly, B. D. Hodgson, L. Barbeau, A. C. Post, G. Bullard, E. V. Buchmann, M. Kane, N. T. Whelan, A. Warwick, D. Margolis, "NASA Light-Emitting Diodes for the Prevention of Oral Mucositis in Pediatric Bone Marrow Transplant Patients," *Journal of Clinical Laser Medicine & Surgery*, vol. 20, no. 6, pp. 319-324, 2002.

[236] J. Dai, W. Gao, B. Liu, X. Cao, T. Tao, Z. Xie, H. Zhao, D. Chen, H. Ping, and R. Zhang, "Design and Fabrication of UV Band-Pass Filters Based on SiO_2/Si_3N_4 Dielectric Distributed Bragg Reflectors," *Applied Surface Science*, vol. 364, pp. 886-891, 2016.

[237] Z. Jakšić, M. Maksimović, and M. Sarajlić, "Silver–Silica Transparent Metal Structures as Bandpass Filters for the Ultraviolet Range," *Journal of Optics A: Pure and Applied Optics*, vol. 7, no. 1, pp. 51-55, 2005.

[238] M. Feneberg, R. A. R. Leute, B. Neuschl, K. Thonke, and M. Bickermann, "High-Excitation and High-Resolution Photoluminescence Spectra of Bulk AlN," *Physical Review B*, vol. 82, no. 7, pp. 075208, 2010.

[239] X. Li, S. Sundaram, P. Disseix, G. Le Gac, S. Bouchoule, G. Patriarche, F. Réveret, J. Leymarie, Y. El Gmili, and T. Moudakir, "AlGaN-Based MQWs Grown on A Thick Relaxed AlGaN Buffer on AlN Templates Emitting at 285 nm," *Optical Materials Express*, vol. 5, no. 2, pp. 380-392, 2015.

[240] D. Welch, M. Buonanno, V. Grilj, I. Shuryak, C. Crickmore, A. W. Bigelow, G. Randers-Pehrson, G. W. Johnson, and D. J. Brenner, "Far-UVC Light: A New Tool to Control the Spread of Airborne-Mediated Microbial Diseases," *Scientific Reports*, vol. 8, no. 1, pp. 1-7, 2018.

[241] J. A. Woods, A. Evans, P. D. Forbes, P. J. Coates, J. Gardner, R. M. Valentine, S. H. Ibbotson, J. Ferguson, C. Fricker, and H. Moseley, "The Effect of 222-nm UVC Phototesting on Healthy Volunteer Skin: A Pilot Study," *Photodermatology, Photoimmunology & Photomedicine*, vol. 31, no. 3, pp. 159-166, 2015.

[242] S. E. Bache, M. Maclean, G. Gettinby, J. G. Anderson, S. J. MacGregor, and I. Taggart, "Universal Decontamination of Hospital Surfaces in An Occupied Inpatient Room with A Continuous 405 nm Light Source," *Journal of Hospital Infection*, vol. 98, no. 1, pp. 67-73, 2018.

[243] I. R. M. Barnard, E. Eadie, and K. Wood, "Further Evidence That Far-UVC for Disinfection Is Unlikely to Cause Erythema or Pre-Mutagenic DNA Lesions in Skin," *Photodermatology, Photoimmunology & Photomedicine*, vol. 36, no. 6, pp. 476-477. 2020.

[244] M. Buonanno, G. Randers-Pehrson, A. W. Bigelow, S. Trivedi, F. D. Lowy, H. M. Spotnitz, S. M. Hammer, and D. J. Brenner, "207-nm UV Light - A Promising Tool for Safe Low-Cost Reduction of Surgical Site Infections. I: *In Vitro* Studies," *PLoS One*, vol. 8, no. 10, pp. e76968(1-7), 2013.

[245] Y. Taniyasu, M. Kasu, and T. Makimoto, "An Aluminium Nitride Light-Emitting Diode with A Wavelength of 210 Nanometres," *Nature*, vol. 441, no. 7091, pp. 325-328, 2006.

[246] F. Yun, M. A. Reshchikov. L. He, T. King, H. Morkoç, S. W. Novak, and L. Wei, "Energy Band Bowing Parameter in $Al_xGa_{1-x}N$ Alloys," *Journal of Applied Physics*, vol. 92, no. 8, pp. 4837-4839, 2002.

[247] S. Larouche and L. Martinu, "OpenFilters: Open-Source Software for the Design, Optimization, and Synthesis of Optical Filters," *Applied Optics*, vol. 47, pp. C219-C230, 2008.

[248] G. Hass, "Filmed Surfaces for Reflecting Optics," *Journal of the Optical Society of America*, vol. 45, no. 11, pp. 945-952, 1955.

[249] S. Saadati, "Study of Ultraviolet C Light Penetration and Damage in Skin." *Medical Physicist Programme*," Sahlgrenska Academy Department of Radiation Physics, University of Gothenburg, 2016.

[250] C. K. Sen, "Human Wounds and Its Burden: An Updated Compendium of Estimates," *Advances in Wound Care (New Rochelle)*, vol. 8, no. 2, pp. 39-48, 2019.

[251] C. K. Sen, G. M. Gordillo, S. Roy, R. Kirsner, L. Lambert, T. K. Hunt, F. Gottrup, G. C. Gurtner, and M. T. Longaker, "Human Skin Wounds: A Major and Snowballing Threat to Public Health and the Economy," *Wound Repair Regeneration*, vol. 17, no. 6, pp. 763-771, 2009.

[252] C. Sussman and B. B.-Jensen, *Wound Care: A Collaborative Practice Manual for Health Professionals*. Philadelphia, PA, Lippincott Williams & Wilkins, 2007.

[253] CORDIS. "Miniaturized Smart System for Light Stimulation and Monitoring of Wound Healing." cordis.europa.eu. https://cordis.europa.eu/project/id/644267 (accessed 29 March 2021).

[254] A. Becker, A. Klapczynski, N. Kuch, F. Arpino, K. Simon-Keller, C. De La Torre, C. Sticht, F. A. van Abeelen, G. Oversluizen, and N. Gretz, "Gene Expression Profiling Reveals Aryl Hydrocarbon Receptor as A Possible Target for Photobiomodulation When Using Blue Light," *Scientific Reports*, vol. 6, no.1, pp. 1-11, 2016.

[255] S. Guo and L. A. Dipietro, "Factors Affecting Wound Healing," *Journal of Dental Research*, vol. 89, no. 3, pp. 219-229, 2010.

[256] R. G. Frykberg and J. Banks, "Challenges in the Treatment of Chronic Wounds," Advances in Wound Care (New Rochelle), vol. 4, no. 9, pp. 560-582, 2015.

[257] Chronic wounds: Overview. InformedHealth.org, Cologne, Germany: Institute for Quality and Efficiency in Health Care (IQWiG), 2006.

[258] N. N. Houreld, "Shedding Light on A New Treatment for Diabetic Wound Healing: A Review on Phototherapy," *The Scientific World Journal*, vol. 2014, no. 398412, pp. 1-13, 2014.

[259] M.-S. Kim, Y.-I. Cho, M.-S. Kook, S.-C. Jung, Y.-H. Hwang, and B.-H. Kim, "Effect of 660 nm Light-Emitting Diode on the Wound Healing in Fibroblast-Like Cell Lines," *International Journal of Photoenergy*, vol. 2015, pp. 1-9, 2015.

[260] A. Lipovsky, Y. Nitzan, and R. Lubart, "A Possible Mechanism for Visible Light-Induced Wound Healing," *Lasers in Surgery Medicine*, vol. 40, no. 7, pp. 509-514, 2008.

[261] A. Yadav and A. Gupta, "Noninvasive Red and Near-Infrared Wavelength-Induced Photobiomodulation: Promoting Impaired Cutaneous Wound Healing," *Photodermatology, Photoimmunology & Photomedicine*, vol. 33, no. 1, pp. 4-13, 2017.

[262] H. T. Whelan, R. L. Smits, E. V. Buchman, N. T. Whelan, S. G. Turner, D. A. Margolis, V. Cevenini, H. Stinson, R. Ignatius, T. Martin, J. Cwiklinski, A. F. Philippi, W. R. Graf, B. Hodgson, L. Gould, M.Kane, G. Chen, and J. Caviness, "Effect of NASA Light-Emitting Diode Irradiation on Wound Healing," *Journal of Clinical Laser Medicine & Surgery*, vol. 19, no. 6, pp. 305-314, 2001.

[263] C. Ash, M. Dubec, K. Donne, and T. Bashford, "Effect of Wavelength and Beam Width on Penetration in Light-Tissue Interaction Using Computational Methods," *Lasers in Medical Science*, vol. 32, no. 8, pp. 1909-1918, 2017.

[264] M. R. Hamblin, "Mechanisms and Mitochondrial Redox Signaling in Photobiomodulation," *Photochemistry and Photobiology*, vol. 94, no. 2, pp. 199-212, 2018.

[265] K. Lacjakova, N. Bobrov, M. Polakova, M. Slezak, M. Vidova, T. Vasilenko, M. Novotny, F. Longauer, L. Lenhardt, J. Bober, M. Levkut, F. Sabol, and P. Gal,

"Effects of Equal Daily Doses Delivered by Different Power Densities of Low-Level Laser Therapy at 670 nm on Open Skin Wound Healing in Normal and Corticosteroid-Treated Rats: A Brief Report," *Lasers in Medical Science*, vol. 25, no. 5, pp. 761-766, 2010.

[266] B. J. Erdle, S. Brouxhon, M. Kaplan, J. Vanbuskirk, and A. P. Pentland, "Effects of Continuous-Wave (670-nm) Red Light on Wound Healing," Dermatology Surgery, vol. 34, no. 3, pp. 320-325, 2008.

[267] T. Fushimi, S. Inui, T. Nakajima, M. Ogasawara, K. Hosokawa, and S. Itami, "Green Light Emitting Diodes Accelerate Wound Healing: Characterization of the Effect and Its Molecular Basis In Vitro and In Vivo," *Wound Repair and Regeneration*, vol. 20, no. 2, pp. 226-235, 2012.

[268] M.-W. Cheon and Y.-P. Park, "Wound Healing Effect of 525 nm Green LED Irradiation on Skin Wounds of Male Sprague Dawley Rats," *Transactions on Electrical and Electronic Materials*, vol. 11, no. 5, pp. 226-229, 2010.

[269] P. Chotikasemsri, "G Protein-coupled Receptors and Proopiomelanocortin Expression After Light Emitting Diode Irradiation in Diabetic Wound Healing" *Wounds: A Compendium of Clinical Research and Practice*, vol. 29, no. 11, pp. 311-316, 2017.

[270] W. K. Ong, H. F. Chen, C. T. Tsai, Y. J. Fu, Y. S. Wong, D. J. Yen, T. H. Chang, H. D. Huang, O. K. Lee, S. Chien, and J. H. Ho, "The Activation of Directional Stem Cell Motility by Green Light-Emitting Diode Irradiation," *Biomaterials*, vol. 34, no. 8, pp. 1911-1920, 2013.

[271] R. K. Hobbie and B. J. Roth, *Intermediate Physics for Medicine and Biology*. Springer, 2015.

[272] T. Dai, A. Gupta, C. K. Murray, M. S. Vrahas, G. P. Tegos, and M. R. Hamblin, "Blue Light for Infectious Diseases: Propionibacterium Acnes, Helicobacter Pylori, and Beyond?," *Drug Resistance Updates*, vol. 15, no. 4, pp. 223-236, 2012.

[273] T. Dai, "The Antimicrobial Effect of Blue Light: What Are Behind?," *Virulence*, vol. 8, no. 6, pp. 649-652, 2017.

[274] W. D. Enwemeka CS, Enwemeka SK, Hollosi S, Yens D., "Blue 470-nm Light Kills Methicillin-Resistant Staphylococcus Aureus (MRSA) in Vitro " *Photomedicine and Laser Surgery*, vol. 27, no. 2, p. 221-226, 2009.

[275] N. T. de Sousa, M. F. Santos, R. C. Gomes, H. E. Brandino, R. Martinez, and R. R. de Jesus Guirro, "Blue Laser Inhibits Bacterial Growth of Staphylococcus Aureus, Escherichia Coli, and Pseudomonas Aeruginosa," *Photomedicine and Laser Surgery*, vol. 33, no. 5, pp. 278-282, 2015.

[276] P. Yang, N. Wang, C. Wang, Y. Yao, X. Fu, W. Yu, R. Cai, and M. Yao, "460nm Visible Light Irradiation Eradicates MRSA via Inducing Prophage Activation," *Journal of Photochemistry and Photobiology B*, vol. 166, pp. 311-322, 2017.

[277] N. Adamskaya, P. Dungel, R. Mittermayr, J. Hartinger, G. Feichtinger, K. Wassermann, H. Redl, and M. van Griensven, "Light Therapy by Blue LED Improves Wound Healing in An Excision Model in Rats," *Injury*, vol. 42, no. 9, pp. 917-921, 2011.

[278] M. W. Cheon, T. G. Kim, Y. S. Lee, and S. H. Kim, "Low level light therapy by Red–Green–Blue LEDs Improves Healing in An Excision Model of Sprague–Dawley Rats," *Personal and Ubiquitous Computing*, vol. 17, no. 7, pp. 1421-1428, 2012.

[279] F. Rossi, G. Magni, F. Tatini, M. Banchelli, F. Cherchi, M. Rossi, E. Coppi, A. M. Pugliese, D. Rossi degl'Innocenti, D. Alfieri, F. S. Pavone, R. Pini, and P. Matteini, "Photobiomodulation of Human Fibroblasts and Keratinocytes with Blue Light: Implications in Wound Healing," *Biomedicines*, vol. 9, no. 1, pp. 41(1-14), 2021.

[280] F. Jaffary, V. Changizi, H. Mardani, P. Kakanezhadian, F. M. Javadi, M. A. Nilforoushzadeh, and E. Haftbaradaran, "Macroscopic Effect of Blue Light Cure on Wound Healing in NMRI Mice NMRI," *Advanced Biomedical Research*, vol. 3, no. 106, pp. 1-6, 2014.

[281] R. Cicchi, F. Rossi, D. Alfieri, S. Bacci, F. Tatini, G. De Siena, G. Paroli, R. Pini, and F. S. Pavone, "Observation of An Improved Healing Process in Superficial Skin Wounds after Irradiation with a Blue-LED Haemostatic Device," *Journal of Biophotonics*, vol. 9, no. 6, pp. 645-655, 2016.

[282] L. R. Koller, "Bactericidal Effects of Ultraviolet Radiation Produced by Low Pressure Mercury Vapor Lamps," *Journal of Applied Physics*, vol. 10, no. 9, pp. 624-630, 1939.

[283] N. Vermeulen, W. J. Keeler, K. Nandakumar, and K. T. Leung, "The Bactericidal Effect of Ultraviolet and Visible Light on Escherichia Coli," *Biotechnology and Bioengineering*, vol. 99, no. 3, pp. 550-556, 2008.

[284] K. I. Møller, B. Kongshoj, P. A. Philipsen, V. O.Thomsen, H. C. Wulf, "How Finsen's Light Cured Lupus Vulgaris," *Photodermatology, Photoimmunology & Photomedicine*, vol. 21, no. 3, pp. 118–124, 2005.

[285] E. R. Blatchley, N. Dumoutier, T. N. Halaby, Y. Levi, J. M. Laîne, "Bacterial Responses to Ultraviolet Irradiation," *Water Science and Technology*, vol. 43, no. 10, pp. 179-186, 2001.

[286] H. C. Rentschler, R. Nagy, and G. Mouromseff, "Bactericidal Effect of Ultraviolet Radiation," *Journal of Bacteriology*, vol. 41, no. 6, pp. 745–774, 1940.

[287] T. P. Thai, P. E. Houghton, D. H. Keast, K. E. Campbell, and M. G. Woodbury, "Ultraviolet Light C in the Treatment of Chronic Wounds with MRSA A Case Study," *Ostomy Wound Manage*, vol. 48, no. 11, pp. 52-60, 2002.

[288] T. A. C. -Kerr, P. K. Sullivan, J. Gaillard, M. E. Franklin, R. M. Jones, "The Effects of Ultraviolet Radiation on Antibiotic-Resistant Bacteria in Vitro," *Ostomy Wound Manage*, vol. 44, no. 10, pp. 50-56, 1998.

[289] J. Li, K. Hirota, H. Yumoto, T. Matsuo, Y. Miyake, T. Ichikawa "Enhanced Germicidal Effects of Pulsed UV-LED Irradiation on Biofilms," *Journal of Applied Microbiology*, vol. 109, no. 6, pp. 2183-2190, 2010.

[290] T. Dai, M. S. Vrahas, C. K. Murray, and M. R. Hamblin, "Ultraviolet C Irradiation: An Alternative Antimicrobial Approach to Localized Infections?," *Expert Review of Anti-infective Therapy*, vol. 10, no. 2, pp. 185-195, 2012.

[291] S. F. Davidson, S. K. Brantly, and S. K. Das. "The Effects of Ultraviolet Radiation on Wound Healing," *British Journal of Plastic Surgery*, vol. 44, pp. 210-214, 1991.

[292] K. Yano, K. Kajiya, M. Ishiwata, Y. K. Hong, T. Miyakawa, and M. Detmar, "Ultraviolet B-Induced Skin Angiogenesis is Associated with A Switch in the Balance of Vascular Endothelial Growth Factor and Thrombospondin-1 Expression," *Journal of Investigative Dermatology*, vol. 122, no. 1, pp. 201-208, 2004.

[293] M. Brauchle, J. O. Funk, P. Kind, S. Werner, "Ultraviolet B and H_2O_2 Are Potent Inducers of Vascular Endothelial Growth Factor Expression in Cultured Keratinocytes," *The Journal of Biological Chemistry*, vol. 271, no. 36, pp. 21793-21797, 1996.

[294] M. Meinhardt, R. Krebs, A. Anders, U. Heinrich, and H. Tronnier, "Wavelength-Dependent Penetration Depths of Ultraviolet Radiation in Human Skin," *Journal of Biomedical Optics*, vol. 13, no. 4, pp. 044030-5, 2008.

[295] M. Brenner, K. Degitz, R. Besch, and C. Berking, "Differential Expression of Melanoma-Associated Growth Factors in Keratinocytes and Fibroblasts by Ultraviolet A and Ultraviolet B Radiation," *British Journal of Dermatology*, vol. 153, no. 4, pp. 733-739, 2005.

[296] I. Willis and L. Cylus, "UVA Erythema in Skin: Is It a Sunburn?," *Journal of Investigative Dermatology*, vol. 68, no. 3, pp. 128-129, 1977.

[297] J. L. Zhong, L. Yang, F. Lu, H. Xiao, R. Xu, L. Wang, F. Zhu, and Y. Zhang, "UVA, UVB and UVC Induce Differential Response Signaling Pathways Converged on the eIF2α Phosphorylation," *Photochemistry and Photobiology*, vol. 87, no. 5, pp. 1092-1104, 2011.

[298] H. Siiskonen, A. Smorodchenko, K. Krause, and M. Maurer, "Ultraviolet Radiation and Skin Mast Cells: Effects, Mechanisms and Relevance for Skin Diseases," *Experimental Dermatology*, vol. 27, no. 1, pp. 3-8, 2018.

[299] M. F. Holick, "Ultraviolet B Radiation: The Vitamin D Connection," in *Ultraviolet Light in Human Health, Diseases and Environment*, S. I. Ahmad, Ed., vol. 996, Cham, Switzerland, Springer, 2017, pp. 137-154.

[300] Y. Yuan, S. K. Das, and M. Li, "Vitamin D Ameliorates Impaired Wound Healing in Streptozotocin-Induced Diabetic Mice by Suppressing NF-κB-Mediated Inflammatory Genes," *Bioscience Reports*, vol. 38, no. 2, pp. 1-10, 2018.

[301] M. M. Lankford KV, Hillyer CD, "Effects of UVB Radiation on Cytokine Generation, Cell Adhesion Molecules, and Cell Activation Markers in T-Lymphocytes and Peripheral Blood HPCs," *Transfusion*, vol. 40, no. 3, pp. 361-367, 2000.

[302] J. W. Zhu, X. J. Wu, D. Luo, Z. F. Lu, S. Q. Cai, and M. Zheng, "Activation of VEGFR-2 Signaling in Response to Moderate Dose of Ultraviolet B Promotes Survival of Normal Human Keratinocytes," *The International Journal of Biochemistry & Cell Biology*, vol. 44, no. 1, pp. 246-256, 2012.

[303] P. Bao, A. Kodra, M. Tomic-Canic, M. S. Golinko, H. P. Ehrlich, and H. Brem, "The Role of Vascular Endothelial Growth Factor in Wound Healing," *Journal of Surgical Research*, vol. 153, no. 2, pp. 347-358, 2009.

[304] K. Yano, K. Kadoya, K. Kajiya, Y. K. Hong, and M. Detmar, "Ultraviolet B Irradiation of Human Skin Induces an Angiogenic Switch That Is Mediated by Upregulation of Vascular Endothelial Growth Factor and by Downregulation of Thrombospondin-1," *British Journal of Dermatology*, vol. 152, no. 1, pp. 115-121, 2005.

[305] M. R. Kaiser, S. C. Davis, B. M. Mertz, "The Effect of Ultraviolet Irradiation Induced Inflammation on Epidermal Wound Healing," *Wound Repair Regeneration*, vol. 3, no. 3, pp. 311-315, 1995.

[306] G. M. Fluhr and M. Gloor "The Antimicrobial Effect of Narrow-Band UVB (313 nm) and UVA1 (345-440 nm) Radiation in Vitro," *Photodermatology, Photoimmunology & Photomedicine*, vol. 13, no. 5-6, pp. 197-201, 1997.

[307] S. P. Hong, M. J. Kim, M. Y. Jung, H. Jeon, J. Goo, S. K. Ahn, S. H. Lee, P. M. Elias, and E. H. Choi, "Biopositive Effects of Low-Dose UVB on Epidermis: Coordinate Upregulation of Antimicrobial Peptides and Permeability Barrier Reinforcement," *Journal of Investigative Dermatology*, vol. 128, no. 12, pp. 2880-2887, 2008.

[308] P. E. Hockberger, "A History of Ultraviolet Photobiology for Humans, Animals and Microorganisms," *Photochemistry and Photobiology*, vol. 76, no. 6, pp. 561-579, 2002.

[309] R. Yin, T. Dai, P. Avci, A. E. Jorge, W. C. de Melo, D. Vecchio, Y. Y. Huang, A. Gupta, and M. R. Hamblin, "Light Based Anti-Infectives: Ultraviolet C Irradiation, Photodynamic Therapy, Blue Light, and Beyond," *Current Opinion in Pharmacology*, vol. 13, no. 5, pp. 731-762, 2013.

[310] P. K. Rao, B. Kumar, S. Rao, and B. Gurung, "Bactericidal Effect of Ultraviolet C (UVC), Direct and Filtered Through Transparent Plastic, on Gram-Positive Cocci: an in Vitro Study," *Ostomy Wound Manage*, vol. 57, no. 7, pp. 46-52, 2011.

[311] J. Dobrowolski, "The Impact of Computers on The Design and Manufacture of Optical Multilayer Coatings During the Past 50 years," *In the Annual Technical Conference-Society of Vacuum Coaters*, 2007, pp. 33-44, 2007.

[312] H. P. T. Nguyen and Y. Evo "Phosphor-Free III-Nitride Nanowire White Light Emitting Diodes Challenges and Prospects," *ECS Transactions*, vol. 66, no. 4, pp. 213-221, 2015.